Zeitschrift: Helvetica Physica Acta
Band: 63 (1990)
Heft: 4

Vereinsnachrichten: Herbsttagung der SPG/SSP
Autor: [s.n.]

Helvetica Physica Acta
Vol. 63 (1990)

0018-0238/90/040471-86$1.50+0.20/0

The incommensurate γ phase of n-propylammonium tetrachlorometallates

Bernard Doudin† and Volker Heine§

† Institut de Cristallographie, Université de Lausanne, 1015 Dorigny, CH

§ Cavendish Laboratory, Madingley Road, Cambridge CB3 OHE, UK

Abstract: This paper presents a study of the γ phase observed for the $(C_3H_7NH_3)_2CuCl_4$ and $(C_3H_7NH_3)_2MnCl_4$ compounds. With the help of their structural knowledge, a physical mechanism involving only the organic part of the structure has been found for the transition. Computer calculations exhibit the instability favourizing a modulated configuration and give a quantitative support to the model.

1. The observations [1, 2]

These two compounds present a structure characterized by a succession of inorganic layers with corner-sharing $Cu(Mn)Cl_6$ octahedra. The ammonium ends of the organic chains are connected by hydrogen bonds to the Cl atoms. The methyl ends protruding from two successive inorganic layers are stacked to form 'the slice inside the sandwich'. For both compounds, the modulated γ phase is limited in the temperature range by the β (T>~450K) and the δ (T<~350K) phases exhibiting the same group of symmetry.

2. The model [3]

Figure 1 resumes the main characteristics of the γ phase. The two configurations 'P' and 'T' correspond to the periodic arrangement of phases β and δ.

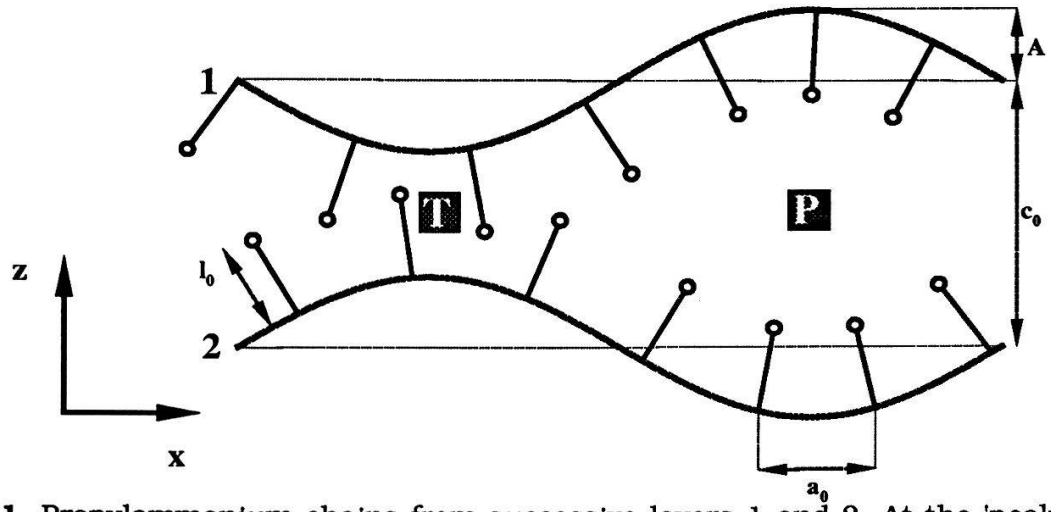

Figure 1. Propylammonium chains from successive layers 1 and 2. At the 'peaks' P of the modulation, the chains from successive layers draw apart, but adjacent chains from the same layer come close together. At the 'trough' T the adjacent chains in the same layer are splayed open and allow greater interpenetration by the chains from the next layer. The lines at 1 and 2 denote the metal chloride backbone of the layers.

The distance a_0 separating two adjacent chains has a value constrained by the periodicity of the inorganic backbone, critical in the γ phase.

3. The calculations

We used an hypothetical crystal formed by an arrangement of propane chains, with a symmetry reproducing the observations. The local energy, involving only interactions between non bonded organic atoms, can be estimated with fixed values of the translations along **x** and **z**. The interatomic potential is a summ of a repulsive of type $\exp(r^{-1})$ form, an attractive Van der Waals energy (r^{-6}) and a Coulombic interaction. The parameters concerning the organic atoms have been fitted with a large number of observed structures [4]. For a value of a_0 lower than 7.0Å, this function has a saddle point confirming the instability. This static model reproduces the δ phase (configuration 'T') if the value of a_0 is larger, corresponding to the observations (a_{obs} ~ 7.4Å).

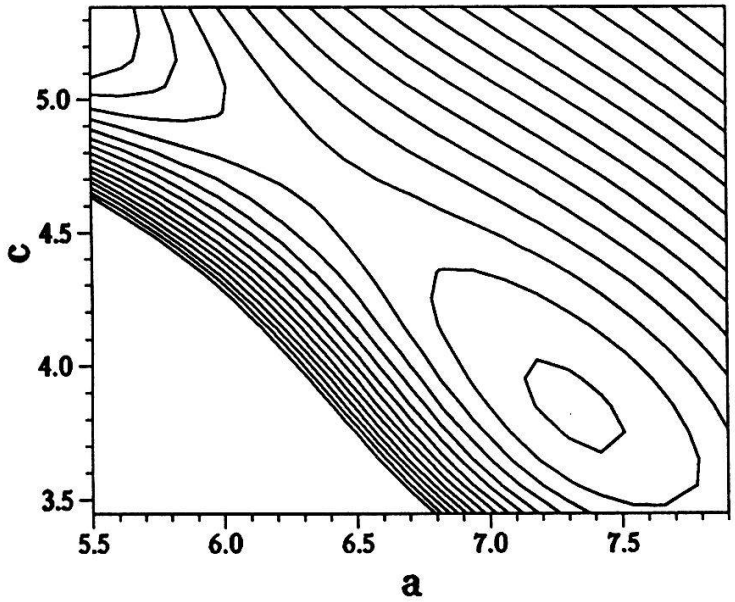

Figure 2. Energy contours of the simulation, showing the local energy E(a,c). In producing this plot, we have removed the effect of the first derivative $(\partial E/\partial a)_{a_0=6.4Å}$ which is balanced by the rigidity of the backbone.

The financial assistance of the Science and Engineering Research Council of the UK and the Fondation Georgine Claraz to B. D. are gratefully acknowledged.

4. References

[1] W. Depmeier, Acta Cryst. B**44**, 330 (1981).
[2] B. Doudin & G. Chapuis, Acta Cryst B, in press (1989).
[3] P. Muralt, J. Phys. C**19**, 1689 (1986).
[4] D. E. Williams & E. R. Cox, J. Chem. Phys. **56**, 1897 (1972).

THE VOLUME OF DENDRITES

E. Hürlimann, R. Trittibach, and J.H. Bilgram
Laboratorium für Festkörperphysik, ETH, 8093 Zürich

Abstract: The volume V of xenon dendrites growing into supercooled melt has been measured as a function of an overall length L of the dendrites at various supercoolings ΔT. We find $V \propto L^3$ at a given supercooling, and $V \propto \Delta T^{4.5}$ at a given time. These results are in agreement with a simple model, which is based on the assumption of a steady state and continuity.

1. A Simple Model

We consider a stationary state. The overall length of the dendrite at a given time is L. All latent heat has to pass through a sphere with the diameter 2L. The volume solidification rate is: $\frac{dV}{dt} \propto \int_S \nabla_L \, d\sigma$ (S = the surface of the sphere) (1)

The thermal gradient at the surface of the sphere ∇_L depends on orientation. We define an averaged and normalized gradient ∇_L^*:

$$L^2 \Delta T \, \nabla_L^* = \int \nabla_L d\sigma \qquad (2)$$

For low Péclet numbers p we can use $\Delta T \propto p \propto v_{tip} R$ [1]. We obtain for a given ΔT: $\frac{dV}{dt} \propto \nabla_L^* R v_{tip} L^2$ and $V \propto RL^3$ (3)

R and v_{tip} are the dendrite tip radius and the tip growth velocity. Using $R \propto \Delta T^{-0.68}$ and $v_{tip} \propto \Delta T^{1.73}$ [1], we obtain for a given time: $V \propto \Delta T^{4.5}$. (4)

2. Experimental Results

The growth vessel shown in Fig.1 is immersed in a bath. The setup is similar to the one described in [1]. Two optics are used

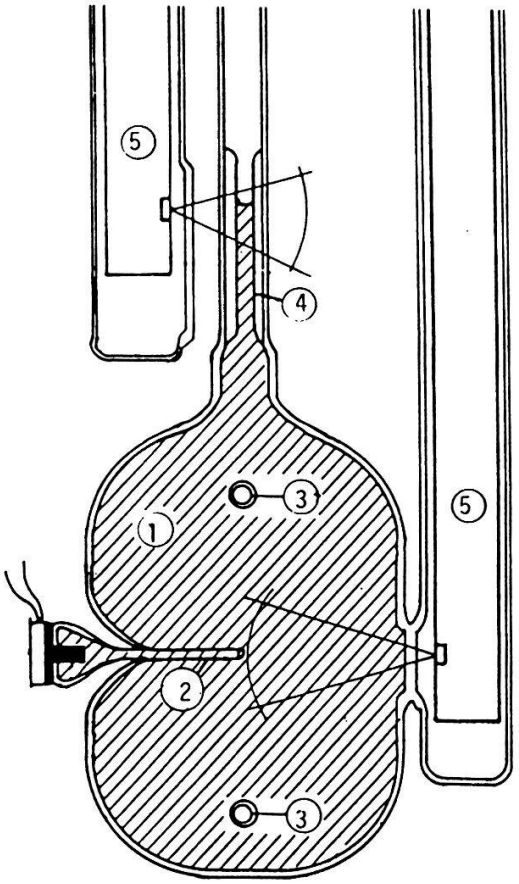

Fig.1 Growth vessel 1) liquid rare gas, 2) injection capillary 3) temperature sensor, 4) calibrated capillary, 5) optics

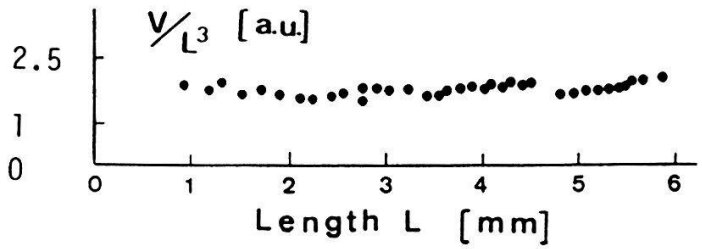

Fig.2 Average density in arb. units vs. L

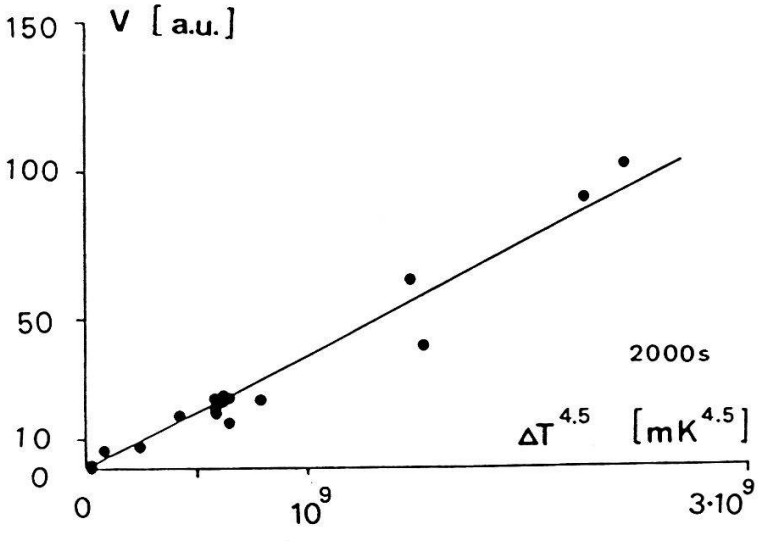

Fig.3 The volume of dendrites in arb. units vs. the supercooling $\Delta T^{4.5}$

to measure the volume change in the calibrated capillary and the length of the dendrite. The change in density upon freezing is 14% for xenon. Fig.2 shows the solidified volume of a cluster of dendrites growing out of the capillary. Fig.3 shows the volume of dendrites after growth for 2000 s into a bath with the initial supercooling ΔT. The experiment confirms eq.3 and eq.4.

Acknowledgements: We thank Prof. H.R. Ott for his support. This work is supported by the Swiss National Science Foundation.

3. References

[1] J.H. Bilgram, M. Firmann, and E. Hürlimann, J. Crystal Growth, 96, 175 (1989)

A HOPF BIFURCATION IN A SELF-ORGANIZING HELIUM II SURFACE SYSTEM

P.W. Egolf and D.A. Weiss, Laboratorium für Festkörperphysik, ETH-Hönggerberg, CH-8093 Zürich

Abstract: In our fluiddynamical system a spontaneous creation of an oscillation mode has been observed.

1. A reorganization process in real space

When standing second sound waves are generated in superfluid ^{4}He, they are coupled to pressure waves with much smaller energy density fluxes. These in their turn create surface waves on the liquid gas interface.

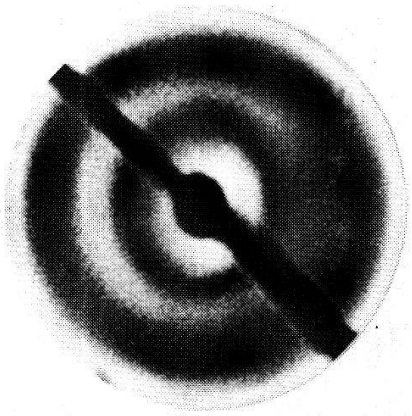

Fig. 1

The strength of the external forcing of the system can be described by a dimensionless stress number. For our system such a number is introduced in [1] as (Zk). Below a critical value $(Zk)_c$ the surface structures are stationary. An axially symmetric example of the resulting "waves" is shown in Fig. 1.

At the critical value the "waves" become unstable and a spatial reorganization process to a new stable state sets in. This is described in [2]. Above the critical value the axial symmetry is broken and the spatial patterns are to some extent disordered (see Fig. 2).

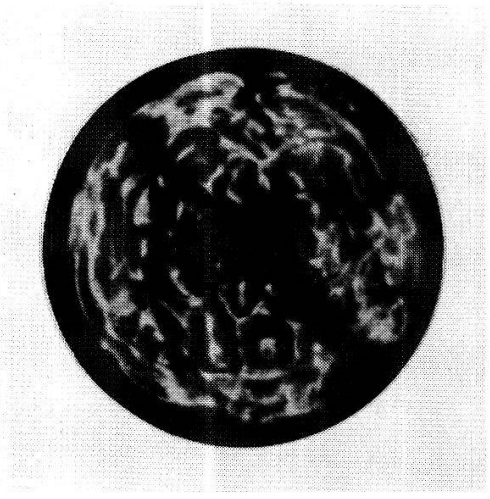

Fig. 2

2. Self-organization in time

Photodiodes with very small windows (ϕ = 0.2 mm) have been added to our schlieren technical equipment [1]. Each of them yields a current that is related in a well defined way to the pattern inclination at a certain point of the surface. We have connected a first diode to the x- and a second one to the y-input of an oscillograph.

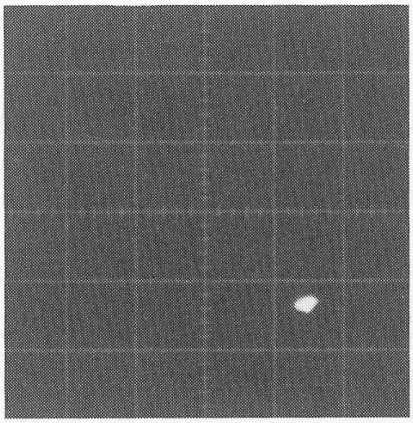

Below criticality, a fixed point in the x-y diagram (Fig. 3a) confirms the theoretically predicted stationarity of the surface structures at low intensities [1]. At the critical value $(Zk)_c$ the system becomes unstable (Fig. 3 b); the kind of instability occurring is called Hopf bifurcation and causes the reorganization of the patterns described in § 1 to begin. With increasing stress number some higher frequencies appear (Fig. 3c) and a continuous self-generated noise spectrum begins to grow. Therewith our surface motion becomes increasingly disordered in space and time behaviour.

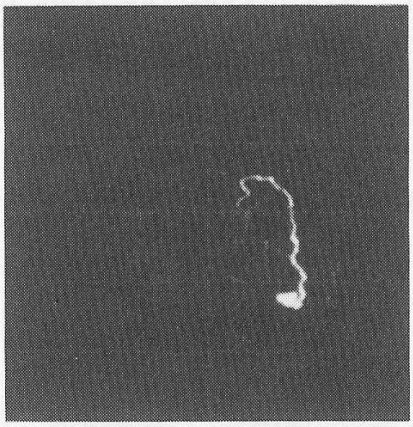

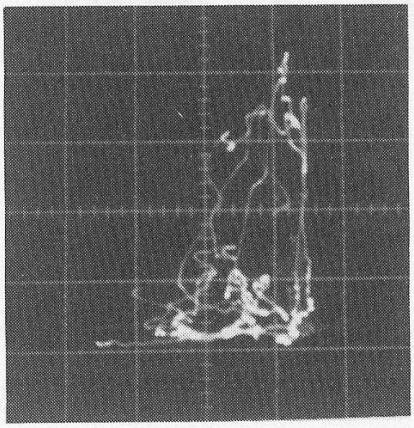

Fig. 3 a,b, and c

We would like to thank P. Caminada for his contribution to this work.

3. References

[1] J.L. Olsen., J. Low Temp. Phys. 61, 17 (1985)

[2] P.W. Egolf, J.L. Olsen, and B. Röhricht, Helv. Phys. Acta 62 (1989)

Light scattering experiments at the solid-liquid interface of a molten sphere

R.Steininger und J.H.Bilgram
Laboratorium für Festkörperphysik,ETH,8093-Zürich

Abstract: The dynamics of crystal growth are studied by quasi-elastic light scattering. A new crystal growth geometry has been developed which eliminates any possibility of a contamination of the melt. A small liquid sphere is molten inside a crystal. Light scattering at the solid-liquid interface is observed during inward growth of the crystal. The dynamics in the interface layer is ca. 10^6 times slower than in the bulk liquid. These experiments corroborate earlier results that continuous fluctuations occur at the solid-liquid interface.

1. Experimental

A small temperature sensor (TS) is frozen in a bulk cyclohexane crystal. The crystal with the TS is multiple zone refined. A small liquid sphere ($\varnothing \simeq 4$ mm) is molten inside the crystal by heating at the TS [fig. 1]. Melting or growth are controlled by the heat produced at the TS. The melt in this experiment is only in contact with its own crystal. Light scattering experiments are performed at the solid-liquid interface [1].

2. Results

During the inward growth of the crystal we observe the same light scattering phenomena as in earlier experiments [1]. The scattering develops at the s.-l. interface during growth of the crystal [fig. 1]. The dynamics can be described by a diffusion constant D_i. $D_i \simeq 3 \cdot 10^{-9}$ cm^2/s. The scattering is localized at the s.-l. interface only. No scattering remains in the newly formed crystal. Once the scattering is initiated, it does not disappear if growth is stopped. It sticks to the interface even

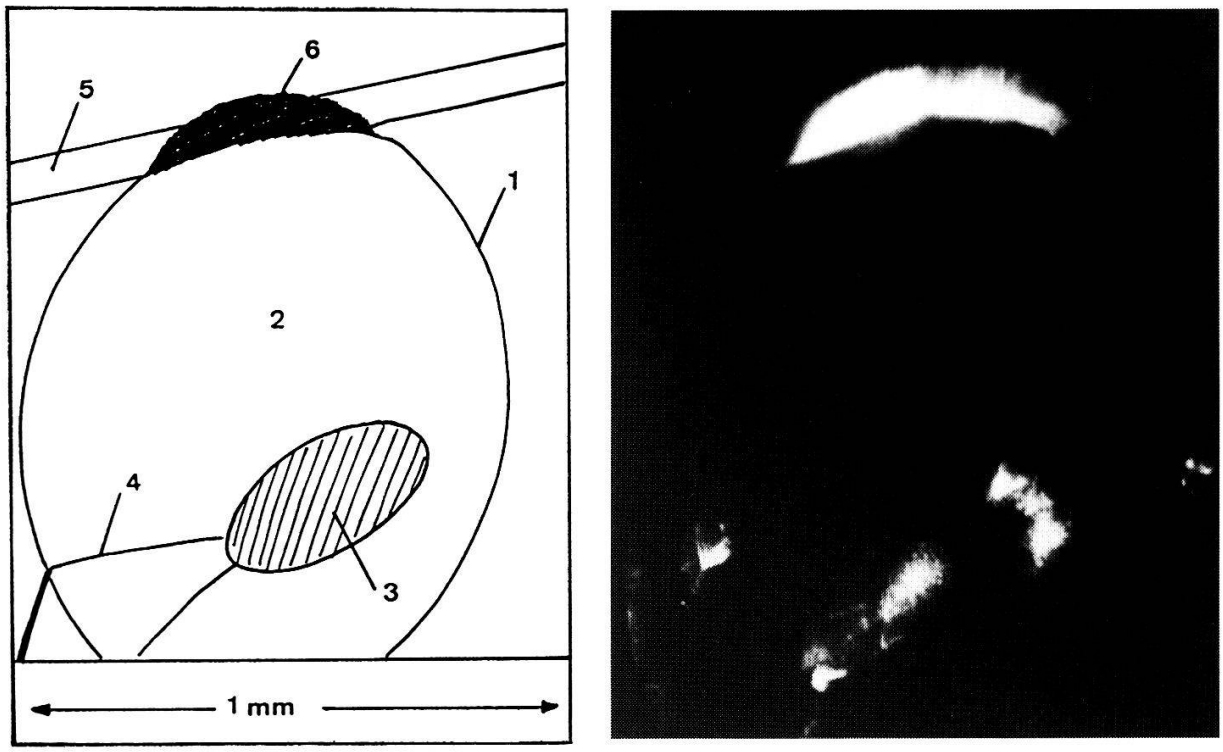

Fig.1: Light scattering at the s.-l. interface of an inward growing crystal. Sketch of the experimental setup. 1) surface of the growing crystal, 2) molten sphere, 3) TS, 4) leads to the TS, 5) laser beam, 6) scattering region.

if the crystal is melted. It is concluded that the light is not scattered by surface corrugations or by segregated impurities. The light is scattered by continuous fluctuations with a long range correlation length and slow dynamics in an interface layer. These conclusions confirm the results of light scattering experiments during zone refining of cyclohexane [2].

Acknowledgments: We thank Prof. H.R. Ott for his support. This work was supported by the Swiss National Science Foundation

3. References

[1] J.H.Bilgram,Phys.Reports,153(1987)1

[2] R.Steininger and J.H.Bilgram,Helv.Phys.Acta 62(1989)215
R.Steininger and J.H.Bilgram,Proc.ICCG9,J.Cryst.Growth,to be publ.(1990)

INELASTIC LIGHT SCATTERING (BRILLOUIN) FROM RAYLEIGH MODES ON DIFFERENT SURFACES OF Ni SINGLE CRYSTALS

M.Mendik and P.Wachter
Laboratorium für Festkörperphysik, ETHZ, CH – 8093 Zürich

Abstract

Brillouin–spectroscopy of surface acoustic waves on semiinfinite media is a versatile tool for characterising the symmetry of surfaces and the elastic properties of solids. Some of our results from acoustic modes on (100), (110) and (111) surfaces of a Ni single crystal are presented. The obtained data are used to determine the complete elastic tensor of the bulk.

Introduction

The presence of a surface causes interference of LA and TA bulk waves and is therefore the origin of surface waves. The solutions of the wave equation for the displacement in an elastic and homogeneous medium are forced to obey boundary conditions ($\sigma_{3j}(j=1,2,3) = 0$ at the surface). Therefore the components normal to the surface have either purely imaginary damping constants (Rayleigh surface wave,RSW) or also a real part in the anisotropic case (generalized Rayleigh wave). These thermally excited surface ripples, moving like a grating on the surface, are the reason for light scattering in opaque media. The elastooptic mechanism does not have any contribution to the scattering cross section because of opacity broadening. It was demonstrated by Elmiger [1] that it is possible to obtain the complete elastic tensor of the bulk of single crystals using the measured angular dispersion of surface waves. In this paper we report our results of an investigation of RSW phase velocities on different planes of a Ni single crystal and the result of a numerical calculation of the elastic constants C_{11}, C_{12} and C_{44}.

Experimental

A 3+3 Tandem interferometer was used to analyse the backscattered light[2]. The measurements were carried out in air and at room temperature. We used the λ=514 nm line (TM polarised, 80mW) of a single mode single frequency Ar+ Laser. The incident beam made an angle of 71 degree to the normal. By varying the scattering geometry it is possible to select single surface waves propagating along any direction. (100), (110) and (111) faces were cut from a single Ni crystal and mechanically polished ($1/4\mu$).

Measurements

The measured velocities are 2–5% lower than those calculated[3] with data from ultrasonic measurements. Because the high anisotropy coefficient η=2.38 there are well measurable deviations of the phase velocity.

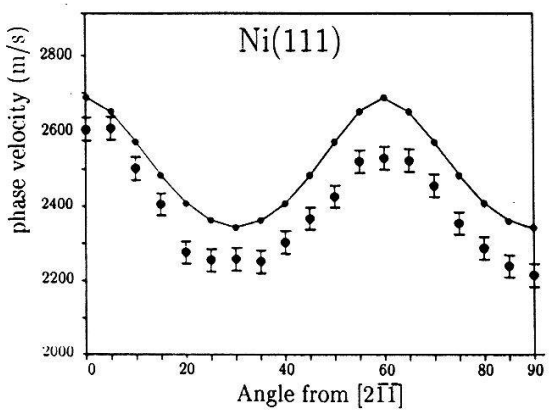

Fig.1 shows the experimentally observed surface wave velocity on (111) plane as a function of direction. (● calculated velocities) The azimuth angle is measured between Q(propagation direction of the surface wave) and [2$\bar{1}\bar{1}$]. There is a six fold symmetry observable instead of the threefold cubic axis.

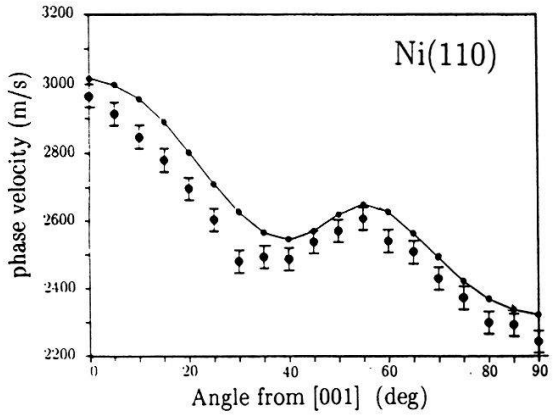

Fig.2 Angular dispersion on a (110) plane: The surface wave is a RSW at 0° and at 90° (particle displacement ellipse lies in the sagittalplane, principal axis is perpendicular to the surface). For intervening angles it becomes a gRSW (the plane of particle motion is inclined)

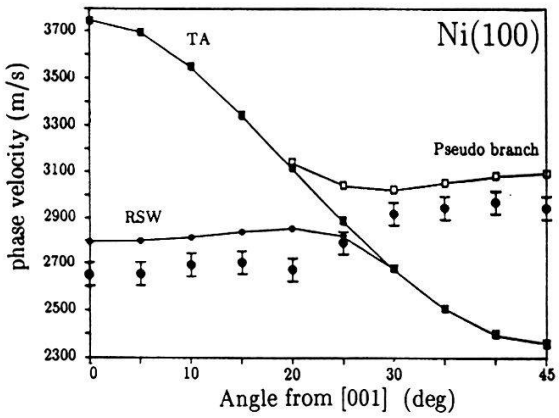

Fig.3 Angular dispersion on a (100) plane: The plane of the displacement ellipse of the RSW coincides at 0° with the sagittal plane but turns out of it with increasing α and the wave degenerates at about 30° into the TA bulk mode. Therefore this mode has progressively weaker coupling with the light. From 30° to 45° the imaginary part of Q is decreasing and therefore the Pseudo surface wave causes corrugations on the plane. That velocity can be measured by BS though with smaller intensity.

Calculations

In order to get the elastic tensor we applied the Levenberg–Marquardt procedure to perform a least square fit of the measured phase velocities to the model function in [3]. We used the surface wave velocities of the (100) plane and obtained the following results (in brackets the deviations from ultrasonic measurements [4]):C_{11}=240.6 GPa (2%), C_{44} = 98.8 GPa (20%), C_{12}=151.1 GPa (3%) with ρ=8.91 g cm–1. It is a general finding that the velocities measured by BS are lower than those calculated from ultrasonic data. The reason of this variation is still not clear. One explanation involves the difference between the isothermal and adiabatic stiffness[5] and an other the interaction of charge carriers produced by the incident light[6]. The surface preparation could have an additional influence to the decrease of C_{44}.

Acknowledgements

We wish to gratefully thank M.Elmiger for helpful discussions and S.Sathish, E.Fischer and F.Meier for Ni single crystals.

References

[1] M.W. Elmiger, Surface and Interface Analysis,14,18(1989)
[2] J.R. Sandercock in: "Light Scattering in Solids II",173,Springer (1982)
[3] G.W. Farnell in:"Physical Acoustics",VI,109;Ed.:W.P.Mason,Academic press(70)
[4] American Institute of Physics Handbook,Third edition,2.51–2.52
[5] O.L.Anderson,J.Phys.Chem.Solids 27,547 (66)
[6] A.K.Sood,M.Cardona,Solid State Communications 60,629(1986)

Temperature Stability of Interfacial Ordering in Strained Layer Si-Ge Superlattices

E. Müller, H.-U. Nissen, M. Ospelt, H. von Känel
Laboratorium für Festkörperphysik, ETH Zürich, Switzerland

The interface structure of strained layer Si-Ge superlattices on Si(100) is investigated by SAD techniques and HRTEM. Diffraction evidence is presented for the existence of domains, chemically ordered along the <111> directions. Experiments with annealed specimens indicate that ordering persists up to 575°C . This temperature is slightly above the temperature of transformation into an alloy structure.

During the last four years, strained layer superlattices (SLS) of pure Ge and Si on Si(100) have been of great interest because of changes in the band structure due to strain and to zone folding effects[1,2]. From theoretical investigations, new optical transitions can be expected to occur in perfectly grown superlattices. For these calculations, layered systems with ideally sharp interfaces are assumed. We attempted to characterize the deviations of the real crystal interfaces, grown by MBE, from a sharp boundary. By applying the techniques of high resolution transmission electron microscopy (HRTEM), Fig. 1 and selected area electron diffraction (SAD), Fig. 2, we found evidence of an ordering in the boundary layers of the SLS. In addition to the spots originating from the diamond structure and to those due to the superlattice, there are intensities in the SAD patterns at positions (h,k,l) = (1/2,1/2,1/2), (h,k,l) = (3/2,1/2,1/2), etc. and a streaking along the growth direction connecting the additional intensities[3]. These spots at half integer positions indicate a doubling of the unit cell along the four equivalent <111> axes. We explain this doubling by a bilayer stacking of Si and Ge atoms along the (111) axis (Fig. 3)[4]. This ordering by interdiffusion along the interfaces probably locally reduces the strain. For a layer thickness of more than 5 atomic layers this results in merely two-dimensional ordering and leads to a threadlike diffraction intensity distribution. For layers thinner than 4-5 monolayers, the ordering can exist throughout the whole thickness of a layer and therefore become three-dimensional. Thus spots are expected as additional diffraction intensities. This is in perfect agreement with experimental results.

Since the assumed ordering changes the materials properties, we have investigated whether it is removed by annealing. Samples were annealed at various temperatures up to 700°C for half an hour and subsequently cooled with a rate of 50°C/Min. Figs. 2 and 4a-c (all SAD patterns in [130] projection) present a series of annealed samples of a strain-symmetrized superlattice showing that the ordering is still present at 575°C, while at 600°C it has vanished. At this temperature, the superlattice structure is altered towards that of an alloy. Fig. 5 shows an asymmetrically strained superlattice on a Ge-buffer. Ordering is again present up to 575°C, however the quality of the superlattice is already lowered at this temperature,

probably resulting from the particular strain distribution. Reversability of ordering was investigated by annealing a sample at 700°C and cooling at a rate of only 1-2°C/Min. While the HRTEM images show that the superlattice has been converted into an alloy, the SAD patterns again show the additional spots indicating that ordering has reoccurred. In conclusion, ordering must be assumed to occur along the interfaces of as grown Si-Ge SLS. It is independent of the growth temperature and cannot be destroyed by annealing without the destruction of the superlattice at the same time.

1 S. Froyen, D.M. Wood, A. Zunger, Phys. Rev. **B36**, 4547 (1987)

2 M.S. Hybertsen, M. Schlüter, Phys. Rev. **B36**, 9683 (1987)

3 E. Müller et al., to be published in Proc. Third Int. Symp. on Si - MBE, Eur. Mat. Res. Soc., Strasbourg, 1989.

4 A. Ourmazd and J.C. Bean, Phys. Rev. Lett. **55**, 765 (1985)

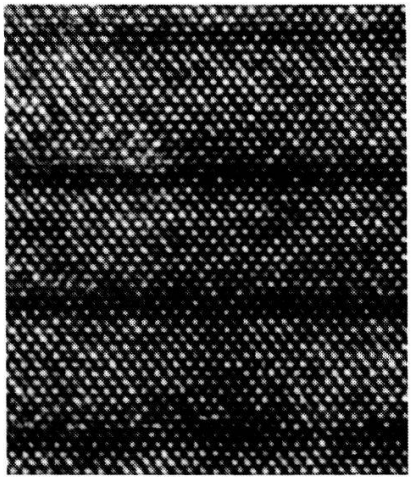

Fig.1

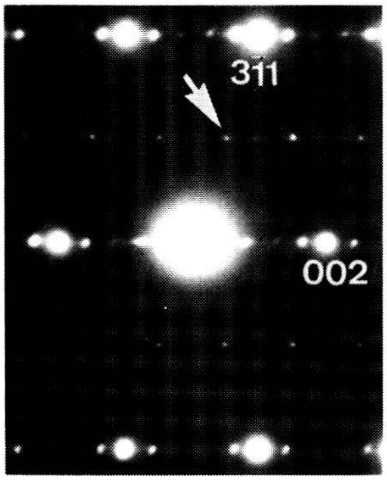

Fig. 2: as grown

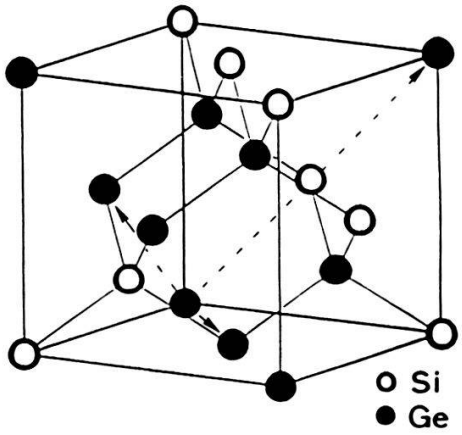

Fig. 3

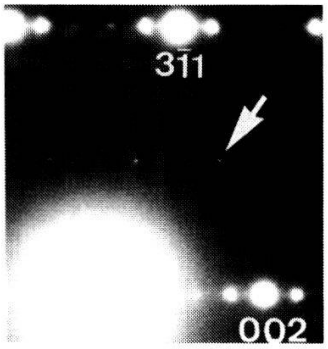

Fig. 4a: 550°C

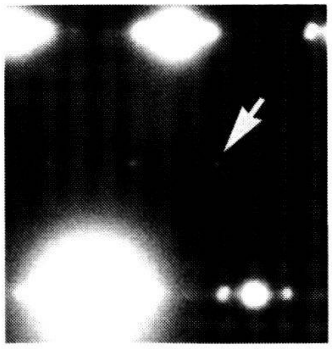

Fig. 4b: 575°C

Fig. 4c: 600°C

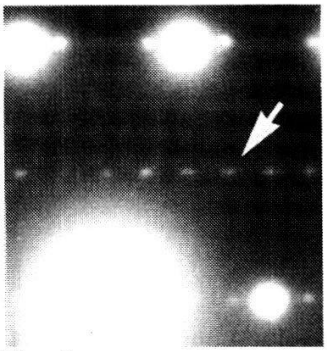

Fig. 5a: as grown

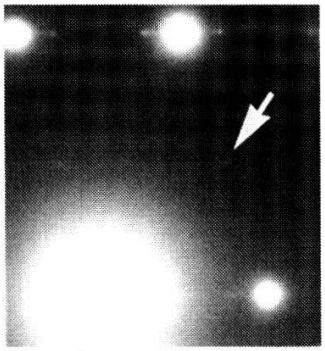

Fig. 5b: 575°C

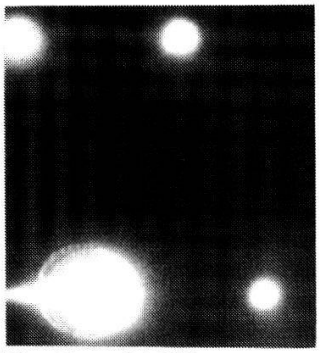

Fig. 5c: 600°C

12-FOLD SYMMETRIC 2D TILINGS BY TWO PENTAGONS OR TWO QUADRANGLES

H.-U. Nissen, Festkörperphysik, ETH Zürich, CH-8093 Zürich

Abstract: We present new dodecagonal quasiperiodic tilings by two pentagons as well as by two quadrangles.

The projection [1] of a 4d lattice into 2d as well as the de Bruijn grid technique [2] have allowed to construct quasiperiodic tilings with 12-fold symmetric Fourier transform describing the properties of dodecahedral quasicrystals [3]. One of them, the shield tiling, a tiling by squares, triangles and "shields" [1], is the basis for constructing the two-pentagon tiling (Fig. 1): A σ-pentagon, occurring e.g. as a planar unit of the σ-phase alloys is placed at each vertex of the shield tiling so that σ-pentagons cover the plane except for small gaps constituting the second tile which has nonconvex pentagon shape. The orientation of the σ-pentagons is determined as follows: The 4d lattice points corresponding to the vertices of the shield tiling, when projected into the space orthogonal to the tiling space, fall into a dodecagon-shaped acceptance region which is divided into 12 sectors. Each sector corresponds to one of the 12 orientations of any σ-pentagon.

A dodecagonal tiling by two quadrangles can be generated by replacing each vertex of the shield tiling by a "house". After enlarging all houses until they are in contact along their edges, the remaining voids can be covered either by pairs of the second quadrangle ("wedges") or by combinations of half a house and half a wedge. After dissecting all houses into 4 congruent quadrangles, the dodecagonal quasiperiodic tiling of Fig. 2 results. Both the two-pentagon tiling (Fig. 1) and the two- quadrangle tiling have a single infinite line of mirror symmetry and are quasiperiodic. Both tilings can be used in crystallographic investigations of dodecagonal quasicrystals.

References

[1] F. Gähler, In: Quasicrystalline Materials, ed. Ch. Janot, J.M. Dubois, (World Scientific, Singapore, 1988) p. 272.

[2] P. Stampfli, Helv. Phys. Acta 59, 1260 (1986).

[3] T. Ishimasa, H.-U. Nissen, F. Fukano, Phil. Mag. A 58, 835 (1988).

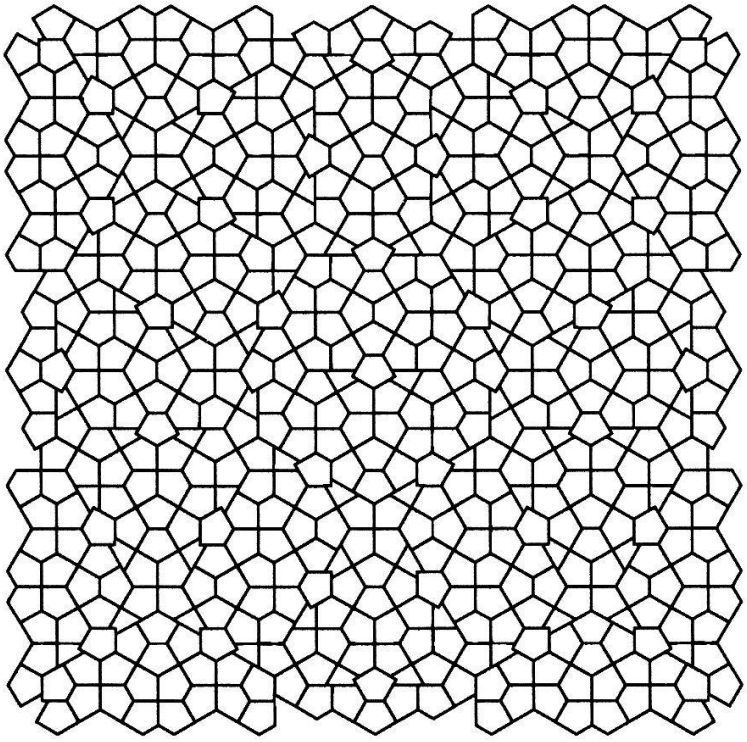

Fig. 1

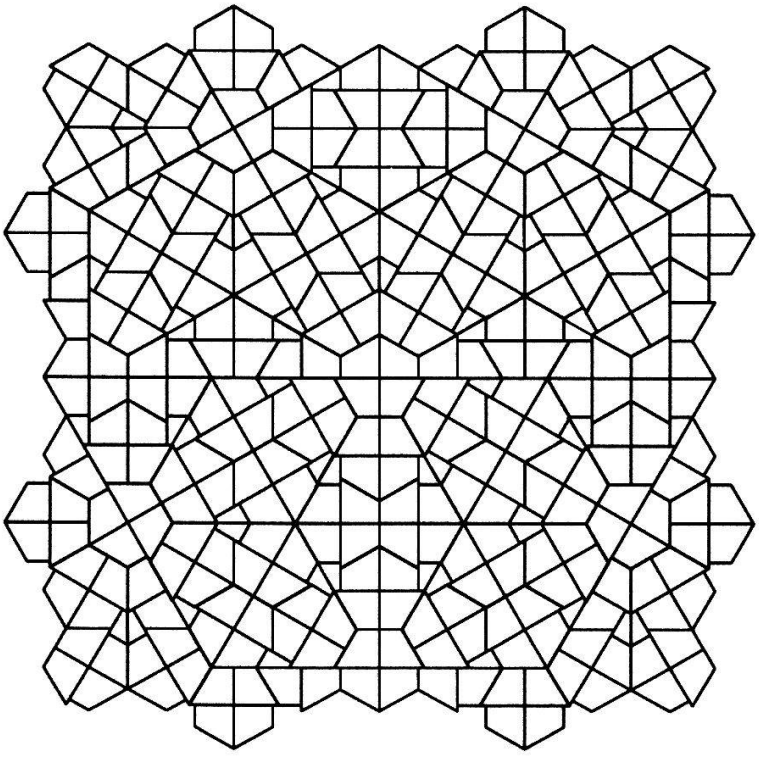

Fig. 2

Pattern Formation on the Surface of a Frozen Lake

P. Hildebrand, B. Merté, E. Lüscher
Department of Physics E13, TU Munich, James-Franck-Str., D-8046 Garching

Abstract
Typical phenomena of pattern formation as self-amplification and self-similarity within a certain range of length scales, can not only be found experimentally, but also as naturally ocurring examples as in the present case. The Hausdorff-Besicovich-dimension D_f is, as expected, comparable with the fractal dimension of other 2-dimensional diffusion-like processes.

Observing ice-surfaces of frozen lakes in winter, one can see cracks, typically netted over the whole lake and forming loops. However, in some special cases, nature produces several separated dendritic structures having no connections in between, as shown in figure 1.

1. Appearances of Dendritic Patterns

Dendritic structures on ice-surfaces may be observed in a region up to 150 m from the shore; they are isolated and have a maximum size of about 60 cm.
These dendritic patterns can be qualitatively generated by computer simulations based on a simple model.

figure 1:

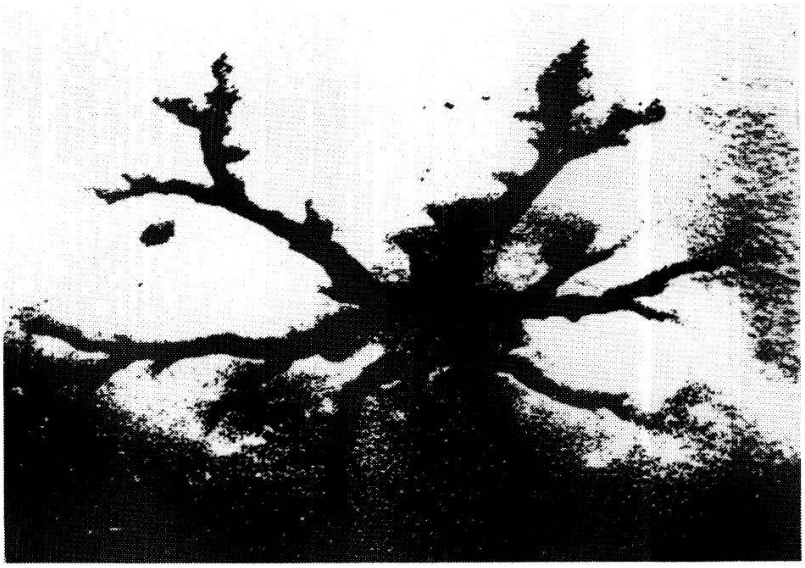

2. Presuppositions for Forming Dendritic Structures on Ice-surfaces

The question can be asked, as to why there are no dendritic patterns to be seen on several lakes in the same region, having the same temperature-history? On this lake, in one region, bubbles of gas were being produced by exothermal decays, which rise up from the ground at a temperature higher than $4°C$, (the temperature of water with highest density).

As the water-layer is rather thin near the shore, where the patterns are formed, they reach the surface at a temperature T_0 above $T_{ice} = 273.15K$, being able to form the ice on the long run. The lower surface represents a potential $V(\vec{r}) \sim z(\vec{r})$ causing some kind of competing interaction: Having reached the surface, the bubbles "walk" - driven by the buoyancy - along the gradient lines of the ice layer to a local minimum of the thickness - modifying the ice layer by a delivery of thermal energy. We have in addition a hampering force in the friction combined with small fluctuations in thickness:

$$\vec{F} = \vec{F}_f + \vec{F}_b = -\gamma\dot{\vec{r}} + \alpha \cdot \vec{\nabla}V(\vec{r}, t)$$

If T_0 is the temperature of the bubble at the moment of contact with the ice-layer, the delivered heat is

$$Q = -\int_{T_{ice}}^{T_0} C dT$$

and therefore for the case of slow delivery of heat $Q = C \cdot (T_{ice} - T_0)$.
Once used paths that deformed the ice-layer locally are attractors for future paths: A self-amplifying process is started, a randomly choosen point becomes the center of a growing dendrite. Bubbles coming from the outside are lead on existing paths to the center, extending the path. Conditioning the surface is supported by the gradient of temperature that leads to cracks, preferentially in the thinnest regions. The area of the dendrite's center is superior to that of, for example, a DLA-structure formed by diffusion and sticking to the cluster /4/. In our case we have an accumulation of bubbles in one region, mixing diffusion and conduction. In spite of the different appearance, the fractal dimension D_f of dendrites in ice is $D_f = 1.66 \pm 0.03$ - just like the case of DLA. The fractal dimension has been determined by box-counting and is illustrated in figure 2. Simulations based on the above equations show, that ramified structures are formed.

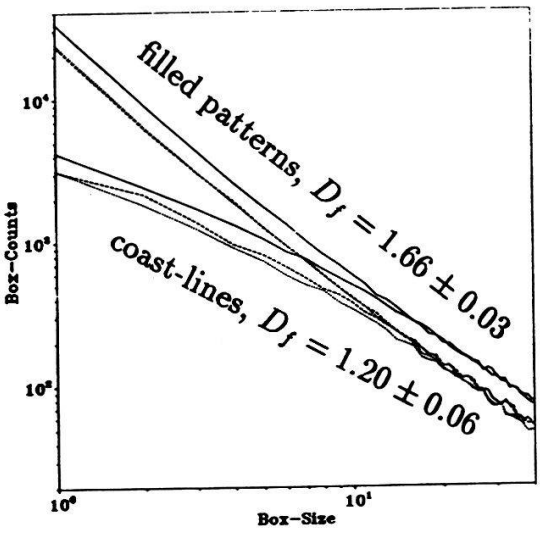

figure 2: Results of Box-Counting

Literature:

/1/ P. Hildebrand, diploma thesis, Dept. of Physics E 13, TU-Munich (1989)
/2/ B. Mandelbrot, The Fractal Geometry of Nature, Freeman, San Francisco 1983
/3/ L.M. Sander, Fractal Growth, Scientific American, **256**, 1, 82 (1987)
/4/ T.A. Witten, L.M. Sander, Phys. Rev. Lett. **47** 1400 (1981), Phys. Rev. B **27**, 5686 (1983)

Stationary Dendritic Structures in an Electric Field

G. Hadwich, B. Merté+, A. Hübler*, E. Lüscher
Physik-Department E 13, Technische Universität München, D-8046 Garching
* CCSR, University of Illinois, USA

+ part of Ph.D. thesis

1. Abstract

Under the influence of an electric current dendritic patterns are cooperatively formed by small metallic spheres in a viscous insulating fluid (oil). A large and isotropic frictional force causes the system to reach a stable stationary state characterized by minimal potential energy and by minimal dissipation /1/. The characteristic properties of the dendritic strutures are evaluated as a function of time and of the growth parameters.

2. Theory

The *Poisson* equation $\Delta\varphi = S_0/\sigma_0$ (φ: electric potential, S_0: constant source term, σ_0: specific conductivity of the oil) ensues from *Ohm*'s law $\vec{j} = \sigma_0 \vec{\nabla}\varphi$ ($\vec{j}$: current density) and from charge conservation $\dot{\rho} = -\vec{\nabla}\vec{j} + S_0$ (ρ: charge density) combined with $\dot{\rho} \approx 0$ (Relaxation time $\tau_{mechanical} \gg \tau_{electrical}$, see below).

The electric potential energy can be written as $W = \frac{1}{2}\varepsilon \iint_A (\vec{\nabla}\varphi)^2\, dx\, dy = \varepsilon\, S_0\, \bar{\phi}/2\sigma_0$ (ε: dielectric constant, A: surface of the oil, $\bar{\phi} = \iint_A \varphi\, dx\, dy$). The equation of motion describing particle $\#i$ is $-\gamma\, \dot{\vec{q}}_i - \vec{\nabla}_{\vec{q}_i} W = 0$ ($\vec{q}_i$: position of particle, γ: damping constant). As γ is very large, the electrical degrees of freedom ($\tau_{electrical}$) are slaved by the mechanical ones ($\tau_{mechanical}$) /2/. Thus a stationary state is attained: $\dot{\vec{q}}_i = 0 \;\Rightarrow\; \vec{\nabla}_{\vec{q}_i} W = 0 \;\Rightarrow\; W$ extremal. Furthermore, W is a *Lyapunov* function of the system, that is the stationary state is stable, W is minimal. Thus the dissipation P_D is also minimal: $P_D = \iint_A \vec{j}\,\vec{\nabla}\varphi\, dx\, dy = S_0\, \bar{\phi} = 2\sigma_0\, W/\varepsilon$.

3. Experimental Results

Charges from a spike electrode set to a high voltage of $12.5\text{kV} \le U \le 25.0\text{kV}$ are sprayed almost homogeneously onto the surface of an oil layer (thickness 3mm, in an acrylic dish of $\oslash$ 114mm) $h = 4$cm below it /3/. Dendritic structures are formed by $N_{tot} = 600$ metallic spheres ($\oslash$ 2mm, initially statistically distributed in the oil layer) conducting these charges to a earthed ring electrode at the inner border of the dish. The following macroscopic quantities characterizing this structure are solely a function of the growth parameters U and h: The number N of earthed spheres, the number M of open ends, the "fractal dimension" D_F calculated by a *box counting* algorithm and the dissipation P_D determined by a numerical solution of the *Poisson* equation.

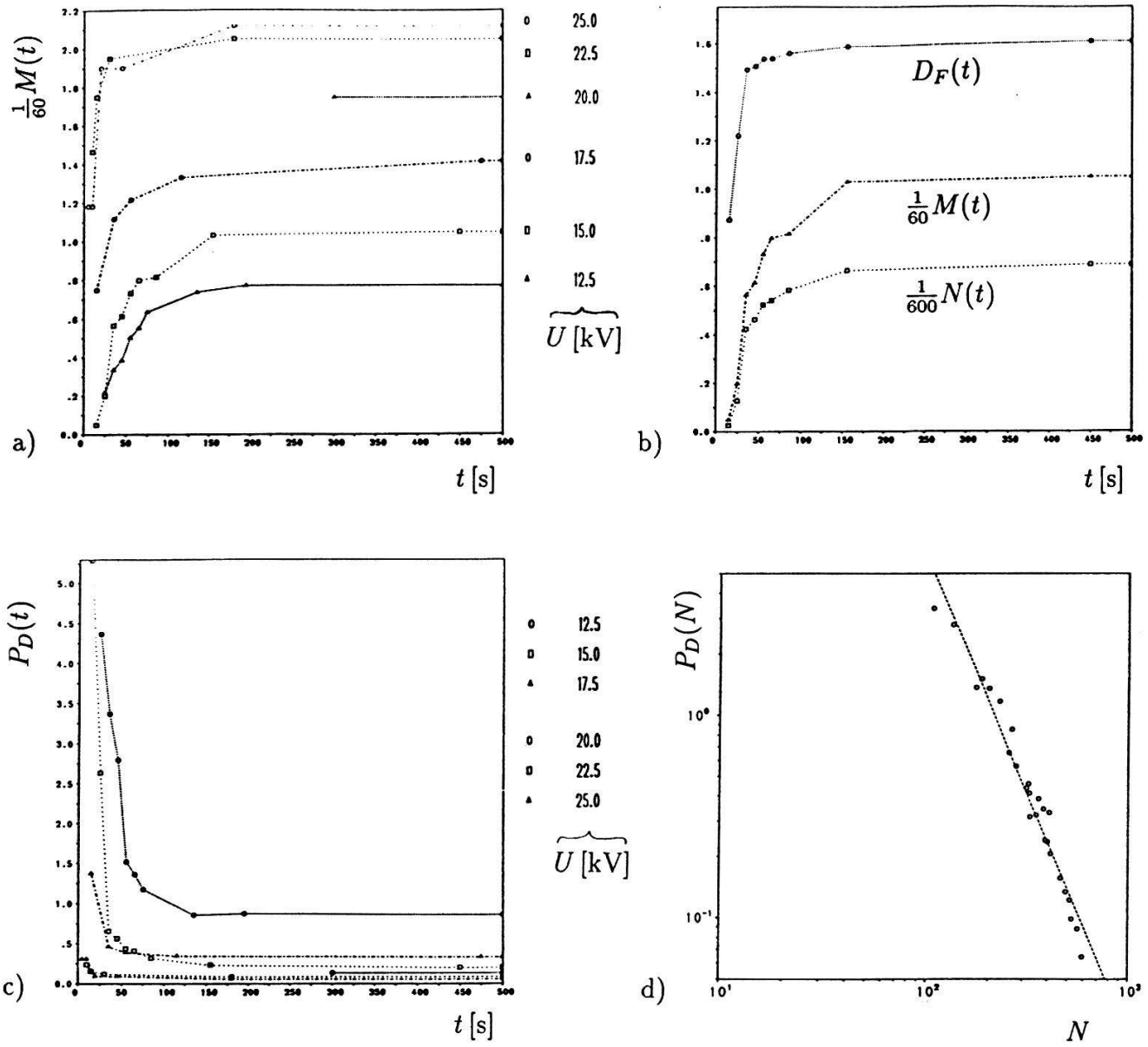

Figure: Time dependence a) of M measured at different growth parameters $12.5\text{kV} \leq U \leq 25.0\text{kV}$, b) of M, N and D_F measured at $U = 15.0\text{kV}$, c) of P_D at $12.5\text{kV} \leq U \leq 25.0\text{kV}$.
d) Logarithmic plot of $P_D(N)$. /3/

The characteristic quantities attain their stationary value more rapidly if a higher U is applied. The following proportionalities have been evaluated /3/: $M \sim N \sim D_F$ and $P_D \sim M^{-\alpha} \sim N^{-\alpha}$, $\alpha = 2.35 \pm 0.4$.

4. References

/1/ B.Merté, P.Gaitzsch, M.Fritzenwanger, W.Kropf, A.Hübler, E.Lüscher, Stable Stationary Patterns with Minimal Dissipation , Helv. Phys. Acta **61** (1988)

/2/ H.Haken, Advanced Synergetics, chapter 7, Springer, Berlin 1983

/3/ G.Hadwich, Extremaleigenschaften dendritischer Strukturen im elektrischen Feld, diploma thesis, Technische Universität München, 1989

DIFFERENT SPIN AND LATTICE TEMPERATURES OBSERVED BY SPIN-POLARIZED PHOTOEMISSION WITH LASER PULSES

D. Guarisco, A. Vaterlaus, M. Lutz, M. Aeschlimann, M. Stampanoni and F. Meier
Laboratorium für Festkörperphysik,ETH Hönggerberg,CH-8093 ZÜRICH

Abstract: From spin-polarization measurements with short laser pulses it is concluded that the melting of a Sn surface occurs faster than 68 ps and that the spin-lattice relaxation time in Fe is between 30 ps and 20 ns.

Due to the extreme surface sensitivity (≈ 20 Å) and the very short excitation time (≈ 10^{-16} s) spin-polarized photoemission is a powerful experimental technique for studying dynamic magnetization processes during short laser pulses. The experimental setup is described in Ref. [1]. For non-magnetic materials the emitted electrons are optically oriented from an unpolarized ground state using circularly polarized light [2]. The polarization is then fully determined by the symmetry properties of the lattice. For magnetically-ordered materials the polarization of the photoelectrons emitted with unpolarized light is proportional to the magnetization along the surface normal due to the spin conservation in optical dipole transitions.

A measurement of the spin-polarization as a function of the pulse energy from a cesiated β-Sn surface is shown in Fig. 1 a). The behaviour of the polarization is the same for both ns and ps pulses: it drops toward zero at the threshold energy for positive ion emission. Completely different results are obtained from a cesiated polycrystalline Fe surface (Fig. 1 b). For 20 ns pulses the polarization vanishes at or even before the onset of ion emission, whereas for 30 ps pulses it remains constant up to an energy of about 4 E_{ion}.

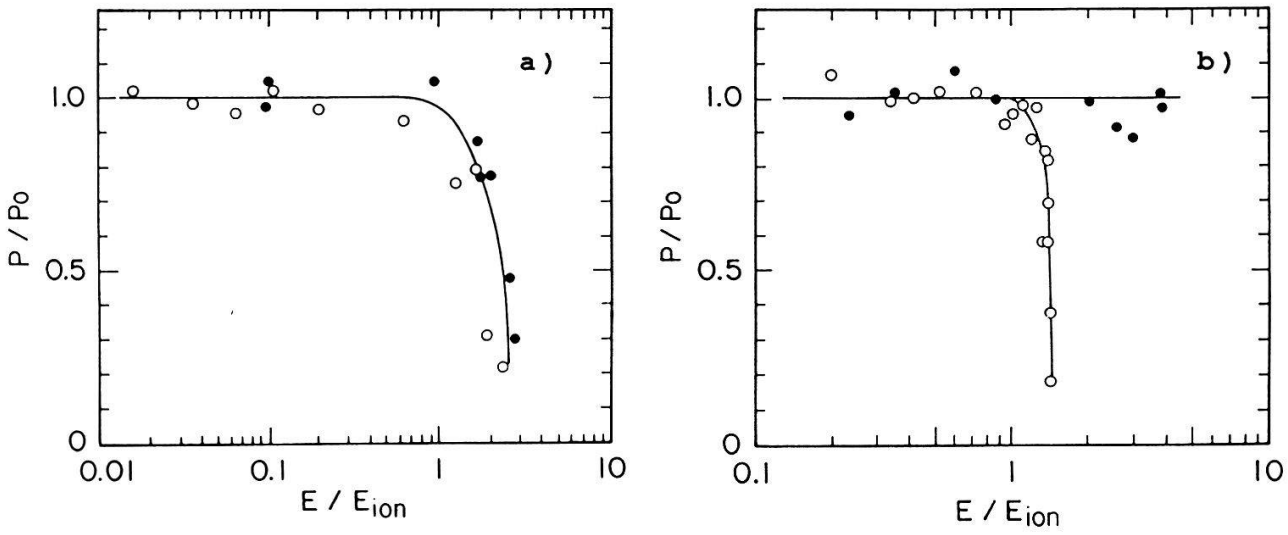

Fig.1 Spin polarization of the photoelectrons emitted from **a)** β-Sn (001) during 12 ns (open circles) and 68 ps (full circles) laser pulses ($h\nu = 2.7$ eV); **b)** iron in a magnetic field of 4 kOe during 20 ns (open circles) and 30 ps (full circles) laser pulses ($h\nu = 2.15$ eV) as a function of the pulse energy. P_0 is the polarization measured with a HgXe-lamp, E_{ion} is the threshold energy for positive ion emission.

When a high-intensity laser beam hits the surface of a solid the incident energy is first absorbed by the electron gas. The hot electron gas thermalizes with the lattice in a few ps. The energy is then transmitted from the lattice to the spin system [3]. From the above measurements on tin it is concluded that the melting of the surface occurs in a time scale which is short compared to the duration of a ps pulse and that positive ion emission indicates melting of the surface. From Fig. 1 b) it is seen that in iron the magnetic order is not destroyed by 30 ps pulses even if the lattice is molten. Therefore the spin-lattice relaxation time lies between the ps and the ns pulse duration.

References

[1] S.F. Alvarado, W. Eib, F. Meier, H.-C. Siegmann, and P. Zürcher, in: *Photoemission and the Electronic Properties of Surfaces*, eds. B. Feuerbacher, B. Fitton, and R.F. Willis (John Wiley, 1978).

[2] F. Meier, and D. Pescia, in: *Optical Orientation*, eds. F. Meier and B.P. Zakharchenya (North Holland, 1984).

[3] M.B. Agranat, S.I. Ashitkov, A.B. Granovskii, and G.I. Rukman, *Sov. Phys. JETP* **59**, 804 (1984).

Ein kompaktes Kraftmikroskop aufgebaut mit Laserdiode und positionsempfindlicher Photodiode

Jaime Colchero, Othmar Marti, Jürgen Mlynek
Institut für Quantenelektronik, Laboratorium für Quantenoptik,
ETH - Hönggerberg, 8093 Zürich

Ein kompaktes Kraftmikroskop (Durchmesser 6 cm, Höhe 10 cm) wird beschrieben. Das Licht einer Laserdiode wird auf einen mikrofabrizierten Federbalken (Länge l=100 μm) fokussiert und auf eine Zweisegment-Photodiode reflektiert. Der Laserstrahl wirkt so als Lichtzeiger; die Auslenkung des Balkens wird über den Differenzstrom der Zweisegment -Photodiode gemessen.

Mit der Erfindung des Kraftmikroskopes durch Binnig et al. [1] ist atomare Auflösung auch von nichtleitenden Oberflächen möglich geworden. Die Probe wird dabei rasterförmig an einem Federbalken vorbeibewegt. Dieser biegt sich auf Grund der entfernungsabhängigen Wechselwirkung Balkenspitze-Probe unterschiedlich stark. Eine genaue Beschreibung dieses Prinzips findet man in der Literatur [1,2].

Zentrales Problem beim Kraftmikroskop ist die höchst emfindliche Detektion der Balkenauslenkung [2]. Wir verwenden hierzu einen Lichtzeiger [3], der im folgenden näher beschrieben wird. Ein Lichtstrahl wird vom Balken auf eine Zweisegment-Photodiode reflektiert. Bei Auslenkung dieses Balkens um den Betrag Δh gilt für die Ablenkung ΔH des Lichtfleckes auf der Photodiode $\Delta H = 3\,{}^{L}\!/_{l}\,\Delta h = G\,\Delta h$, wo L die Länge des Lichtweges (Balkenspitze-Zweisegment-Photodiode) bezeichnet. Bei unserem Aufbau mit L=40mm und l=0.1mm ist die geometrische Verstärkung G=1200. Die Empfindlichkeit des Kraftmikroskopes mit Lichtzeiger ist ferner proportional zur von der Balkenspitze auf die Photodiode reflektierten Lichtintensität. Daher benötigen wir eine Lichtquelle von *hoher Leistung*, die sich möglichst vollständig auf die Balkenspitze *fokussieren* lässt. Ausserdem sollte die Lichtquelle - und das Kraftmikroskop insgesamt - *kompakt* sein; ein kleiner Aufbau liefert hohe Eigenfrequenzen und entkoppelt das höchst empfindliche Kraftmikroskop von äusseren Vibrationen. Laserdioden erfüllen diese Anforderungen optimal und erlauben darüberhinaus die direkte Modulation der Lichtintensität. Damit bietet sich die Möglichkeit einer Heterodyndetektion der Balkenauslenkung durch einfache Strommodulation der Laserdiode.

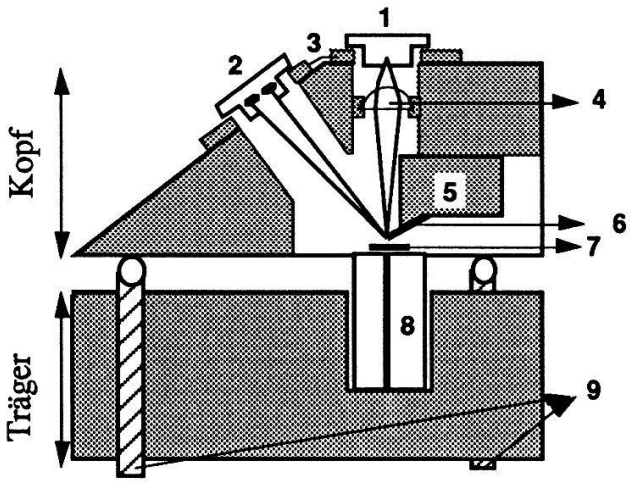

1 Laserdiode
2 Zweisegment Photodiode
3 verschiebbare Halterungen
4 Mikrolinse
5 Balkenhalterung
6 Siliziumhalterung mit mikrofabriziertem Balken
7 Probe
8 Piezoröhre
9 Feingewindeschrauben (insgesamt 3)

Im Kopf des Kraftmikroskopes (siehe Abbildung) befinden sich die Laserdiode, eine Mikrolinse die den Stahl auf den Balken fokussiert, die Balkenhalterung mit dem Balken, sowie die Zweisegment-Photodiode. Laserdiode und Photodiode lassen sich zur Justierung des Strahlenganges bewegen. Die Balkenhalterung kann vorgeschoben werden, um die Balkenspitze in den Strahlengang hineinzufahren. Die Probe wird von einer Piezoröhre gerastert; dabei bleibt der Balken auf konstanter Höhe. Zur Annäherung des Balkens an die Probe dienen drei Feingewindeschrauben. Da wir neben diesem Kraftmikroskop auch ein Rastertunnelmikroskop betreiben, verwenden wir dessen Elektronik zur Regelung der Kraft und zur Bilderzeugung.

Erste Bilder eines optisches Gitters sowie von "Quantum Dots" auf GaAs sind bereits erzielt worden, die Periodizität dieser Strukturen (200nm bzw 300nm) wurde gut aufgelöst Bei Optimierung unseres Aufbaus und geeigneten Proben sollte atomare Auflösung erreichbar sein.

Ein Lichtzeiger ist nicht das einzige optische Verfahren, um die Balkenauslenkung zu detektieren. Die interferometrische Detektion [4] ist experimentell aufwendiger, während das in [5] vorgeschlagene Verfahren (Rückkopplungsänderungen einer Laserdiode) schwer zu kontrollieren ist und ausserdem keine atomare Auflösung liefert. Unsere Ergebnisse zeigen dagegen, dass Kraftmikroskope mit Lichtzeiger sehr einfach und bedienungsfreundlich sind. Insbesondere bei Verwendung einer Laserdiode als Lichtquelle lässt sich ein solches Kraftmikroskop sehr kompakt bauen.

[1] Binnig, C.F. Quate, C. Gerber, *Phys. Rev. Lett.* **12**, 930 (1986)
[2] P.K. Hansma, V.B. Elings, O. Marti, C.E. Braker, *Science Vol* **242**, 157 (1988); und Referenzen darin
[3] S. Alexander, K. Hellemans, O. Marti, J. Schneir, V. Elings, P.K. Hansma, M.Longmire and J. Gurley, *J. Appl. Phys.* **65**, 164 (1989)
[4] Mc Clelland et al.; J.Vac. Sci. Tecnol. A6, 266 (1986)
[5] D. Sarid et al., Opt. Lett. 13, 1057 (1988)

DC Size Effects measurements in Aluminium up to 30 K

J Romero, T Fleischer and R Huguenin
Institut de Physique Expérimentale, Université de Lausanne, BSP,
1015 Lausanne, Switzerland

Previous high resolution measurements up to 9 K of the electrical resistivity of a monocrystalline Al sample showing size effects are being completed by extending the temperature range up to 30 K and keeping the resolution high (50 ppm) at this temperature. This has been possible using high T_c superconductors (HTSC) as parts of the wiring circuit in a bridge working with a direct current comparator and a rf SQUID as null-detector. This constitutes a practical application of HTSC in an electrical circuit in which no high density current flows. The sample surface was changed from rough to polished in a controlled and reproducible way by electropolishing and chemical treatments, showing that scattering at the sample surface is partially specular in contrast to the usual assumption of diffuse scattering.

When interpreting data on the temperature dependence of the surface resistivity $\rho_s(d,T)=\rho(d,T)-\rho(\infty,T)$ of Al with the current theories [1], one must take into account the specularity p which could be, as shown [2], different from 0. Recent works [3], [4] observed that a T^2-behaviour of $\rho_s(d,T)$ exists for $15 \leq T \leq 30$ K with a coefficient up to 35 $f\Omega m K^{-2}$. The lower values can be confused with the e-e contribution in Al whose existence has been established experimentaly by Ribot et al. [5]. Notwithstanding, the magnitude for thinner samples and the T-domain of the T^2-contribution from the surface is different from the e-e contribution. Furthermore, the former is strongly affected by dislocations [6] and it has not yet been shown how the specularity influences it. Sambles and Elsom [4] have shown that its thickness-dependence was as $d^{-2/3}$. In this work we present preliminary results which have been carried out on a monocrystalline Al sample thinned by alternative etching and polishing, keeping in this way the same bulk properties at the successive thicknesses.

We measured $\rho(d,T)$ in a high resolution bridge with a direct current comparator and a SQUID as null-detector. Usually, in order to keep the resistance low in the input circuit to the SQUID, copper cladded Nb-Ti superconducting wires with $T_c \approx 9$ K are used. To overcome this limitation and reach higher temperatures, we have improved the wiring circuit by inserting high T_c superconductors in order to uncouple thermally the sample from the input circuit to the SQUID, the former reaching 30 K and the later been kept at 4.2 K [7]. In this reference a method is indicated to make the contacts between the sample and the HTSC. The resolution obtained in the bridge was 1 ppm at 4.2 K and dropped to 50 ppm at 30 K. This last value of the temperature is not limited and is due to the thermal stability of the sample taking a long time. The sample surface was polished and etched in a controlled way.

Typical results are presented in Fig. 1 where the temperature-dependent part of

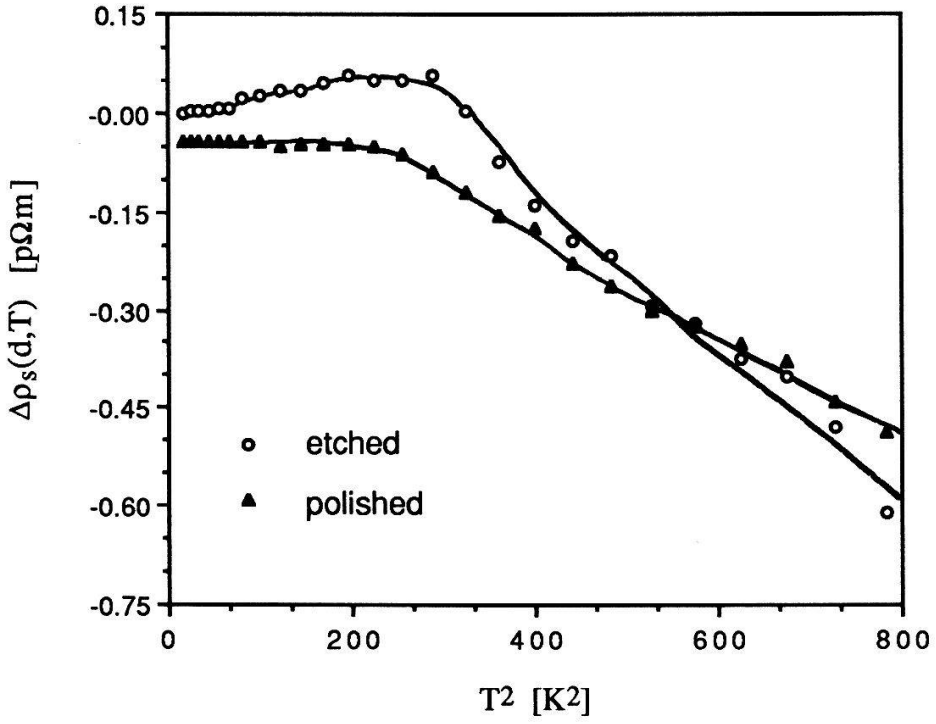

Figure 1. *Temperature-dependent part of the surface resistivity $\Delta\rho_s(d,T)$ as a function of T^2 for a polished (thickness d=910 μm) and an etched (thickness d=920 μm) state of the surface of an Al sample with RRR=17000. The lines are to guide the eye.*

the surface resistivity $\Delta\rho_s(d,T)=\rho_s(d,T)-\rho_s(d,T=0)$ is shown for an etched and a polished state of the surface of two close thicknesses. A T^2-behaviour is noticeable above ~15 K, the coefficient being ~1 $f\Omega mK^{-2}$. It is not clear whether this surface contribution results from an intrinsic mecanism in Al as a tangential Umklapp scattering suggested by Sambles and Elsom [4] or derives from the bulk T^5-behaviour both due to the presence of the surface. But the important fact is that a distinction can be made between polished and etched states of the surface up to high temperature and must be taken into account when a comparison with the theory is made to deduce e. g. $\rho_\infty\lambda_\infty$ values from experiment.

The financial support of the Swiss National Science Foundation is gratefully acknowledged.

References

[1] Soffer S B, J Appl Phys 38 1710 (1967)
[2] Romero J and Huguenin R, Helv Phys Acta 62 758 (1989)
[3] van der Maas J, Huguenin R and Rizzuto C, Physica 107 B 139 (1981)
[4] Sambles J R and Elsom K C, J Phys F : Met Phys 15 161 (1985)
[5] Ribot J H J M, Bass J, van Kempen H, van Vucht R J M and Wyder P, Phys Rev B 23 532 (1981)
[6] Romero J and Huguenin R, Helv Phys Acta 61 837 (1988)
[7] Romero J, Fleischer T and Huguenin R, accepted by Cryogenics (1989)

Radio-Frequency-Size-Effect measurements of the scattering rates in Cd below 1 K.

A. Jaquier, P-A Probst and R. Huguenin.
Institut de Physique Expérimentale, Université de Lausanne, BSP, CH-1015 Lausanne.

Introduction

Previous measurements[1,2] show that the scattering rate $\nu(T)$ of the electrons on the lens of the Fermi Surface of Cd vary approximately like T^5 . This has been attributed by Myers et al.[1] to the phonon wave vector being too small at low temperatures to scatter the electrons effectively, and alternatively by Probst et al.[2] to intersheet scattering with an orbit dependent gap temperature (T_{gap}). The latter interpretation would predict a T^3-law when $T \rightarrow 0$. On second zone orbits $\nu(T)$ includes a large T^2 term whose origin is not clear. $\nu(T)$ measurements from 5 K down to 0.2 K were made to investigate these points.

Experimental details

The RFSE[3] measurements are made using a marginal oscillator[4], a modulated dc magnetic field and a digital lock-in amplifier[5] for signal detection. Under good conditions the resolution on the amplitude is 10^{-4} . Temperatures below 1K are obtained with a dilution refrigerator. The temperature is measured with GE thermometers and is controlled digitally[6] with a precision < 1mK. The samples are single crystals cut from 6N rods. The first one is 527 μm thick with normal n parallel to $(11\bar{2}0)$, the second 310 μm and n = $(10\bar{1}0)$. The orientations are choosen so that the electron orbits are symmetrical.

Measurements

Elliptical lens orbit. The scatering rate behave clearly as $\alpha T^2 + \beta T^3$ (see figure) below 2 K. The fitted values of the parameters are $\alpha = 7.7 \pm 0.1$ MHz K^{-2} , $\beta = 5.05 \pm 0.1$ MHz K^{-3} . Above 3 K, $\nu(T)$ varies like T^n with $n \approx 4.9$.

Orbit n[2]. This orbit is part of the second zone monster. $\nu(T)$ is well fitted by $\alpha T^2 + \beta T^3$ over the whole temperature range, with $\alpha = 8.3 \pm 0.1$ MHz K^{-2} , $\beta = 22.3 \pm 0.1$ MHz K^{-3} .

Orbit m . It is a second zone triangular orbit surrounding the first zone orbit l. The resolution is less good here making extrapolation of the amplitude to T = 0 K more difficult. The behaviour of $\nu(T)$ is however consistent with $\alpha T^2 + \beta T^3$ where $\alpha \approx 50$ MHz K^{-2}, $\beta = 45$ MHz K^{-3}.

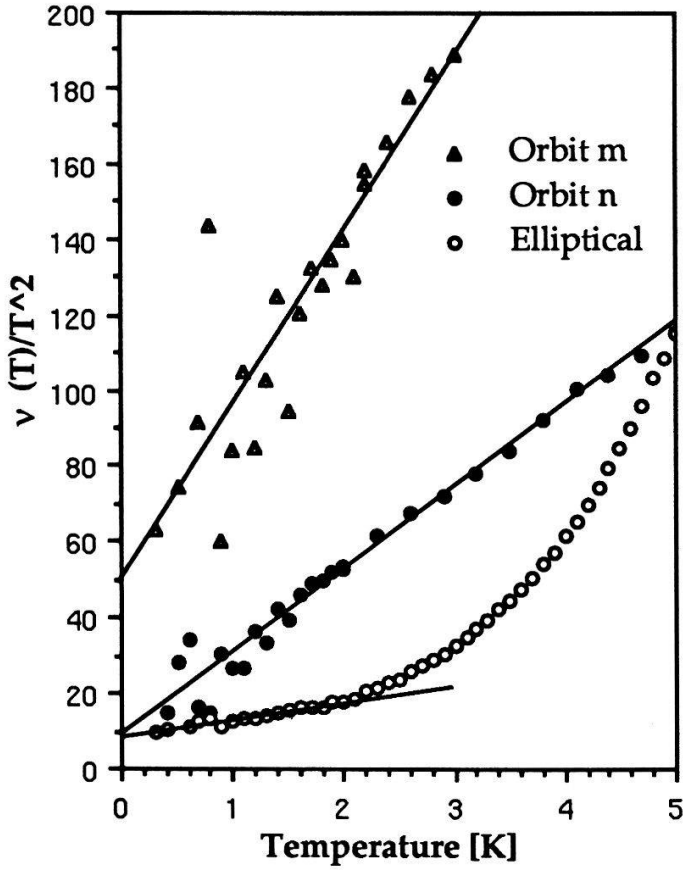

Orbit m : second zone, B //0001 + 10°, n // (10$\bar{1}$0), d = 310μm, $\alpha \approx 50$ [MHz K^{-2}], $\beta \approx 45$ [MHz K^{-3}]

Orbit n : second zone, B // 0001 + 10°, n // (10$\bar{1}$0), d = 310 μm, $\alpha = 8.3 \pm 0.1$ [MHz K^{-2}], $\beta = 22.3 \pm 0.1$ [MHz K^{-3}]

Elliptical Orbit : third zone lens, B ⊥ 0001 , n // (11$\bar{2}$0), d = 527μm, $\alpha = 7.7 \pm 0.1$ [MHz K^{-2}], $\beta = 5.05 \pm 0.1$ [MHz K^{-3}]

Conclusions

Ineffectiveness of scattering cannot provide explanation for the low temperature behaviour of ν(T) on the elliptical orbit; it would lead indeed to a T^5 temperature dependence down to 0 K, which is not experimentally observed. On the other hand the rapid variation of ν(T) with T above 2.5K can be interpreted by intersheet scattering with $T_{gap} \approx 25$ K. The term α has the right order of magnitude to be attributed to electron-electron scattering, being about 3 times larger than the theoretical prediction by Lawrence[7], and 50 % higher than Mc Donald's calculations[8] On the second zone the value of α is close to that of lens electrons for the n orbit, whereas it is 6 times larger for the m orbit. The origin of this large T^2 term is not settled yet.

---

[1]A Myers, R Thompson and Z Ali, J. Phys. F: Met. Phys. **4**, 1707 (1974)

[2]P A Probst, W M MacInnes and R Huguenin, J. Low Temp. Phys. **41**, 115 (1980)

[3]D K Wagner and R Bowers,Adv. in Phys. **27**, 651 (1978).

[4]P A Probst, B Collet and W M MacInnes,Rev. Sci. Instr. **47**, 1522 (1977).

[5]P A Probst and B Collet,Rev. Sci. Instr. **56**, 466 (1985).

[6]P A Probst and J Rittener,HPA **62**, 298-301 (1989).

[7]W E Lawrence, J W Wilkins, Phys. Rev. B. **7**, 2317 (1973)

[8]A H MacDonald and D J W Geldart, J. Phys. F : Met. Phys. **10**, 677 (1980)

Photoacoustic Investigation of Thermal Diffusion on Random Structures

R. Haberkern, R. Osiander*, P. Korpiun and E. Lüscher
Phys. Dept. TU München, Inst. E13, D–8046 Garching, James–Franck–Str.

The photoacoustic signal of random structures as powdered samples is interpreted within the framework of fractals. From the modulation frequency dependence a frequency dependent thermal diffusivity is calculated.

The Photoacoustic Effect:

If a solid sample is periodically illuminated with light so–called heat waves, strongly damped wave like solutions of the heat diffusion equation, travel from the surface into the sample as well as into the gas /1/. For the thermal conductivity λ, the density ρ and the specific heat c_p the temperature modulation in the gas ($n = 0$) and the sample ($n = 1$) is $T_n(z,t) \propto \exp\{-(-1)^n(1+i)z/\mu_n+i\omega t\}$ with $\mu_n = \sqrt{2\alpha/\omega}$. Here $\alpha_n = \lambda/c_p\rho$ is the thermal diffusivity, $f = \omega/2\pi$ is the modulation frequency of the light. A contribution to the signal only comes from a few thermal diffusion lengths μ_1. In a homogenieous material this length depends on the frequency as $1/\sqrt{\omega}$ and thus offers the possibility of varying the depth of resolution of the experiment. If the thermal properties of the sample are a function of space this will lead to a special frequency dependence.

To detect the temperature modulation we have used the photoacoustic effect /1/. In a closed gas volume (1 ccm) the temperature wave in the gas leads to a pressure modulation which can be detected by a microphone in the audio range ($1\ \text{Hz} < f < 18\ \text{kHz}$). The temperature at the surface is proportional to the energy release ($\propto 1/\omega$) per volume ($\propto \mu_1$). For the photoacoustic effect the temperature wave in the gas must be integrated over the gas volume and gives a photoacoustic signal proportional to $\omega^{-3/2}/\mu_1$.

Thermal diffusion on fractals:

The concept of fractals /2/ has been successfully used to characterize random structures. The density of a fractal depends on the applied yardstick by a non integer exponent called the "fractal dimension" d_f. The geometrical structure seen by the diffusing heat depends on the elapsed time, the diffusion coefficient α becomes time

dependent. Alexander and Orbach /3/ have introduced the spectral dimension $\bar{d}$ in the scaling exponent of the diffusion coefficient. Its fourier transformed form, used in the photoacoustic effect has the form $\alpha(\omega) \propto \omega^{1-(\bar{d}/d_f)}$ /4/. It should be observable between a lower length, where the diffusion length is smaller than the smallest structure, and an upper length larger than the correlation length /3/ where the sample appears homogeneous.

Experiments:

We have measured the frequency dependence of the photoacoustic signal on graphite powders with grain sizes of about 10 μm and 80 μm as shown in figure 1. For $\mu/d < 1$ and $\mu/d > 1000$ the slope in the logarithmic plot is 2 corresponding to a frequency dependence of $1/\omega$ for an euclidean sample. Between those limits the slope is 2.3. The exponent $\bar{d}/d_f$ that can be calculated from this is 0.35. For a percolating network one would expect $\bar{d}/d_f = 0.52$.

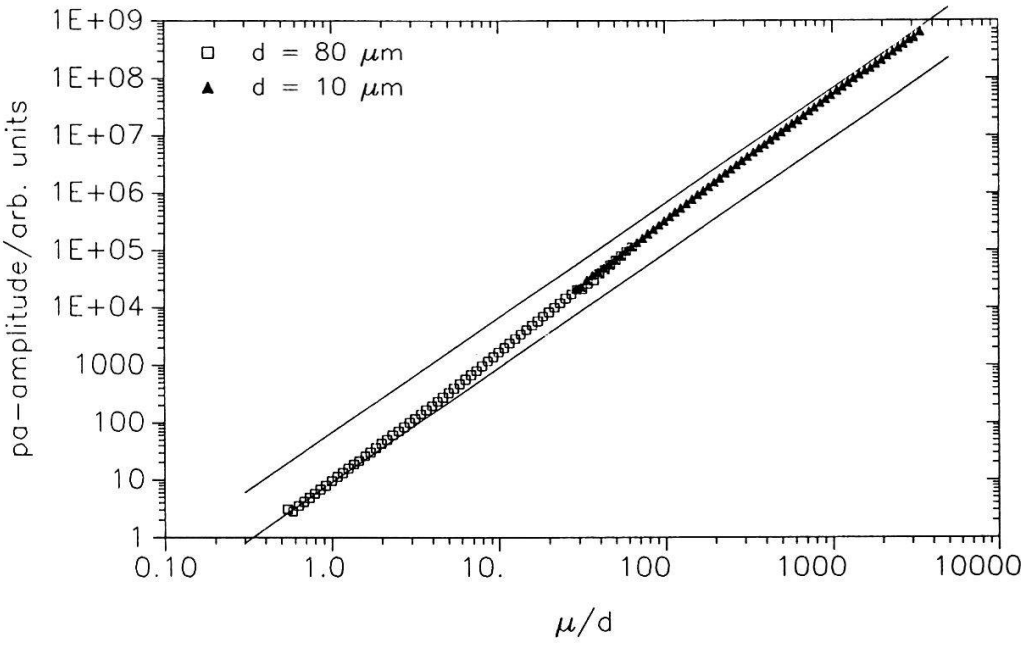

Figure 1: PA–amplitude versus diffusion length / grain size for graphite powder

References:

/1/ A.Rosencwaig, Photoacoustics and Photoacoustic Spectroscopy, Wiley, New York (1980)
/2/ B.Mandelbrot, The Fractal Geometry of Nature, Freeman, New York (1983)
/3/ R.Orbach, Science 231, 814 (1986)
/4/ R.Osiander, R.Haberkern, P.Korpiun, W.Schirmacher, to be published

* part of Ph.D.thesis

ERA-MEASUREMENT OF THE H-CONCENTRATION IN a-Si:H AS A FUNCTION OF THE ANNEALING TEMPERATURE

X.-M. Tang, J. Weber, Institut de Physique de l'Université, rue Breguet 1, CH-2000 Neuchâtel
F. Finger, V. Viret, Institut de Microtechnique de l'Université, rue Breguet 2, CH-2000 Neuchâtel

Abstract : we have measured by the Elastic Recoil Analysis method (ERA) the concentration profiles of hydrogen in amorphous silicon a-Si:H between 25 °C and 500 °C. Up to 280 °C, the H-concentration is constant and uniform in depth. From 280 to 305 ° C there is a fast "H-evaporation". Above 350 ° C, the H-evolution is governed by a diffusion process.

1. Introduction

The hydrogen concentration in amorphous silicon films is known to play an important role in the electronic properties of this material [1]; it should also be important in the silicide formation and/or diffusion processes [2]. From hydrogen evolution studies on undoped a-Si:H films it is concluded [1] that, depending on the preparation conditions and particularly on the substrate temperature Ts, hydrogen "evaporates" from a-Si:H with different rates at temperatures around 300 °C and 600 ° C. Each peak is related to different hydrogen phases [3]. One can expect, for a-Si:H samples prepared at a moderate temperature Ts, two domains of H-concentration: one below and one above 300 °C. One expects also that, in the first domain, the concentration profiles will not depend on the temperature. The purpose of this experiment was to confirm these two domains with respect to the in depth H-concentration profiles.

2. Experimental procedure, data analysis and results

The a-Si:H thin films were prepared by the Silane based VHF-Glow Discharge method (VHF-GD) recently developed [4,5]. Films of about 5 μm thickness were deposited on polished

Si<100> wafers. We have used the Elastic Recoil Analysis (ERA) method to determine the H-concentration profiles. Simultaneously, the He beam current was measured and the scattered α were detected (RBS). The samples were fixed onto a samples holder that could be heated by IR radiation. Samples were annealed for 30 min. at 14 different temperatures between 25 °C and 500 ° C. The measured profiles show that up to 280 °C the H-concentration is uniform in depth and constant. At 305 ° C the concentration has dropped by a few at. % but is still uniform. This situation persists up to 350 ° C. Above 350 ° C, the profiles are no longer uniform, the surface region being the first to be hydrogen depleted. This indicates that the H-evolution is then controlled by a diffusion process in concordance with [1].

3. Aknowledgment

This work has been supported by the FNSRS.

4. References

[1] W. Beyer, in "Tetrahedrally-Bonded Amorphous Semiconductors", D. Adler and H. Fritzscher, eds., Plenum Press, New-York (1985), p. 129.

[2] X.-M. Tang, J. Weber, Y. Baer and M. Favre, Helv. Phys. Acta 62 (1989) 235.

[3] R. A. Street, C.C. Tsai, J. Kakalios and W.B. Jackson, Phil. Mag. 56 (1987) 305.

[4] H. Curtins, N. Wyrsch and A.V. Shah, Elec. Lett. 23 (1987) 228.

[6] M. Favre, H. Curtins and A.V. Shah, J. Non-Cryst. J. Non-Cryst. Sol. 97/98 (1987) 731.

HYDROGEN DIFFUSION IN a-Si:H

X.-M. Tang, J. Weber, Institut de Physique de l'Université,
rue Breguet 1, CH-2000 Neuchâtel
F. Finger, V. Viret, Institut de Microtechnique de l'Université,
rue Breguet 2, CH-2000 Neuchâtel

Abstract : we have measured by ERA, the hydrogen diffusion constant D at 400 °C in five a-Si:H/c-Si samples of nominal H-concentration ranging from 11 to 18 at. %. We have found that the lower the H-concentration, the larger is D. We suggest that this behaviour is due to the variation of the microvoid concentration in the films.

1. Introduction

The motion of hydrogen in a-Si:H is believed to play an important role in the kinetics of the metastable defects. It has been studied by various authors and techniques [1-4]. In the preceding communication (this issue), we have given our results about the evolution of the H-concentration profiles in the 25 to 500 °C temperature range. We present here the results of our ERA (Elastic Recoil Analysis) study of the hydrogen diffusion in undoped a-Si:H films.

2. Experimental

Five undoped a-Si:H films (1 to 2 μm thick) were prepared by the Silane based VHF-Glow Discharge (VHF-GD) method [5,6]. During the depositions, the Si<100> substrates were kept at temperature Ts : 50, 100, 150, 200 and 250 °C resp. in order to study the influence of Ts on the hydrogen content and bonding structure in the films. Our experimental set up enabled us to detect simultaneously elastically recoiled protons (ERA) and scattered alphas (RBS). Annealings could be made in situ. We have ckecked our ERA procedure by measuring the H-concentration of a hydrogen standard.

3. Results

The H-concentration profiles of as-deposited films were uniform throughout the measurable depth (about 1 μm). These concentrations -in at. %- were : 17.7 (Ts = 50 °C), 17.4 (Ts = 100 °C), 16.0 (Ts = 150 °C), 13.8 (Ts = 200 °C) and 11.5 (Ts = 250 °C). Through the analysis of the profiles, after annealing at 400 °C for 30', the value of the diffusion constant D in function of Ts could be obtained (Fig. 1). We suggest that this behaviour is due to a decrease of the microvoids content in the film when Ts increases. On the other hand, we have also observed the dispersivity of D, a phenomenon that we are currently studying more extensively.

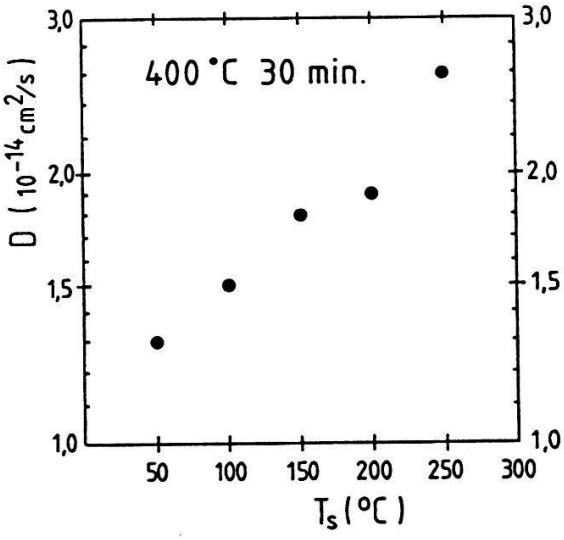

Fig. 1 : the hydrogen diffusion constant D in function of the film deposition temperature Ts.

4. Aknowledgment

We thank professor L. Schlapbach (Fribourg University) for providing the H-standards. This work has been supported by the SNFSR.

5. References

[1] W. Beyer, in "Tetrahedrally-Bonded Amorphous Semiconductors", D. Adler and H. Fritzscher, eds., Plenum Press, New-York (1985), p. 129.

[2] D. E. Carlson et al., Phys. Lett. 33 (1978) 81.

[3] R. A. Street et al., Phil. Mag. 56 (1987) 305.

[4] J. Kakalios et al., Phys. Rev. Lett. 59 (1987) 1037.

[5] H. Curtins et al., Elec. Lett. 23 (1987) 228.

[6] M. Favre et al., J. Non-Cryst. Sol. 97/98 (1987) 731.

A STUDY OF THE EFFECTS OF ANNEALING ON THIN FILMS OF Bi-(Pb)-Sr-Ca-Cu-O

D. Abukay, H. Nakano†, M. Suzuki††, G. Burri and L. Rinderer

Institut de Physique Expérimentale, Université de Lausanne
CH-1015 Lausanne, Switzerland
† On leave from Nagoya University, Nagoya 464-01, Japan
†† On leave from Saga University, Saga 840, Japan

Abstract : Thin films of Bi-(Pb)-Sr-Ca-Cu-O were prepared by rf magnetron sputtering from a single target onto MgO substrates with pure argon gas. An annealing processing, comprised of heating over a temperature range of 840-860°C for durations of several hours in air was applied. The temperature dependences of the electrical resistivities were carried out. The relations between annealing condition and High-T_c phase (80K and 110K) are discussed.

The discovery of superconducting Bi-Sr-Ca-Cu-O phase (BSCCO) with the critical temperature T_c values in the region of 110K [1,2] has stimulated great interest in the preparation of high quality, high T_c BSCCO films. The multiphase nature of this compound complicates forming single phase thin films with a T_c of 110K for which a growth mechanism is not yet cleaned out. In this report, we are presenting the results of our experiment on the effect of annealing on the resistivity of BSCCO-system.

The samples were prepared by rf magnetron sputtering method with a $Bi_2PbSr_2Ca_2Cu_4O_x$ target prepared by usual ceramic techniques. The sputtering power, gas and pressure are respectively 100W, pure Ar and 0.05mbar. MgO substrates with (100) face were used, but they were not heated during deposition. All the samples, as deposited, are found in amorphous phase. The samples were annealed at 840-860°C in air for various length of time. The ratio of increasing temperature is about 10°C/min and cooling ratio is much less than heating ratio because the samples were cooled down by simply opening the door of furnace. The resistivity of the samples were measured over the sections which are mechanically patterned bridges (length: ≈1.5mm, width: ≤0.5mm) by the 4-probe technique in a controlled closed-cycle refrigerator. Figure 1 shows the temperature T dependences of the electrical resistivities ρ after first annealing. One striking feature of the films heated above 840°C is that the appearance of needle-shaped regions

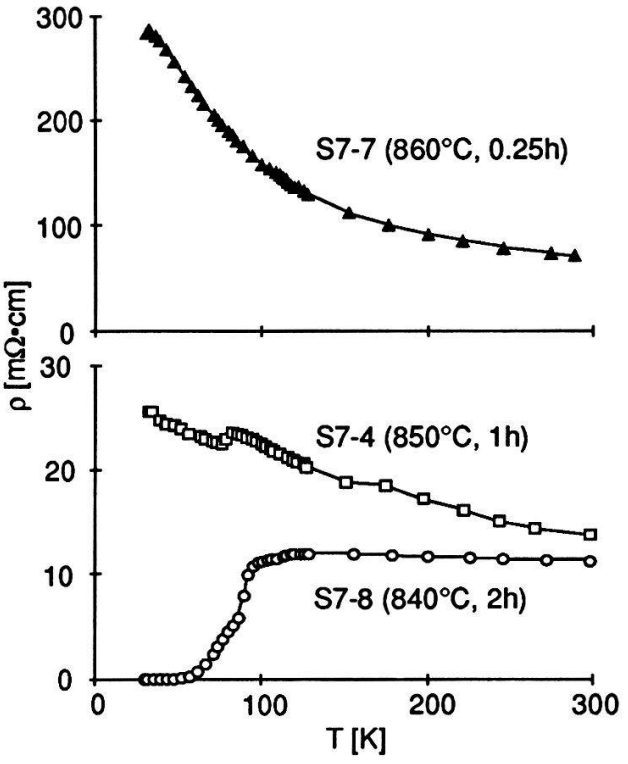

Fig.1 Temperature dependences of the electrical resistivities after the first annealing.

about hundreds of microns in length. The electron micro probe (EMP) analysis has shown that these region are Ca-rich insulating phase. When the number of these needles is high the resistance of the sample was measured as high. But we couldn't get sharp transition with only one annealing. After a second heating at 840°C for two hours in air, the samples with first annealing of 850-860°C become a rather good superconductor with sharp transition of 80K phase as shown in Fig.2. These results suggest that the superconducting phase is not stable above 840°C, but first annealing at temperature above 840°C is necessary to crystal growth. The EMP analysis has shown that there remained no lead in films after heat treatments like the other results [3]. We also measured ρ-T characteristics of the films sputtered with a $BiSrCaCu_2O_x$ target. For the films sputtered from targets without lead the grain sizes were much smaller and their surface morphology was less rough than the one prepared from the target with lead. This suggests that inclusion of lead might enhances the grain growth meanwhile it evaporates from the surface of film due to high heating temperatures. Another interesting observation was that the thinner films have higher proportions of 110K phase on the resistivity curves as shown in Fig.3. The first annealing conditions of samples S8-3 and S9-3 are respectively 850°C for 1 hour and 855°C for 20 minutes, and second annealing conditions of them are equally 840°C for 2 hours. This may imply that the high T_c phase is better stabilized in thinner layers than thicker ones which suggests that the kinetics of atoms is more favorable to occupy the right sites when the thickness of the film is thin enough.

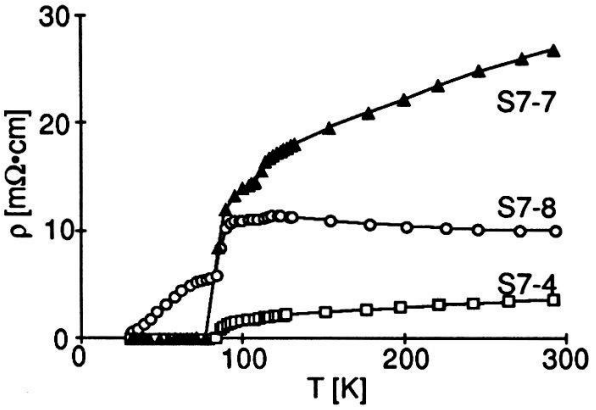

Fig.2 Temperature dependences of the electrical resistivities after the second annealing (840°C,2h).

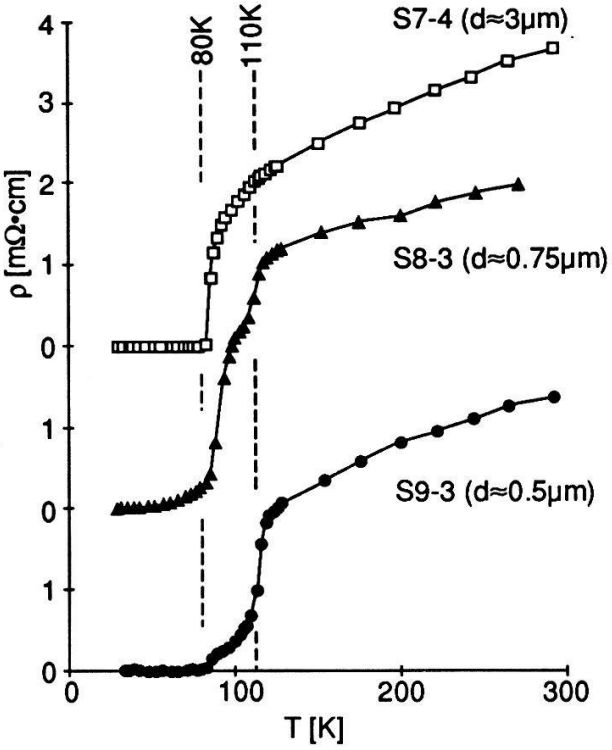

Fig.3 Temperature dependences of the electrical resistivities with various thickness *d*.

Acknowledgement

The authors are indebted to the Fonds National Swisse de la Recherche Scientifique.

References

[1] H. Maeda, Y. Tanaka, M. Fukutomi and T. Asano, Jpn. J. Appl. Phys. 27, L209 (1988).
[2] J. M. Tarascon, Y. LePage, P.Barboux, B. G. Bagley, L. H. Greene, W. R. McKinnon, G. W. Hull, M. Giroud and D. M. Hwang, Phys. Rev. B 37, 9382 (1988).
[3] Y. Kozono, T. Ohno, M. Kasai, M. Hanazono and Y. Sugita, Jpn. J. Appl. Phys. 28, L646 (1989).

AES, XPS and SIMS Characterization of $YBa_2Cu_3O_7$ Superconducting High Tc Thin Films

A. Gauzzi*, H.J. Mathieu*, J.H. James+ and B. Kellett+
Swiss Federal Institute of Technology, (EPFL),
*Materials Department, CH-1007,
+Physics Department,CH-1015,
Lausanne, Switzerland.

High Tc superconducting $YBa_2Cu_3O_{7-x}$(YBCO) films have been grown in-situ by ion beam sputter co-deposition using four Kaufman ion beam sources[1,2]. The deposition system [3] and film preparation techniques [4] have been described in detail elsewhere. Films were 100-200 nm thick and deposition rates were typically 3.5 $nmmin^{-1}$. As-deposited films have T_c (R=0) at 74 °K. Postannealing improved Tc (R=0) to 79 °K. The critical current density exceeded $5x10^4 Acm^{-2}$ at 77 °K. Films were deposited on $SrTiO_3$, or on Si with an intermediate layer of SiO_2 or Y_2O_3. Auger Electron Spectroscopy (AES), X-Ray Photoelectron Spectroscopy (XPS) and Secondary Ion Mass Spectroscopy (SIMS) were used to depth profile films deposited at 350°C and 650°C [5-7]. Data were transferred to an Apollo network station via a serial interface for data treatment using the *LOSAN* software package for AES, XPS and SIMS data evaluation [8] For quantification of XPS and AES analysis, standards of BaF_2, $BaCO_3$, BaO, BaO_2, CuO, Cu_2O and Y_2O_3, and monocrystals of $BaCuO_2$ and $YBa_2O_3O_{7-x}$ were measured. XPS binding energies and AES sensitivity factors were determined. Results indicate that the BaO and Cu_2O powders were partially oxidized to BaO_2 and CuO. For YBCO, two separate peaks for copper, barium and oxygen corresponding to two different electronic valence states were found. Using XPS Wagner area sensitivity factors [9], quantitative results of the surface composition (at %) were obtained. New AES sensitivity factors differing from handbook factors have been established. Carbon contamination was observed at the surface, but in the YBCO films carbon concentration was below the AES detection limit of < 1 at% of a monolayer. After calibration with a 30 nm thick anodic Ta_2O_5/Ta standard, AES concentration depth profiles of thin YBaCuO films deposited on $SrTiO_3$ and Si, respectively,were compared with SIMS profiles indicating increased SIMS sensitivity compared with AES. Static SIMS data of the monocrystal [10] and thin film spectra of the first 1-2 monolayers showed almost identical cracking patterns.

Conclusions

1. Superconducting YBCO thin films grown in-situ on $SrTiO_3$ and Si by four ion beam co-deposition have been characterized by AES, XPS and SIMS analysis. Although a $BaCO_3$ sputter target was used, carbon contamination in the film is below AES detection limit of < 1 at% of a monolayer.

2. AES sensitivity factors for these films have been proposed based on a monocrystalline reference sample allowing one to quantify depth profiles.

3. Two different XPS binding states have been found for copper, barium and oxygen in both YBCO films and monocrystals.

4. SIMS data give qualitative complimentary information to AES within the films with higher sensitivity. There is very good agreement between static SIMS data of the monocrystal refe

References

1. D. Pavuna, W. Baer, H. Berger, H.J. Mathieu, A. Vogel, M. Schmid, V. Gasparov, M. Affronte, F. Vasey and F.K. Reinhart; Physica C, **153-155**, pp 1449, (1988).

2. D. Pavuna and J.H. James; in "*High Temperature Superconductors*" Published by Tata Energy Research Institute (New Dehli), Ed R.K. Pachauri, (1989), in-press.

3. S. Michel, J.H. James, B. Dwir, M. Affronte, B. Kellett and D. Pavuna; J. Less Common Metals, **151**, pp. 419-427 (1989).

4. J.H. James, B.J. Kellett, A. Gauzzi, B. Dwir and D. Pavuna; , E-MRS Conf., Strasbourg, 1989. To appear in Journal of Applied Surface Science (1989), in press.

5. M.P. Seah and C.P. Hunt; Surf. Interface Analysis **5**, 33 (1983).

6. M.P. Seah, H.J. Mathieu and C.P. Hunt; Surf. Sci. **139**, 549 (1984).

7. H.J. Mathieu and D. Landolt; Surf. Interface Analysis **11**, 88 (1988).

8. H.J. Mathieu, S. Mischler, A. Vogel, A. Seiler and G. Riedl; Surf. Interface Analysis, **12**, 78 (1988).

9. C.D. Wagner, W.M. Riggs, L.E. Davies, J.F. Moulder and G.E. Muilenberg (eds.); *Handbook of X-Ray Photoelectron Spectroscopy*, Perkin Elmer Corp., Edina, Minn., (1979).

10. F. Licci, MASPEC, C.N.R., Parma, Italy

DYNAMICS OF FLUX PENETRATION IN SUPERCONDUCTING Y-Ba-Cu-O HOLLOW CYLINDERS

E. HOLGUIN and H. BERGER
Institut de Physique appliquée, Ecole Polytechnique Fédérale, CH–1015 Lausanne
J.-F. LOUDE
Institut de Physique nucléaire, Université de Lausanne, CH–1015 Lausanne

Abstract

We present experiments carried out in hollow cylindrical samples of YBaCuO cooled at 77 K. An external coil generates a pulsed field in an annular portion of the sample. A concentric inner coil measures the magnetic flux in the hole. For H larger than H_{shield}, we observe a flux reaching the central hole after a small time delay and then rising slowly to its maximum value.

1. Introduction

The dynamics of destruction of superconductivity by an overcritical magnetic field was initially studied by Pippard [1] in type-I superconductors. According to this author, the transition from the superconducting (S) to the normal (N) state is controlled by electromagnetic damping; the magnetic field takes a value equal to H_c at the S-N frontier. In type-II superconductors, the phenomena are complicated by the Abrikosov lattice.

We present preliminary results of the dynamics of destruction of superconductivity by a magnetic field in high-temperature superconductor samples.

2. Experimental procedure and results

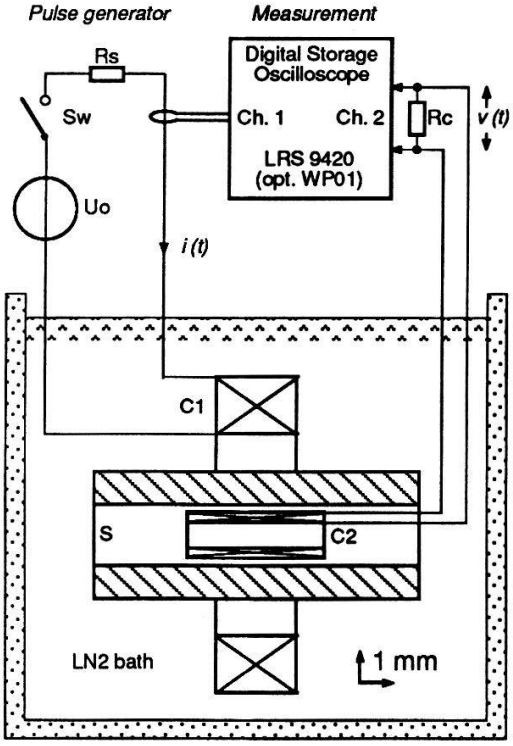

Figure 1. Experimental setup.

An external field coil (C1) generates a pulsed magnetic field in an annular portion of the sample (S) cooled at 77 K. A concentric inner coil (C2) of 500 turns measures the rate of variation of the magnetic field in the hole.

The sample (S) is made from sintered YBaCuO bulk material, mechanically machined to its final tubular form (8–10 mm length, 4 mm outer diameter, 2 mm hole diameter).

We record the current $i(t)$ through the field coil and the voltage $v(t)$ delivered by the inner measuring coil, critically damped by resistor Rc.

The experiments were carried out in "single-shot" mode on samples cooled in zero-field, to avoid the disturbing effect of trapped fields.

For $H < H_{sh}$, $v(t) = 0$; the sample acts as a perfect magnetic shield. H_{sh} depends on the sample composition, preparation and history; we had $H_{sh} \approx 1600$ A/m (about 2 mT in vacuum).

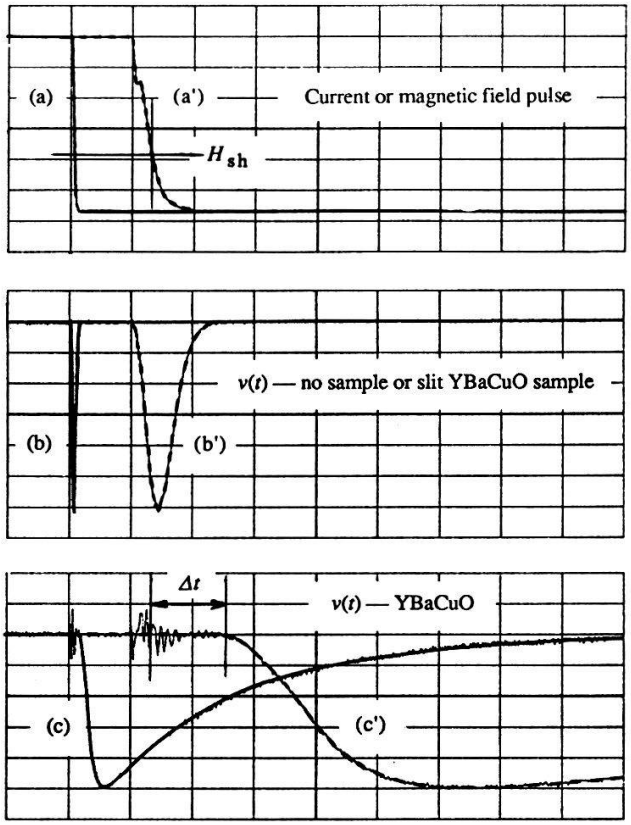

Figure 2. Samples of the recorded current and voltage waveforms. Time scale 5 μs/div. (solid line) and 0.5 μs/div. (dashed line; note the shifted time origin).
(a) and (a'): current pulse $i(t)$. $H(t) \propto i(t)$
(b) and (b'): electronic response, *i.e.* voltage pulse $v(t)$ with sample removed.
(c) and (c'): YBaCuO sample; $v(t)$ for $H > H_{sh}$, measured at $H/H_{sh} = 1.5$.

The magnetic field penetrates into the sample and reaches the hole after a time delay Δt of the order of 1 μs (compare curves c' and a'). The velocity of propagation of the vortex lines deducted from this delay is of the order of 10^3 m/s; this velocity goes up with H.

After the delay, the magnetic flux in the hole (*i.e.* the integral of curve c) increases to reach eventually, after a few tens of microseconds, a constant value.

In order to find out whether the delay and slow flux penetration was due to intragrain or to intergrain currents, the experiment was repeated with an axially slit sample, thus eliminating the contribution of intergrain currents circulating around the sample. The magnitude and shape of the observed response are almost identical to the electronic response (curves b and b'); the magnitude is proportional to H; the shape and the absence of delay indicate an instantaneous flux penetration. There is thus no screening effect at all.

3. Conclusion

The critical field, the delay and the penetration time seem to be very sensitive to the sample composition and preparation mode; important ageing effects have been observed. More detailed investigations are in progress.

Acknowledgements

The authors wish to thank Dr. H. J. Bühlmann (EPFL/IMO) for his help and advice, especially in handling and mounting the measuring coils, Mr. J. Knœpfli for machining the samples, Prof. F. Lévy (EPFL/IPA) for his interest and support and the firm Sokymat SA, CH-1614 Granges, for graciously providing samples of the coils. This work was partially supported by the Swiss National Science Foundation.

References

[1] A. B. Pippard, Phil. Mag. 41, 243 (1950).

Tunneling Study of High T_c Bi-system film

M. Suzuki[†], D. Abukay, H. Nakano[††] and L. Rinderer
Institut de Physique Experimentale, Universite de Lausanne, CH-1015 Lausanne, Suisse
On leave from Saga University, Saga,[†] Japan and Nagoya University,[††] Nagoya, Japan.

Abstract: The Pb-SiO-High T_c Bi-system tunnel junctions were fabricated on the High T_c Bi-system film and the V-dI/dV characteristics were measured at 38 K and 300 K. The characteristic at 38 K gives 2Δ (energy gap) $\fallingdotseq$ 60 meV. The characteristic at 300 K suggests that O 2p band and hybridized band of O 2p and Cu 3d states exist near the Fermi level.

Now, it is a growing interest to elucidate a microscopic mechanism in High T_c superconducting state. The electronic state near the Fermi energy relates intimately to a mechanism of superconducting state. Recently the angle-resolved resonant photoemission spectroscopy has shown that the O 2p band and the hybridized band of O 2p and Cu 3d states are in the valence band near the Fermi energy, and holes in O 2p band play a key role in the high T_c mechanism [1].

The tunneling spectroscopy is also effective tool to obtain direct informations about the electronic state at superconducting state and a band structure near the Fermi energy in a normal state.

The high T_c film was formed on the (100) face of MgO single crystal by rf magnetron sputtering method with a $Bi_2PbSr_2Ca_2Cu_4Ox$ target, and then an annealing process was applied. The Pb-SiO-High T_c Bi-system junctions were fabricated on the High T_c Bi-system film with two phases of T_c=80 and 110 K by depositing SiO and then Pb, where the 80 K phase was dominant in volume. The V-dI/dV characteristics are shown in Fig. 1, where the lower curve is the characteristic at 4.3 K of junction fabricated on the High T_c ceramic Bi-system and the upper curve the one at 38 K of junction fabricated on High T_c Bi-film system. The former has clear structure at gap edge, but the latter has very weak structure. The resistance of the latter is too high (nearly 10 kΩ) to observe clear structure. The weak peaks in the latter, however, nearly coincide with those of the former. Therefore, it may be reasonably concluded that the weak peaks in the upper curve comes from a superconducting state. From the distance between two peaks, the energy gap 2Δ is estimated as nearly 60 meV.

As Harrison theoretically predicted, the V-dI/dV characteristic in a normal state is linear for the tunnel junction fabricated on the substance with a parabolic E-k dispersion relation [2]. The characteristic, however, deviates from a linear line at bias voltage, where a new band appears or where a band deviates from the parabolic E-k dispersion relation. In Fig. 2, a dashed curve is the V-d^2I/dV^2 characteristic at 300 K and a lower solid curve is the V -dI/dV characteristic at 300 K, where the negative polarity corresponds to the valence band of Bi-system. In Fig. 2, a sign of left hand side in a horizontal axis is negative for V-dI/dV and -d^2I/dV^2 characteristics and positive for the photoemission spectrum. The dashed curve reflects clearly a deviation from a linear line in the V-dI/dV characteristic. The upper solid curve in Fig. 2 is the angle-resolved resonant photoemission spectrum. The two peaks in the photoemission spectrum agree with the two peaks in the V-d^2I/dV^2 curve at the energies (0.2 and 0.55 eV) marked by A and B. By the angle-resolved resonant photoemission method, it has been found that the structures A and B come from the O 2p state and the hybridized state of O 2p and Cu 3d states, respectively.

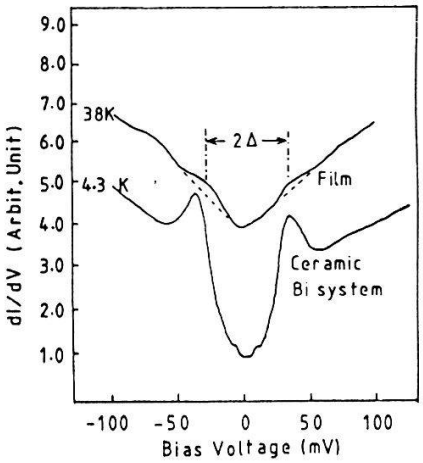

Fig. 1 The V-dI/dV characteristics for the junctions fabricated on High T_c Bi-system film and on High T_c Bi-system ceramic.

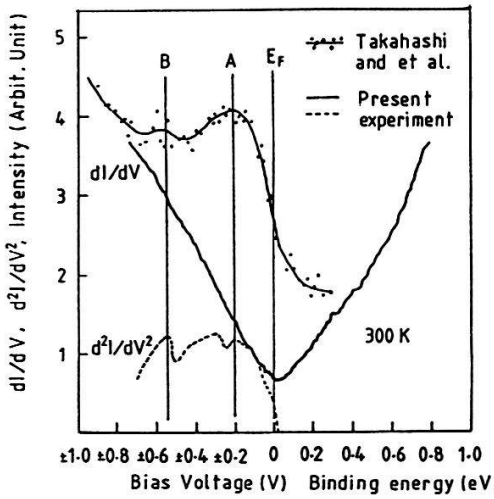

Fig. 2 Upper curve is the angle-resolved photoemission spectrum. Lower two curves are V-dI/dV and -d^2I/dV^2 spectra.

Acknowledgement: The authors are indebted to the Fonds National Suisse de la Recherche Scientifique.

References

[1] T. Takahashi and et al., Nature 39, 691(1988).

[2] W. A. Harrison, Phys. Rev. 123, 85(1961).

I-V CHARACTERISTICS IN Bi-(Pb)-Sr-Ca-Cu-O FILMS

H. Nakano†, M. Suzuki††, D. Abukay, S. Nicoud and L. Rinderer

Institut de Physique Expérimentale, Université de Lausanne
CH-1015 Lausanne, Switzerland
† On leave from Nagoya University, Nagoya 464-01, Japan
†† On leave from Saga University, Saga 840, Japan

Abstract : RF-radiation and magnetic field dependences of current-voltage (I-V) characteristics were measured on Bi-(Pb)-Sr-Ca-Cu-O superconducting lines. The samples were cut from the films which were prepared by rf-magnetron sputtering. The I-V characteristics show some structures under the rf-radiation (50GHz) and magnetic field (0-30Oe). Specially rf-radiation causes a peak in the V-dI/dV curves corresponding to Josephson effect. The results indicate that Josephson weak links exist in the boundary of the grains.

Weak link structures [1] and Josephson effect [2,3] in the grain boundary of High T_C superconducting polycrystal Y-Ba-Cu-O films have been studied. In this paper, we are presenting the observations of Josephson effects in Bi-(Pb)-Sr-Ca-Cu-O films under the rf-radiation and the magnetic field.

We would like to report mainly about a sample S7-8 which prepared by rf-magnetron sputtering on a MgO substrate with a $Bi_2PbSr_2Ca_2Cu_4O_x$ target and which was annealed three times (1st : 840°C,1hour, 2nd : 840°C, 1hour, 3rd : 870°C, 1hour and 840°C, 2hour). The thickness, length and width are respectively about 3μm, 1.72mm and 0.49mm. After 3rd annealing, the critical temperature T_C is about 70K and the electrical resistivity ρ is 33mΩ•cm at room temperature which large ρ value is due to insulating phases [4]. Such a film has rather large grain structure without lead [4]. Details of the fabrication procedures and structures will be reported in reference 4.

The electrical properties were measured by the four terminal method in a closed-cycle refrigerator, and rf-radiation supplied by a Gunn diode (about 50GHz) with attenuator. The I-V characteristics with or without rf-radiation and magnetic field are shown in Fig. 1. The structures like a excess current is observed in curve (a). This curve is a conventional one for weak link and is similar to the I-V characteristics of Y-Ba-Cu-O films [1]. The difference between curve (b) and (c) means that the rf-radiation effect is different from the effect of magnetic field. We also measured I-V characteristics with an oscillator of lower frequency (500MHz) and got similar results. Numerical differential calculus and average were done for the lower voltage parts of I-V characteristics. It

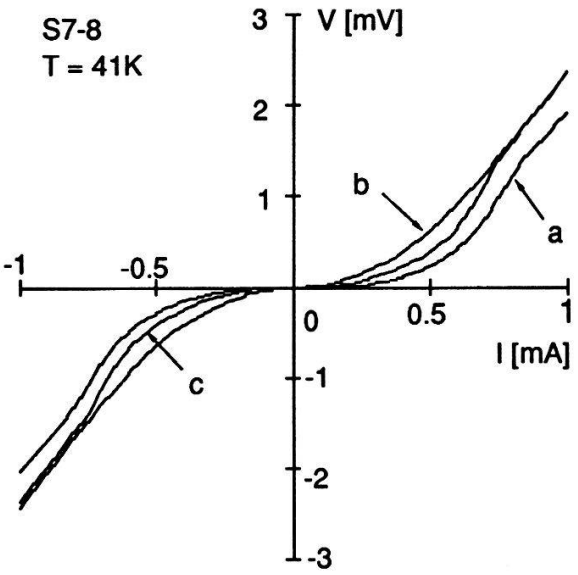

Fig.1 *I-V* characteristics of sample S7-8. (a) no rf-radiation and no magnetic field. (b) rf-radiation (50GHz). (c) magnetic field (33Oe).

gave us the *V-dI/dV* characteristics with various power of rf-radiation as shown in Fig. 2. The peak appears at about 100μV which corresponds to the first step of Shapiro steps for a single Josephson junction given by $hf/2e$ ($f \approx$ 50GHz). As increasing the rf-radiation power, the peak is increasing ,and then, decreasing. This phenomena is also corresponding to Shapiro step. This film might have a large number of Josephson weak link with series and parallel connections, but the step structure was slightly observed as like as Y-Ba-Cu-O films [3]. Figure 3 shows magnetic field dependence of voltage at various currents. There are some structures reappearably. It seems to be corresponding to the loop structures of Josephson weak links. Such effects of rf-radiation and magnetic field were observed below 60K and became clear at low temperature. One of the possibility, the junction type is Superconductor-Normal-Superconductor (SNS) junctions, because the normal coherence length of SNS junction increases as decreasing temperature. These results show the existence of Josephson Junctions made naturally in the grain boundary of Bi-(Pb)-Sr-Ca-Cu-O films.

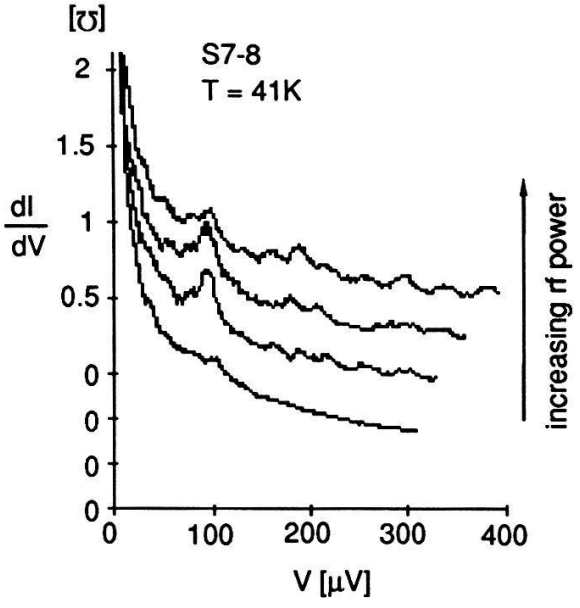

Fig.2 rf-radiation dependence of *V-dI/dV* characterristics.

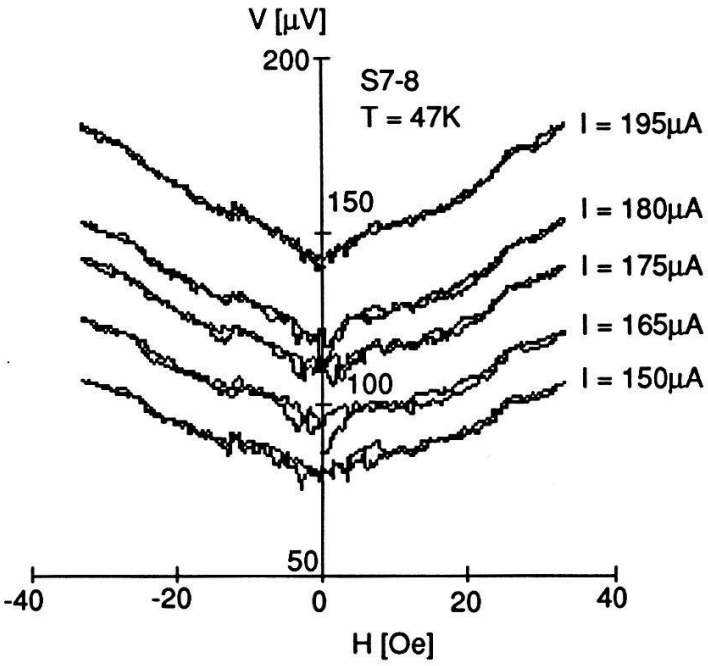

Fig.3 *V* vs. *H* at the various value of *I*.

Acknowledgement

The authors thanks Prof. Aomine and Mr. Soares for his valuable suggestions and encouragement. They are also indebted to the Fonds National Suisse de la Recherche Scientifique.

References

[1] M. Akinaga, D. Abukay and L. Riderer, Helv. Phys. Acta, 61, 861(1988).
[2] H. Tanabe, S. Kita, Y. Yoshizako, M. Tonouchi and T. Kobayashi, Jpn. J. Appl. Phys. 26, L1961, (1987).
[3] J. C. Gallop, W. J. Radcliffe, C. D. Langham, R. Sobolewski, W. Kula and P. Gierlowski, Suprercond. Sci. Technol. 2, 1, (1989)
[4] D. Abukay, H. Nakano, M. Suzuki and L. Rinderer, submitted to Helv. Phys. Acta.

SiO_2/TiO_2 QUARTER WAVE DIELECTRIC MIRRORS FOR VERTICAL CAVITY SURFACE EMITTING LASERS.

J.H. James, M.J. Proctor, C. Faure, W. Baer, and F.K. Reinhart. Institute of Micro and Optoelectronics, EPFL, Lausanne, CH-1015, Switzerland.

Abstract: We present SiO2 /TiO2 multilayer dielectric mirors for vertical cavity surface emitting MQW laser structures. Mirrors of up to 16 quarter wavelength ($\lambda/4$) layers have been deposited by ion beam sputtering. Reflectance (R%) and transmittance (T%) spectra over 1500-350nm are compared with simulations.

1. Introduction.

Sputtered films are suitable as dielectric mirrors for vertical cavity surface emitting laser structures as the arrival energy of sputtered atoms peaks at 1-2eV (compared with 0.1eV for evaporated atoms) enhancing film-substrate adhesion (1). Sputtered films also show improved densification and higher transmittance than evaporated films (2).

2. Film Deposition and Properties.

The deposition system, ($P_{base}=5x10^{-9}$mbar) consists of a 3cm Kaufman ion gun directed at one of four targets on a rotatable carousel (fig.1). Target materials are 10cm diameter disks of SiO_2,TiO_2, In_2O_3 (10 at% Sn) (ITO) and Cr. Deposition rates are measured by quartz crystal oscillator. Substrates follow a planetary motion for uniformity. To avoid charging effects SiO_2 is deposited with a neutralized Ar^+ beam (1000eV, 0.4 $mAcm^{-2}$), deposition rates are 0.30 $nmsec^{-1}$. TiO_2 and ITO are conducting and therefore deposited without neutralization under $5x10^{-4}$ mbar O_2, deposition rates are 0.03 and 0.15 $nmsec^{-1}$ respectively. The deposition time of a 16 layer mirror is about 8 hours.

The refractive index (n_f) and thickness uniformity of single layers are measured by ellipsometry at 633nm. Fabry Perot mode spacings are measured to determine n_f variation with λ. Fig. 2 is an SEM photo of a cleaved dielectric stack. Stacks with and without a base layer of ITO are deposited on glass, Si_3N_4 on GaAs and on GaAs. R% and T% are measured relative to evaporated Au or to Si wafers by dual beam spectrophotometry and compared with R% and T% measured using a Styril-9 dye laser at 890nm (emission wavelength of an MQW surface laser). Fig 3 shows R% of a fifteen layer stack+ITO deposited on Si_3N_4 on GaAs compared with an R% simulation of the same structure. The simulation program is described elsewhere (3). Agreement is not exact as one SiO_2 layer is of incorrect thickness. The measured R% of this structure is 99+-1%.

3. Acknowledgements.

We would like to thank D. Araujo and Dr. J.D. Ganiere for the SEM photos and Thomson CSF, Paris and the Swiss National Science Foundation for financial support.

4. References.

1. P.J. Martin, J. Mat. Sci., **21**, 1, (1986).

2. K.I. Chopra, "Thin Film Phenomena", McGraw-Hill, New York, (1969).

3. J.Faist, J.-D. Ganière, Ph. Buffat, S. Sampson and F.K. Reinhart, J. Appl. Phys., **66**, 1023, (1989).

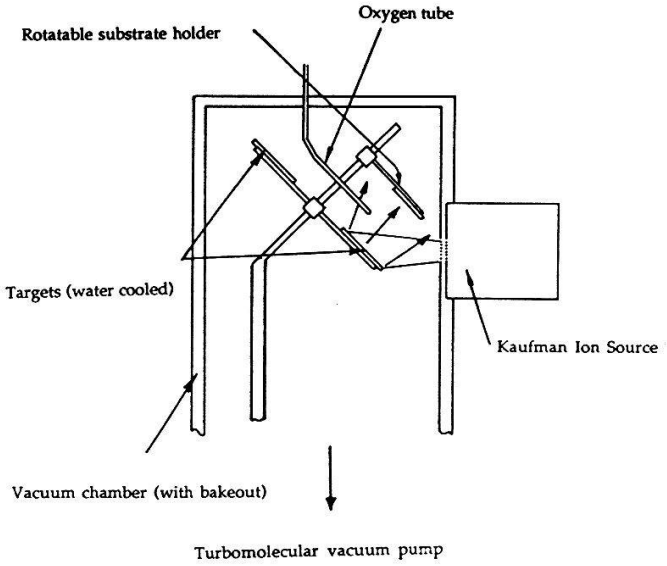

Fig. 1. The Deposition System.

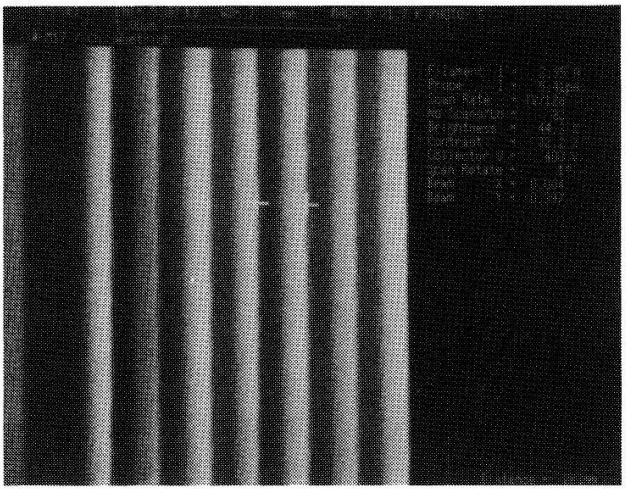

Fig. 2. SEM micrograph of a cleaved stack on Si_3N_4 on GaAs.

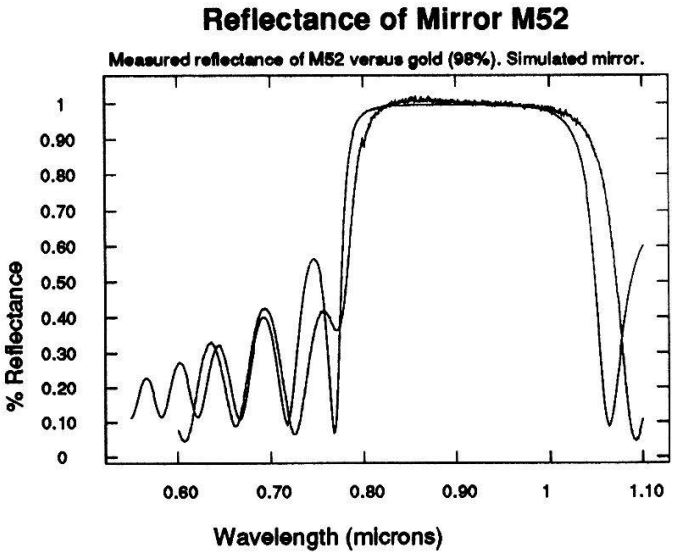

Fig. 3. R% vs λ of a fifteen layer stack, measured data and simulation.

INFLUENCE OF COOLING RATE ON THE SUPERCOOLING OF METALS WITH HIGH MELTING POINT

V. Soares, E. Meyer* and L. Rinderer
Institut de Physique Expérimentale, Université de Lausanne
CH-1015 Lausanne, Switzerland
*Instituto de Física, Universidade Federal do Rio de Janeiro
RJ-21945 Rio de Janeiro, Brazil

Abstract: Cooling curves of rapidly quenched liquid metal droplets with high melting point have been obtained by using a stereophotocalorimetric method, and liquid-solid phase transitions have been observed. We determined the cooling rate in the liquid state, the maximum supercooling produced, and the maximum temperature attained by the new solid phase. We have studied the influence of these cooling rates on the maximum supercooling of these droplets.

1. Introduction and Experimental Procedure.

In the liquid-solid phase transitions the interest stems particularly on the thermal instability of the supercooled liquid and how this instability determines the maximum supercooling attainable. The crystallization of the solid form is controlled essentialy by the nucleation rate of small crystallites in the supercooled liquid but the nucleus itself cannot be observed directly. The experimental information is then limited to the measurements of the temperature of the samples during all the process, and these results can contribute to decide if nucleation phenomena are either isothermal or adiabatic ones.(3)

The procedure described in (1) has been used to achieve and record large supercoolings on metal droplets with high melting point. A diagram of the apparatus is shown in Fig. 1. In brief, a metal wire is overloaded by a high current inside a chamber filled with He gas and the sample is liquefied. Radiating liquid metal droplets are then produced and ejected in the inner space of the chamber, being cooled during the time of flight. The image of this process is recorded on a photographic film. The cooling curve in the Fig. 2 was produced by using calibrated curves of color density ratio on photographic film vs. temperature, and position of free falling droplets vs. time.(1)

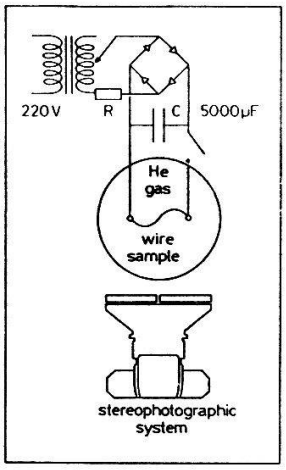

Fig. 1. Diagram showing the production of droplets.

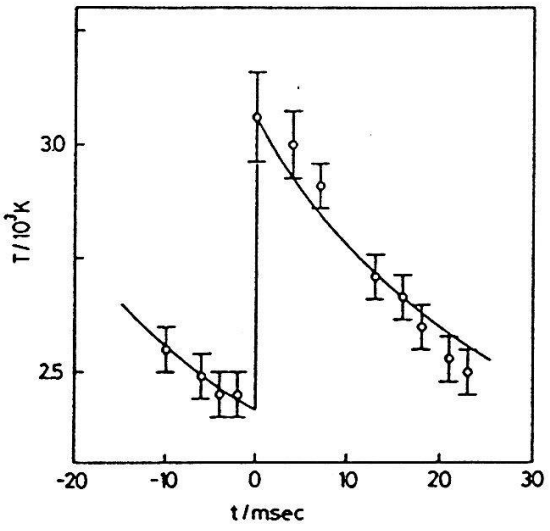

Fig. 2. Typical cooling curve to the droplets.

TABLE

No	Supercooling $\Delta T^-/T_M$	T^+/T_M	Cooling rate deg/sec
1	0.36	0.86	$4.0\ 10^4$
2	0.32	0.90	$2.6\ 10^4$
3	0.29	0.86	$2.1\ 10^4$
4	0.26	0.86	$1.5\ 10^4$
5	0.24	0.86	$7.7\ 10^3$

2. Results and Discussion.

From the cooling curves we have determined the cooling rate in the liquid state ($\Delta T/\Delta t$), the maximum supercooling $\Delta T/T_M$, and the temperature T^+/T_M corresponding to the temperature at which the crystallization ocurred.(1) To the calculation of $\Delta T/\Delta t$ we have fixed Δt=30msec and simply take the difference of temperatures at this interval of time. To the calculation of ΔT^- we have used $\Delta T^- = T_M - T_L$, where T_L is the limit temperature to the supercooling and T_M is the melting temperature.

The Table gives the values of supercooling achieved under identical cooling rates to different Ta droplets. We can observe that as the cooling rate increases so does the supercooling. However, different of Miroshnichenko and Bakharya's work, no similar relation was found to the temperature of the solid.

The present results are also not in agreement with the classical nucleation theory, where such behavior is not present.(1) The adiabatic nucleation theory seems to represent better the nucleation phenomena to these droplets since this theory predicts the solid phase must appear at temperatures higher than the temperature of the liquid but lower than the melting temperature, as is observed.

Acknowledgements: We thank the valuable support from the Fonds National de la Recherche Scientifique and Conselho Nacional de Desenvolvimento Científico e Tecnológico.

3. References:

(1) V. Soares et all, Helv. Phys. Acta, 62, 306 (1989)
(2) I. S. Miroshnichenko and G. P. Brekharya, Phys. Met. Metall., 29, 233 (1970)
(3) E. Meyer, J. Crystal Growth, 74, 425 (1986); 76, 525 (1986)

SINGLE CRYSTAL THIN FILM CdTe SOLAR CELLS

A.N. Tiwari, W. Floeder, S. Blunier, H. Zogg and H. Weibel
AFIF (Arbeitsgemeinschaft für industrielle Forschung) at Swiss Federal Institute of Technology, ETH-Hönggerberg, CH-8093 Zürich, Switzerland

Abstract
We fabricated in initial trials single crystal thin film CdTe solar cells. The epitaxial CdTe layers were grown on Si substrates using CaF_2-BaF_2 buffer layers. They were separated from the substrate by dissolving the BaF_2 layer. An Au/CdTe Schottky cell was achieved with about U_{oc}= 520mV, I_{sc}= 10mA/cm^2, FF = 0.4 and Eff. = 2%.

Introduction
CdTe is a promising semiconductor for photovoltaic applications, because of its near optimum band gap and its high absorption coefficient. Solar cells with monocrystalline bulk CdTe have achieved 15% efficiency [1]. For less material consumption, thin film solar cells with polycrystalline CdTe have been fabricated with 12.3% efficiency [2]. In this paper we describe a novel approach for making solar cells from single crystal CdTe thin films. The epitaxial CdTe films were grown on Si(111) using BaF_2-CaF_2 buffer layers to surmount the 19% lattice mismatch between CdTe and Si. The CdTe layer is removed from the Si substrate by dissolving the BaF_2 layer. The Si-wafer may be reused.

Experimental Procedure and Results
About 70Å CaF_2 (lattice mismatch to Si 0.6%) followed by 2000Å BaF_2 (lattice mismatch to Si 14%) are deposited onto a cleaned Si(111) wafer as a buffer layer using molecular beam epitaxy (MBE) [3]. In a separate MBE system 5-15µm CdTe (lattice mismatch to Si 19%) is then deposited on the BaF_2 layer at substrate temperatures of 300-400°C [4]. The CdTe layers are nearly free of thermal misfit strain because of some plasticity of the buffer layers. SEM, electron channeling and XRD show that the CdTe layers have good structural quality, comparable to CdTe layers grown on GaAs, InSb and sapphire.

In initial trials we fabricated Au/CdTe Schottky solar cells in the epitaxial CdTe layers. In a first step indium is deposited by vacuum evaporation on CdTe as a ohmic back contact (Fig. 1a). For support it is glued on a In-coated glass substrate. The CdTe layer is removed from the Si-substrate by dissolving the BaF_2 layer in water. In a further step gold as a window is evaporated on the removed CdTe layer (Fig. 1b). Electron microprobe analysis (EMPA) of the removed CdTe layers showed that there are no traces of Ba or F left after removal [5].

The I-V characteristic under illumination of such a Au/CdTe Schottky cell is shown in Fig. 2. Without applying any chemical and thermal treatment an open circuit voltage V_{oc}= 520mV, a short circuit current I_{sc}= 10.1mA/cm^2, a fill factor FF = 0.39 and an efficiency of 2.1% was achieved.
There is a considerable potential to improve the solar cell performance:
- The low fill factor originates from the high resistivity CdTe film. In a next step we will dope the CdTe layers using photoassisted MBE. In this technique the layer is illuminated with laser light while growing.
- Optimizing the thickness of the gold layer will increase I_{sc}
- An improved material quality will yield higher U_{oc}. In future we will use an improved MBE system equipped with reflection high energy electron diffraction (RHEED) which allows better control of the crystallinity of the growing layer.

- Etching the CdTe surface and heat treatment will also improve the solar cell.

Alloying CdTe with HgTe, ZnTe and MnTe allows tailoring the band gap thus giving more flexibility for engineering a variety of cell structures like homo- and heterojunction pn, pin or cascade cells.

In conclusion we have fabricated a single crystal thin film CdTe solar cell in a heteroepitaxial layer of CdTe on Si for the first time. The CdTe films were removed from the Si-substrate by dissolving the intermediate BaF_2 buffer layer.

References

[1] P.K. Raychaudhuri, J. Appl. Phys., 62, 3025, 1987
[2] S.P. Albright, Proc. Polycrystalline Thin Film Program Meeting, Lakewood 1989, 17
[3] S. Blunier, H. Zogg and H. Weibel, Mat. Res. Soc. Symp. Proc., 116, 425, 1988
[4] H. Zogg and S. Blunier, Mat. Res. Soc. Symp. Proc., 91, 375, 1987
[5] W. Floeder, A.N. Tiwari, S. Blunier, H. Zogg and H. Weibel, Proc. 9th EC Photovoltaic Solar Energy Conf., Freiburg 1989, 157

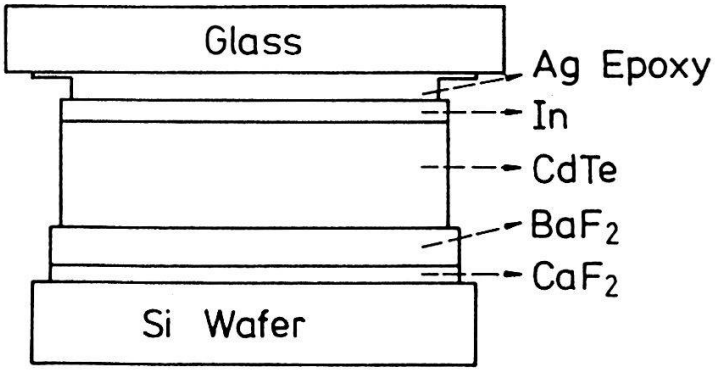

Fig. 1a: The structure used for separation of the Si wafer by dissolving the BaF_2 buffer layer.

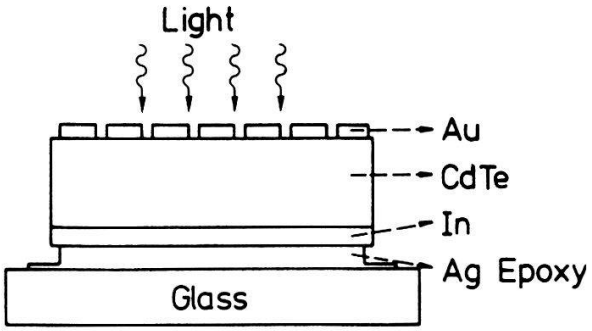

Fig. 1b: Cross section of the Au/CdTe Schottky diode.

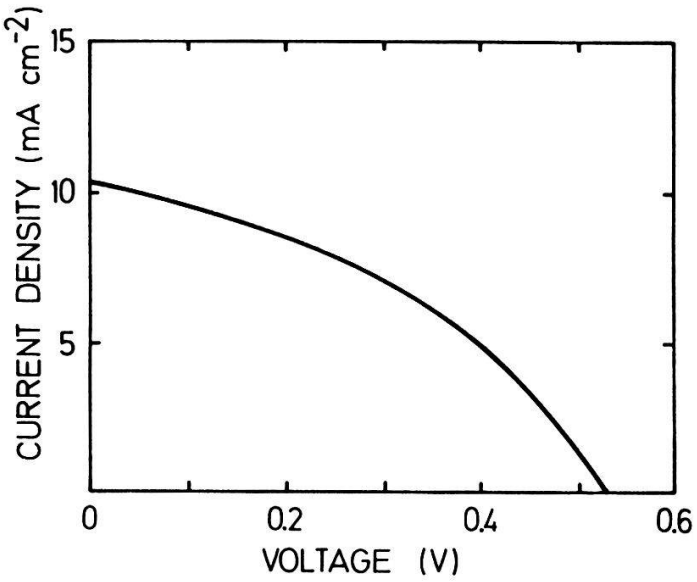

Fig. 2: Light I-V characteristic of a 2.1% efficiency Au/CdTe solar cell.

ETUDE DES RECOMBINAISONS RADIATIVES ET NON RADIATIVES DANS DES MULTIPUITS QUANTIQUES

D. Araujo, B. Zimmermann, J.-D. Ganière, F. K. Reinhart

Institut de Micro- et Optoélectronique, Département de Physique, EPFL, CH-1015 Lausanne

L'étude des centres de recombinaisons (électron-trou) radiatives et non-radiatives peut être faite dans un microscope électronique à balayage (SEM) par cathodoluminescence (CL) et par mesure de courant induit (EBIC).
Un système à flux continu d'hélium et une optique à miroir elliptique incorporés dans le microscope nous ont permis d'étudier les recombinaisons dans des multipuits quantiques (MQW) à des températures allant de l'ambiante à 5K. La structure consiste en 25 puits non dopés de GaAs (l_z= 95 Å) et 24 barrières d'$Al_{0.26}Ga_{0.76}As$ (l_b = 71 Å) insérés entre deux couches dopées p (Be:2x10^{17} cm^{-3}) et n (Si:2x10^{17} cm^{-3}) d'AlGaAs.
La résolution obtenue dans les multicouches est bien meilleure que la longueur de diffusion des paires e^--trou et nous laisse entrevoir de nouvelles études possibles sur les semiconducteurs. Les résultats sont interprétés qualitativement grâce à un modèle numérique du signal EBIC (1 et 2).

Sous un faisceau électronique d'un microscope à balayage (SEM), il y a création de paires é-trou dans le volume de la "poire" d'interaction des électrons et de l'échantillon. S'il existe dans ce volume un champ électrique, alors les paires électron-trou sont séparées et on mesure un courant électrique à travers l'échantillon (EBIC). En l'absence de champ électrique les paires restent spatialement proches et peuvent recombiner. Dans le cas d'une recombinaison radiative, une mesure de cathodoluminescence (CL) peut être faite. Ces deux méthodes sont donc complémentaires pour l'étude des recombinaisons. La cathodoluminescence nous informe sur la nature des recombinaisons et l'EBIC sur les champs électriques, donc sur la présence des recombinaisons. En cathodoluminescence deux modes de travail sont possibles. Le premier consiste en une collection de la luminescence, selective ou non en longueur d'onde, en balayant l'échantillon avec le faisceau électronique (mode image), une image des couches luminescente est ainsi obtenue. Le deuxième mode revient à tirer un spectre résolu en longueur d'onde de la luminescence de l'échantillon émise dans la poire d'interaction . Il est donc possible de mesurer la luminescence d'une couche semiconductrice crue par MBE d'une épaisseur de l'ordre de quelques dixièmes de micron en observant l'échantillon sur un plan clivé.

Les mesures EBIC sur cette diode p-i-n, ont mis en évidence le confinement des paires é-trou dans les puits par une baisse du signal EBIC à cet endroit. Les simulations numériques reproduisent bien l'effet du piègage des paires avec la tension d'accélération et l'intensité du faisceau électronique (1).
Les images de cathodoluminescence s'imposaient donc pour mettre en évidence une recombinaison radiative. Ce ne fut malheureusement pas le cas, car le pic à 788 nm, obtenu par une mesure de photoluminescence à basse température sur les puits, a une largeur extrêmement fine de 1.5 meV à mi-hauteur et ne permet l'émission que d'une faible intensité lumineuse par rapport à celle des deux couches p et n. Une image filtrée en longueur d'onde éviterait le contraste dû à la luminescence de la couche p et mettrait en évidence les recombinaisons radiatives des puits.
On peut également remarquer que la zone p luminesce nettement plus que la zone n pour une tension d'accélération du faisceau éléctronique de 10 KV ce qui correspond à une pénétration de 0,8 µm dans l'échantillon par conséquent les effets de surface ne sont pas négligables. Les mesures EBIC à différentes tensions nous ont permis d'évaluer le taux de recombinaisons non radiatives S au voisinage de la surface du plan clivé (équ. 2). La décroissance du signal dans les zone p et n est due à la diffusion des électrons et des trous jusqu'à la région du champ électrique. Cette décroissance est donc exponentielle et la longueur de diffusion peut être

mesurée sur les profils EBIC. Connaissant le coefficient de diffusion D des trous pour le côté p, et des électrons pour le côté n par l'équation d'Einstein (équ. 1), l'équation (2) permet d'évaluer S et le taux de recombinaisons non-radiatives dans le bulk sachant l'équation (3).

$$D = \mu\left(\frac{kT}{q}\right) \qquad (1)$$

μ = mobilité

$$\frac{D}{L^2} = \frac{1}{\tau} = \frac{1}{\tau_R} + \frac{1}{\tau_{NR}} + \frac{S}{d} \qquad (2)$$

d = distance à la surface

$$\tau_R = \frac{1}{B\,n} = \frac{1}{10E\text{-}10 \times 2 \times 10E\text{-}17} = 50\ ns \qquad (3)$$

B = coefficient de radiation

n = densité de porteurs

Les régressions linéaires de l'équation (2) permet d'estimer via les mesures EBIC les recombinaisons de surface S (pente), le temps de vie total τ et non-radiatif τ_{NR} par l'équ.3:

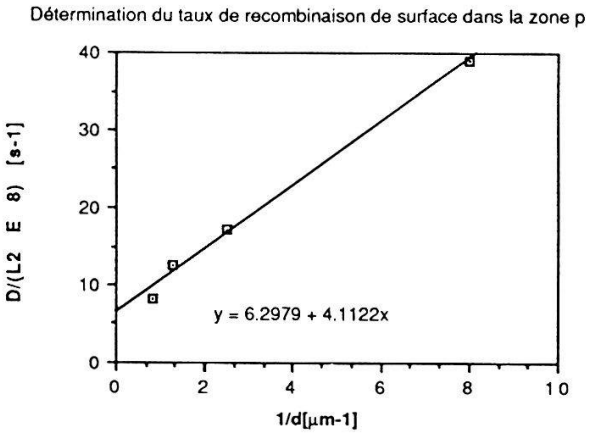

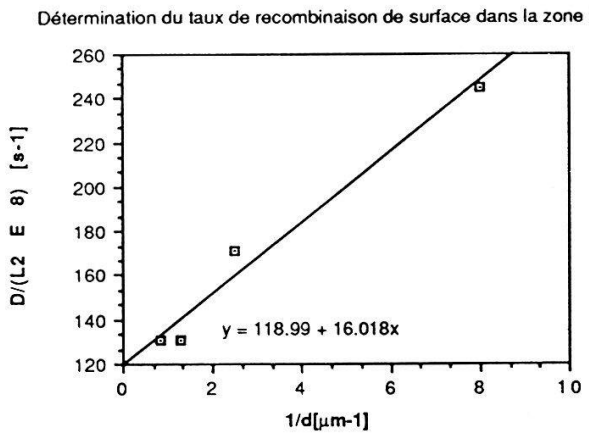

$\tau_{NR} \approx$ 2 ns
S_p = 4.1E4 cm/s

$\tau_{NR} \approx$ 0.1 ns
S_n = 16.0E4 cm/s

Les recombinaisons de surface sont beaucoup plus importantes et τ_{NR} de l'ordre de la 0.1ns du coté n et expliquent une luminescence plus de dix fois plus faible de cette couche.
En conclusion, nous avons pu expliquer les différentes intensités lumineuses émisent par des couches d'AlGaAs/GaAs grâce aux mesures de CL et aux mesures complémentaire d'EBIC et de photoluminescence de notre échantillon. La méthode s'avère donc puissante et appropriée pour l'étude de la nature des processus de recombinaisons. Des couches plus épaisses et des mesures à basse température (augmentant la mobilité) nous donneraient une meilleure précision.

Nous remercions G.Peter pour son compétent appui technique et le fond national suisse pour la recherche (num. 2.979-0.88) pour son soutien financier.

Références:

1) ARAUJO,D., et. al. Investigation by EBIC of p-i-n multiquantum well. *Optik* 83, suppl.4, 1989
2) MARTENS, H.W., HILDEBRAND, O. Computer simulation of electron beam induced current (EBIC) linescan across pn-junctions. *Scanning Electron Microscopy* 111, 1197-1209, 1983.
3) ZOOK, J.-D. Theory of beam-induced currents in semiconductors. *Appl. Phys. Lett.* 42(7), 602-604, 1983
4) JAKUBOWICZ, A. Theory of electron beam induced current and cathodoluminescence contrasts from structural defects of semiconductor crystals; steady-state and time-resolved problems. *Scanning Microscopy* 1(2), 515-533, 1987.

HYDROGEN PASSIVATION OF III-V SEMICONDUCTORS

L. PAVESI, D. MARTIN, F. MORIER-GENOUD AND F. K. REINHART

Institut de Micro et -Optoélectronique; Ecole Polytechnique Fédérale, CH-1015 Lausanne

ABSTRACT Hydrogen induced passivation of deep levels in direct gap $Al_xGa_{(1-x)}As$ is discussed by using a simple one-dimensional model for the rate equations.

INTRODUCTION The introduction of atomic hydrogen into semiconductors causes significant changes in both the electrical and optical properties of these materials [1]. Hydrogen reduces the active concentration of shallow donor and acceptor levels, as well as a variety of deep levels. Following exposure to a hydrogen plasma the low temperature photoluminescence (PL) spectra of $Al_xGa_{(1-x)}As$ samples grown by molecular beam epitaxy change. Direct gap $Al_xGa_{(1-x)}As$ shows a strong increase in the total PL intensity[2] whereas the PL spectra of indirect gap $Al_xGa_{(1-x)}As$ show an increase in the excitonic related recombinations[3].

EXPERIMENTAL DATA AND DISCUSSION In Fig. 1(a) we show the sketch of the structure of a sample formed by an epilayer of direct gap $Al_{0.32}Ga_{0.68}As$ 1.5 μm thick followed by 20 quantum wells (50 Å wide wells, and 200 Å wide barrier) and, finally 0.5 μm of $Al_{0.32}Ga_{0.68}As$ as buffer layer. The effect of hydrogen is to increase the PL intensity I from the different layers as given by the table (row labelled EXP). We note in particular that, after hydrogenation, the photoluminescence signal from the MQW increases more than that from the AlGaAs (see column 4).

Table I

	$\eta=I_{QW}/I_{AlGaAs}$	I_{QW}^H/I_{QW}	I_{AlGaAs}^H/I_{AlGaAs}	η^H/η
EXP	0.11	97	26	3.7
TH	0.11	78	21	3.8

To interpret these results, we have developed simple unidimensional rate equations for the AlGaAs density (see fig 1(b)) and the MQW density:

$$\frac{\partial n_{AlGaAs}}{\partial t} = -D\frac{\partial^2 n_{AlGaAs}}{\partial^2 x} - \frac{n_{AlGaAs}}{\tau_s}F_s(x) - \frac{n_{AlGaAs}}{\tau_{AlGaAs}}F_{AlGaAs}(x) - \frac{n_{AlGaAs}}{\tau_w}F_w(x) + G_0 e^{-\alpha x}$$

$$\frac{\partial n_{QW}}{\partial t} = \frac{n_{AlGaAs}}{\tau_w}F_w(x) - \frac{n_{QW}}{\tau_{QW}}$$

where the function $F_j(x)$ is different from zero if x belongs to the j-th layer (j=surface, AlGaAs or MQW) . τ_W is the trapping time into the MQW whereas τ_{QW} is the e-h lifetime in the MQW. The two equations have to be solved assuming CW excitation conditions and with the following boundary conditions

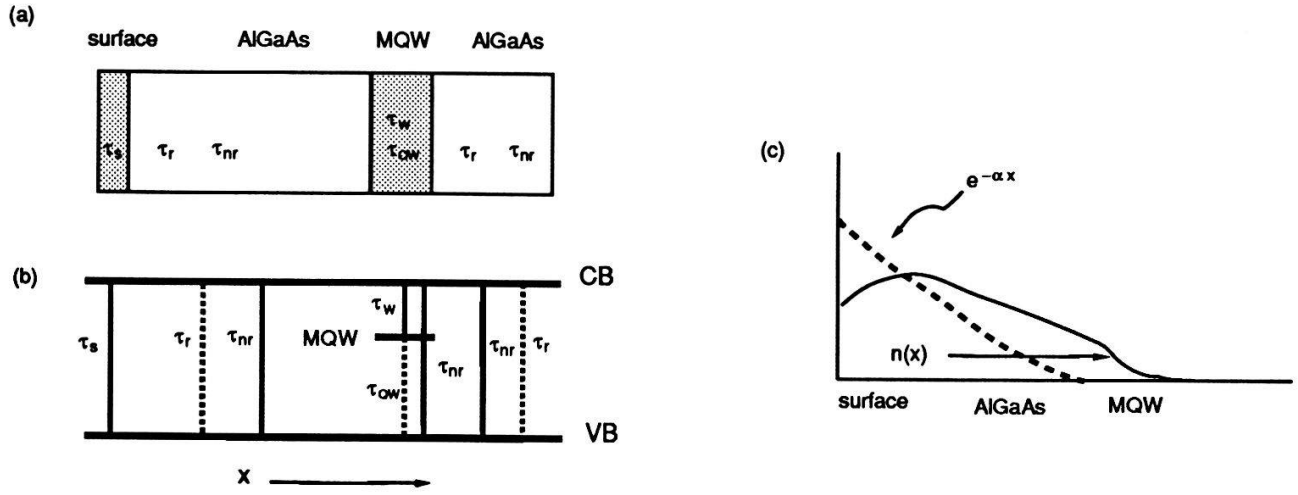

Fig. 1 (a) simplified sketch of the sample structure. (b) the recombinations taken into account by our model. (c) a schematic plot of the density distribution in the AlGaAs layer .

$$D \left.\frac{\partial n_{AlGaAs}}{\partial x}\right|_{x=0} = S\, n_{AlGaAs} \; ; \; n_{AlGaAs}(x \to \infty) = 0$$

A simplified picture of the solution is given in fig. 1(c). Table II gives the different parameters used to fit the experimental results for the PL intensities before and after the hydrogen treatment (see table I column TH). The surface thickness was 0.01 μm, and $\alpha = 2.2 \times 10^4$ cm^{-1}.

Table II

	τ_{nr} (10^{-9}sec)	τ_r(10^{-9}sec)	τ_W(10^{-9}sec)	τ_S(10^{-9}sec)	τ_{QW}(10^{-9}sec)	S (cm^2/sec)	D(cm^2/sec)
noH	0.01	0.4	0.001	0.01	0.2	40000	30
H	10	0.4	0.001	0.01	0.2	40000	30

The effect of hydrogen is thus to passivate deep levels which results in an increase of the non radiative lifetime.for the $Al_{0.32}Ga_{0.68}As$. This, in turn, allows a greater number of e-h pair to reach the MQW where they recombine radiatively. Let us note that no surface passivation is needed to fit the experimental data with our simple model.

In conclusion, defect passivation by hydrogen plasma exposure could be a powerful tool for post-growth improvements of the optical and electrical quality of the MBE samples.

REFERENCES

1 S. J. Pearton et al., Appl. Phys. **A, 43**, 153 (1987).

2 L. Pavesi et al., Appl. Phys. Lett., **54**, 1522 (1989).

3 L. Pavesi et al., Appl. Phys. Lett., **55**, 407 (1989).

HOLOGRAPHIC NM-LITHOGRAPHY AND GROWTH ON FINE GRATINGS BY MOLECULAR BEAM EPITAXY (MBE)

U. Marti[1], D. Martin[1], F. Morier-Genoud[1], B.Senior[2], F.K.Reinhart[1]
[1]Institut de Micro- et d'Optoélectronique, EPFL, 1015 Lausanne
[2]Institut Interdépartemental de Microscopie électronique, EPFL, 1015 Lausanne

1. ABSTRACT

Firstly we report on a method which is based on holographic photolithography for the fabrication of arrays of filament and dot like structures with a high density (period Λ=150nm). We achieved minimum feature sizes in the range of 30-40nm with an excellent uniformity over wide areas. Secondly we discuss regrowth experiments on GaAs substrates which were patterned with a fine line grating. We observed the formation of lateraly confined heterostructure filaments of about 20nm width.

2. INTRODUCTION

In recent years quantum well structures have made possible interesting developements in the field of semiconductor physics (quantized Hall effect, etc) and semiconductor devices (laser diodes, detectors, etc). The reduction of lateral dimensions leads to quantum wire and quantum box arrays that are expected to exhibit larger electroabsorption and electro-refraction, enhanced optical nonlinearities and higher differential optical gain compared to conventional structures[1]. A possible approach to the fabrication of such arrays is the combination of fine line lithography (ion beam, electron beam[2], optical holography) with monolayer crystal growth (MBE, etc). Holography with deep UV laser light (λ=257nm) seems to be very promising for the fabrication of large arrays of nm-structures with an acceptable variation in the feature size[3]. Recently, growth on a patterned substrate yielded some lateral control of crystaline properties[4].

3. FABRICATION OF NM-STRUCTURES

Very high contrast of the fringes is produced by the interference of two laser beams of nearly equal intensities. To take full advantage of this holographic process, we eliminate the substrate reflections with an absorbing antireflective coating. By varying the exposure, we control the feature size over a wide range independently of the periodicity. Moreover by choosing appropriate processing parameters, the photoresist profile can be tuned from nearly verical to overhanging (Fig 1).

A typical fabrication procedure is summerised as follows:

- spin coating of the substrate with:
  - antireflective coating (novolack or polyimide)
  - negative novolack photoresist
- Exposure and developement of the holographic resist pattern (Fig 1)
- Evaporation of Cr and lift off
- Transcription of the Cr pattern into the antireflective coating by O_2 reactive ion etching (RIE)

With this procedure small feature sizes of about 30-40nm with a density of Λ=150nm are achieved. The patterns of Fig 2 are obtained and are suited for subsequent dry etching into the substrate.

4. REGROWTH EXPERIMENTS

GaAs (100) substrates were patterned using the above method. About 120 nm deep grooves in the $[01\bar{1}]$ direction were etched by RIE as previously described[3]. The top of the mesas remained unetched. After removing the mask and degreasing, the samples were loaded into a MBE system. The epitaxial layers were grown at 630°C and consisted of (50nm/30nm) (GaAs/AlGaAs) buffer followed by 6 periods of (8nm/15nm) (GaAs/AlGaAs) supperlatice and 500nm AlGaAs. In the cross sectional scanning electron micrograph (Fig 3) the bright lines are AlGaAs layers with an Al composition of nominaly 30%. The first GaAs layer formed on the mesas facets which are near the (311)A planes. When the facets of neighbouring grating lines touch each other, the growth continued mainly in the [100] direction.Then lateral confined quantum well structures (quantum filaments) were formed and eventually a complete planarisation of the grating occurs. In this experiment, the buffer layer shows the pronounced faceting properies of MBE growth over small structures. In the superlatice growth, Ga adatom migration and the different sticking coefficients of the Ga and Al atoms for different crystal planes play an important role[4].

In another experiment we formed the V-grooves by thermal vacuum etching in a MBE system at 720°C just before growth at the same temperature. Similiar structures were formed as at 630°C, but with a more pronounced growth in the [100] direction.

In summary MBE growth on finely channeled substrates appears very attractive for the fabrication of quantum filaments with lateral dimensions smaller than 20nm. Further investigations are in progress.

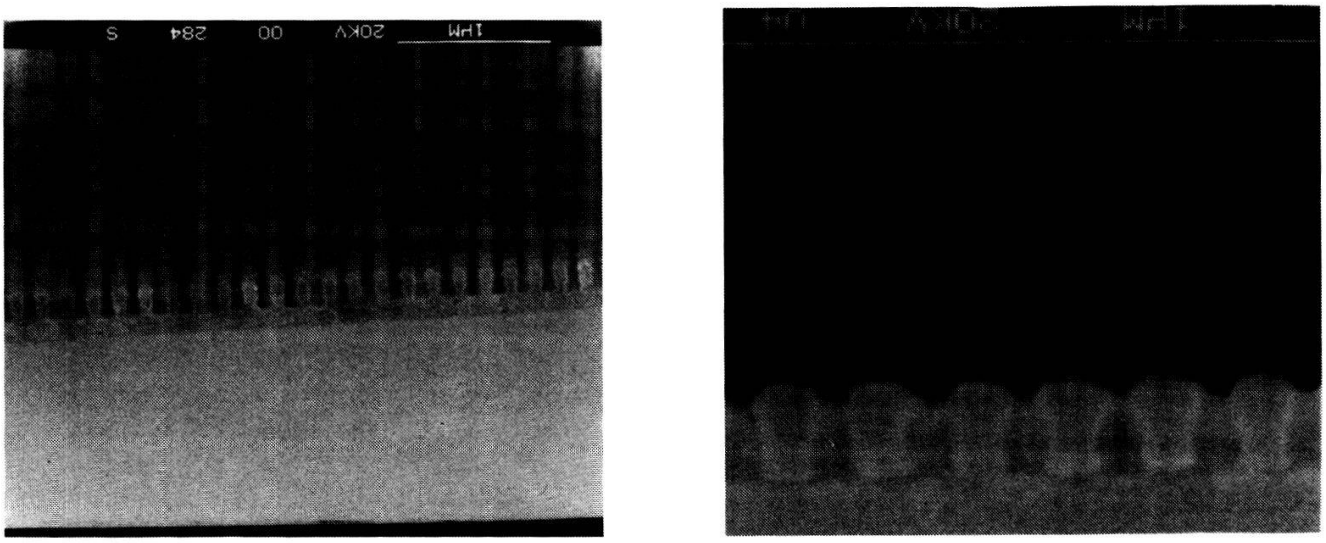

Fig 1: Developed photoresist profiles on antireflective coating.

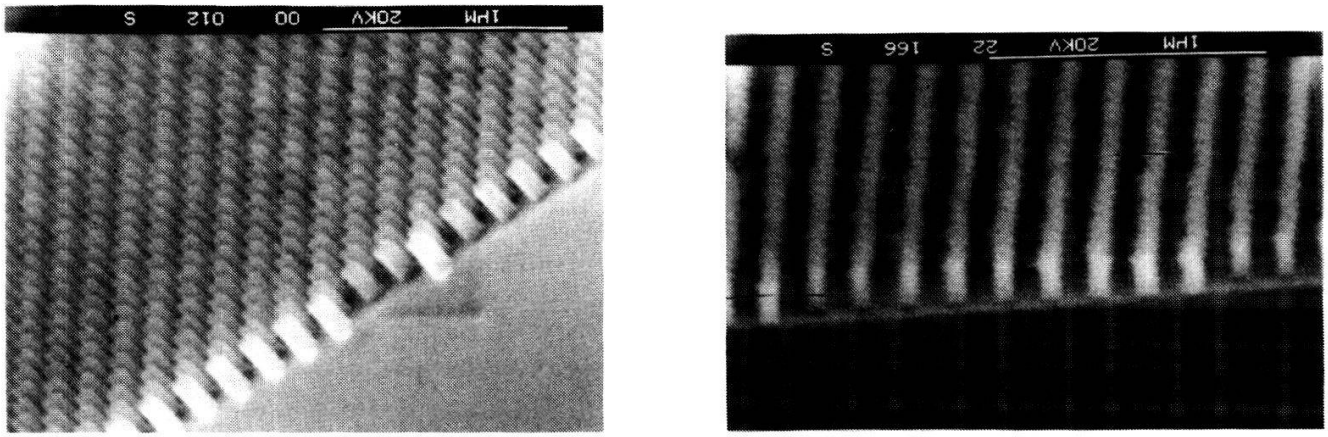

Fig 2: Final mask (patterned antireflective coating). Notice the high uniformity over wide areas.
(Dot like structures by the crossed grating method [3])

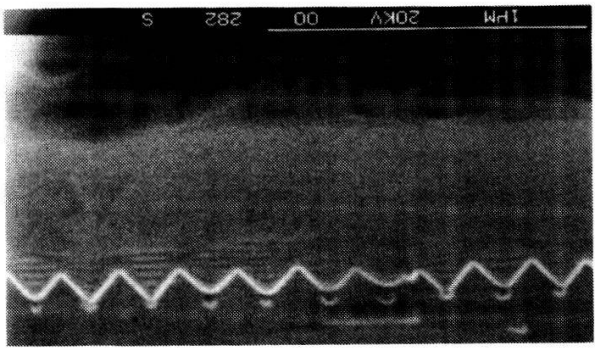

Fig 3: Scanning electron microcsope cross sectional micrograph of the discussed experiment.

This work was made possible through a collaboration with Thomson-CSF. We wish to thank M.Altmann for assistance in MBE growth.

[1]K.J. Vahala, J. Quant. Electron. QE-24, 523 (1988)
[2]F. Vasey, J.M. Stauffer, Y. Oppliger, F.K. Reinhart, Rapport de la réunion d'automne de la SSP 1989
[3]U. Marti, J.D. Ganière, W. Baer, F.K. Reinhart, H.P.A. 61, 122 (1988)
[4]S. Nilsson, E. Van Gieson, D.J. Arent, H.P. Meier, W. Walker, T.Forster, Appl.Phys.Lett. 55(10), 972 (1989)

Realization of Grating Couplers on $Al_xGa_{1-x}As$ Rib Waveguides using Electron Beam Lithography.

F. Vasey[1], J.M. Stauffer[2], Y. Oppliger[2], F.K. Reinhart[1]

[1] Institut de Micro- et Optoélectronique, EPFL, CH1015 Lausanne, Switzerland
[2] Centre Suisse d'Electronique et Microtechnique, CH2007 Neuchâtel, Switzerland

Abstract: We report the design, realization and characterization of optical grating couplers on $Al_{.15}Ga_{.85}As$ rib waveguides. We describe the direct electron beam lithography with automatic alignement used for all processing levels. Gratings with 300nm and 400nm periodicity are evaluated. We demonstrate reverse as well as forward light coupling on rib waveguide and slab waveguide structures at a wavelength of 1.15μm. The effective index of the corresponding TE and TM modes is measured and compared to theoretical predictions.

1. Introduction:

Gratings are key elements in optoelectronic circuits as they allow the realization of many devices such as couplers, filters or mirrors [1] in a planar technology, and can thus easily be integrated with other elements on a single substrate. They are however not totally compatible with standard manufacturing techniques, such as used in today's IC production plants, since their pitch (in the order of 0.1 to 0.4μm) is difficult to reproduce with conventional photolithography techniques. Alternative ways to achieve so small dimensions include holography [2] and direct write techniques [3,4].
We report in sections 2 and 3 the realization of optical diffraction gratings on rib waveguides, using electron beam direct write techniques for all processing levels. The coupling characteristics of these gratings are described in section 4 and allow us to evaluate quite precisely the waveguide parameters.

2. Design:

The device structure is shown on Fig 1. Along the vertical direction, the waveguide is asymmetric with a guiding layer (index n_g) of thickness t (or t+h) containing x% Al and two different cladding layers, one (index n_c) containing y% Al (y>x), and the other one being the surrounding medium (index n_0). Horizontally, light is confined by a symmetrical rib structure of width w. One can easily compute the mode effective index N_{eff} of such a rib waveguide by using the method described in [5].
The grating, which is much wider than the rib, has a length l, a depth a and a periodicity Λ. Its characteristics can be computed using the coupled wave theory [6], but we only want here to use simple geometric equations to roughly describe its coupler behavior [4]. The diffraction angles β (see Fig 1) of a wave (wavelength λ_0) hitting the surface of the grating at an angle α are given by:

$$\nu \cdot \lambda_0/\Lambda + sin\alpha = n \cdot sin\beta \;\; ; \;\; \nu = \pm 1, \pm 2, ...$$

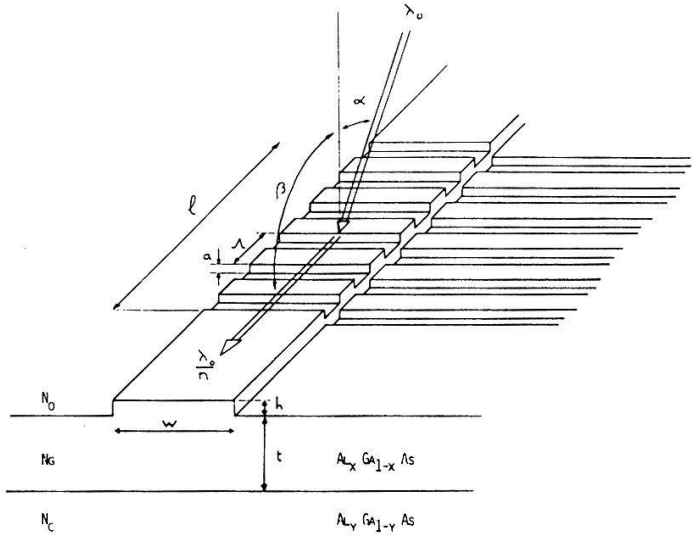

Fig 1. Grating Coupler Structure.
Left grating side ommited for clarity.

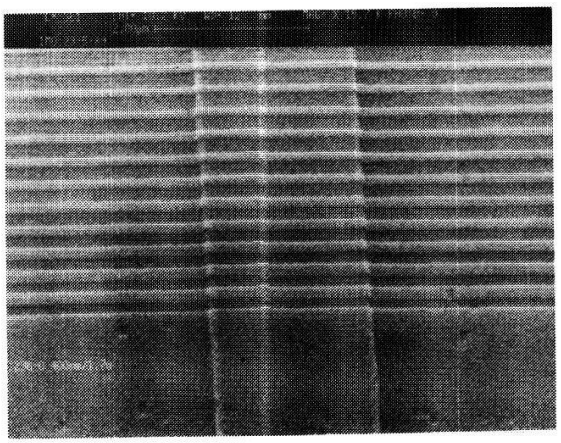

Fig 2. SEM View of a 400nm Pitch Grating on a 2μm wide Rib Waveguide.

A waveguide mode can be excited when $\beta = 90°$ and n=N_{eff}. Depending on the grating pitch Λ and the order of the grating ν, the coupling angle can be either positive (forward coupling) or negative (reverse coupling).
By looking at the orders diffracted into the air (n=1, $\beta < 90°$), the grating pitch can be measured with an accuracy of the order of one $\AA$.

3. Processing: The planar AlGaAs layers were grown by Molecular Beam Epitaxy on a n doped GaAs substrate.
The electron beam patterning with a Philips EBPG machine was done on positive (PMMA) or negative (Shipley SAL600) e-beam resists (single layered), using gold alignement markers to respect the orientation of the mask level being written with respect to previous ones.
The transfer of the structures from the resist to the substrate was achieved using Freon 12 : Argon Reactive Ion Etching. A processed grating is shown on Fig. 2.

4. Characterization: Four gratings on waveguides of different widths were evaluated. Their respective pitches were measured using UV (257nm) or red (633nm) wavelengths. The coupling was then attempted using a IR HeNe laser ($\lambda_0 = 1.15\mu$m) as a light source, and looking at the cleaved outputs of the waveguides with a CCD camera through a 40× microscope objective. As the gratings were much wider than the ribs, two distinct coupling angles could be measured, one for the coupling into the rib waveguide, the other one for the coupling into the 2-dimensional slab waveguide, on both sides of the rib. Furthermore, TE and TM modes could be discriminated when the available output power was sufficient.
The results (pitch Λ, coupling angle α and deduced effective index N_{eff}) for TE and TM modes are summarized in the following table, $\lambda_0 = 1.152\mu$m, $\beta = 90°$:

Λ[nm]	w[μm]	α; N_{eff} for TE_{rib}	α; N_{eff} for TE_{slab}	α; N_{eff} for TM_{rib}	α; N_{eff} for TM_{slab}
299.51	1.0	—31.65°;3.3226	—31.68°;3.3221	—31.90°; 3.3188	————————
299.52	2.5	—31.57°;3.3237	—31.62°;3.3229	—31.83°; 3.3197	————————
399.75	1.7	+25.90°;3.3194	+25.83°;3.3183	+25.65°; 3.3154	+25.63°;3.3152
400.00	3.6	+25.88°;3.3173	+25.80°;3.3160	+25.72°; 3.3147	+25.63°;3.3134

The grating parameters were: $a = 500\AA, l = 800\mu m$
and the waveguide parameters:$t = 0.6\mu m(SEM), x = 13.2\%(Photolum.), y = 22.4\%(Photolum.), h = 300\AA$

A numerical simulation including all four gratings and taking as inputs only the $N_{eff_{slab}}$ measured values for TE and TM modes gave the following results: $t_{sim} = 0.55\mu$m, $x_{sim} = 14\%, y_{sim} = 25.7\%$.

5. Discussion and conclusions: We first note that the grating periodicities achieved with the direct write apparatus were allways within 5Åof the specified values. The coupling characteristics show little difference ΔN_{eff} between slab and rib modes. This is due to weak confinement characteristics of the guide (small rib height h). The wider the guide (w), the bigger this difference. The slab N_{eff} values are not constant due to inhomogenities in the waveguide parameters over the distance separating each grating (in the order of a few mm). Comparisons between computer fitting results and measurements show good agreement for waveguide film thickness t and core Al content x.

This work was supported by the Swiss National Science Fondation.

References:

[1] W.Chang, IEEE MTT21 No12, Dec 1973, pp775-785
[2] U.Marti, Rapport de la réunion d'automne de la SSP 1987
[3] IBM Journal of Res and Dev Vol 32 No4, July 1988, pp439-579
[4] T.Suhara, IEEE QE22 No6, June 1986, pp845-867
[5] R.Knox, Proc Symp Submillimeter Waves Ser20, 1970, pp497-516
[6] H.Kogelnik, Bell Syst Techn J Vol48, Nov 1969, pp2909-2947

COLLISIONS OF HEAVY IONS WITH CARBON FOILS: EQUILIBRIUM CHARGE STATES AT ENERGIES FROM 0.5 TO 2 keV/amu

Michael Oetliker and Alfred Bürgi
Physikalisches Institut, University of Bern, Bern, Switzerland

Abstract: An experiment for measuring the distribution of emergent charge states, angular scattering, and energy loss for heavy ions passing through thin carbon foils at energies of 0.5 to a few keV/nucleon is described.

1. Introduction

Most studies of the passage of ions through solids have been done with ions of energies from several keV per nucleon to Mev per nucleon, see for example references 1, 2, and 3. There are almost no data at energies of 0.5 to 5 keV per nucleon. This is a particularly interesting energy regime because it corresponds to ion velocities comparable to the velocities of valence electrons. Moreover, at these energies the dominant energy loss mechanism is collisions with the electrons in the solid, while the dominant scattering mechanism is collisions with the atomic cores of the solid. In addition, knowledge of transmission coefficients and energy loss are important in the design of spacecraft borne time of flight (TOF) ion mass spectrometers that use thin carbon foils to convert the highly charged incident ions of the interplanetary medium to neutral and singly ionized species (4). We have measured the charge state distributions, angular scattering, and energy loss for a number of heavy ions through carbon foils as a function of incident ion energy and foil thickness.

2. Description of the Experiment:

An incoming ion beam passes through a small entrance aperture of area $1mm^2$ and strikes a carbon foil. The scattered beam is then collimated through a thin slit, electrostatically deflected by a pair of parallel plates, and finally strikes a position sensitive detector. On this detector, one coordinate is related to the scattering angle, whereas the deflection in the other direction is proportional to qU/E (q: charge, U: deflection voltage, E: particle energy). The image on the detector is a series of parallel bands corresponding to the various charge states.

By summing the number of particles in each band, the yields for the various charge states can be obtained, as well as the energies after the collision, which are calculated from the displacement of the bands.

3. Results

We have used incoming ion beams of He, C, N, O, ^{20}Ne, ^{22}Ne and Ar, mostly singly ionized, but in some cases also doubly ionized, with energies 0.5 to 2 keV/amu. The yield for charge state +1 is a strong function of the residual energy per nucleon and becomes very small at low energies. At 1 keV/amu it is typically a few percent. Multiply charged and negatively charged (O and C) ions occur. Results for ^{20}Ne are shown in Fig. 1. Elements of the same period have similar +1-yields. The angular distribution is a Lorentzian for higher energies and a Gaussian for lower energies with a half width at half maximum of typically 5-20°.

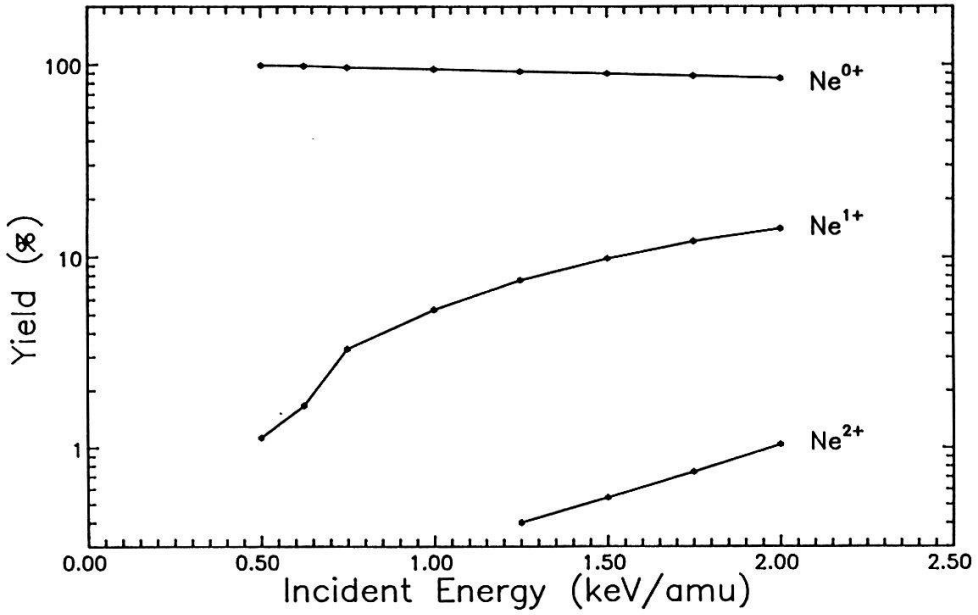

Figure 1: Equilibrium charge state distribution of ^{20}Ne.

4. References

[1] K. Shima et al., Atomic Data Nuclear Data Tables 34, 357 (1986).

[2] H.D. Betz, Rev. Mod. Phys. 44, 465 (1972).

[3] P. Hvelplund et al., Nuc. Instr. Meth., 90, 315 (1970).

[4] D. Hovestadt et al., ESA Special Publication, SP-1104 (1988).

Research supported by the Swiss National Science Foundation.

A SIMPLE LOCK-IN TECHNIQUE TO MEASURE NARROW VELOCITY DISTRIBUTIONS IN ATOMIC BEAMS

Olivier Carnal, Rudolf Grimm and Jürgen Mlynek
Institute of Quantum Electronics, ETH Zürich, CH-8093 Zürich

Abstract: We describe a lock-in technique for high resolution measurements of velocity distributions in atomic beams. The main advantages of this technique are a higher duty cycle and an improved signal-to-noise ratio, compared to classical time-of-flight (TOF) methods. We present both a brief theoretical description and first experimental results on a supersonic Argon beam.

In the last few years extremely narrow velocity distributions in atomic beams have been realized using supersonic expansions. These velocity distributions can be further compressed by means of laser light forces. For the measurement of such narrow velocity distributions simple and powerful techniques are needed. In this contribution we present a technique using a modulated atomic beam in combination with a phase sensitive detection. In this respect our work is related to previous work on gas-surface scattering where a similar approach is used [1].

The principle of the technique is schematically shown in figure 1a): the chopper CH imprints a modulation on the beam. This modulation fades out during the flight distance L due to different atomic velocities in the beam. The particle detector D probes the modulation after the flight distance L. The detector signal is passed through a narrow-band lock-in amplifier where only the fundamental component of the signal is amplified. Looking only at this fundamental frequency, the atomic density modulation at the chopper has the form: $n(t,z=0)= n_0 \sin(2\pi\nu t)$. After the flight distance L the form of the modulation is given by: $n(t, z=L) = n_0 [A_i(\nu) \sin(2\pi\nu t)+ A_q(\nu)\cos(2\pi\nu t)]$, where $A_i(\nu)$ and $A_q(\nu)$ denote the in-phase and quadrature components, respectively:

$$A_{i,q}(\nu)= \int_0^\infty N(\nu) \cos(2\pi\nu\frac{L}{v}+ \phi_{i,q})d\nu \ , \ \text{with} \ \phi_i= 0, \phi_q= \pi/2 \qquad (1)$$

The velocity distribution N(v) can be found by a simple inverse Fourier transform, provided A_i or A_q are known over a sufficiently wide range of modulation frequencies. In general this condition is not easy to fulfill.

Under supersonic beam conditions, however, A_i and A_q can be calculated analytically. Assuming a typical supersonic velocity distribution:

$$N(v) \sim v^3 \exp(- 4 \ln 2 (\frac{v-v_0}{\Delta v})^2) , \quad \Delta v/v_0 << 1 , \qquad (2)$$

with a narrow Gaussian shape (FWHM: Δv) around a mean velocity v_0 [2], we find, e.g., the

following frequency response of A_i:

$$A_i(\nu) \sim \cos\left(2\pi\nu\frac{L}{v_0}\right) \exp\left(-\frac{\pi^2}{4\ln 2}\left(\frac{\Delta v L}{v_0^2}\right)^2 \nu^2\right) . \qquad (3)$$

Here the frequency separation $\Delta\nu$ between two zeros of A_i yields the mean velocity v_0, and the Gaussian decrease in signal amplitude determines the speed ratio $v_0/\Delta v$.

Our experiments to demonstrate the technique were carried out with a supersonic beam of Argon atoms (flux $\phi \cong 10^{15}$ particles/sec). In our setup (fig. 1a)), the chopper consists of a rotating slotted disk driven by an asynchronous motor and the modulated beam is detected downstream by a fast Bayard-Alpert ionization gauge. The time constant of the lock-in was set to 100 msec and the flight path had a length of L= 0.89 m. Figure 1b) shows a typical measured in-phase lock-in signal (full line). Here the dotted line shows part of the fitted theoretical curve [see eq. (3)] (the rest is omitted due to the nearly perfect agreement with the experiment). From this curve, we extract the following experimental values: v_0= 570±10 m/sec, $v_0/\Delta v$= 14±1. These values are in agreement with results obtained by a classical TOF measurement.

We point out that the resolution in $v_0/\Delta v$ can be drastically improved using optical chop methods (only applicable to atoms with available optical transitions) where higher chop frequencies can be used.

[1] F. Goodman, H. Wachman, Dynamics of Gas-Surface Scattering, New York, Academic Press (1976) and references therein.

[2] J. B. Anderson, in 'Molecular Beams and Low Density Gasdynamics', vol. 4 (P. Wegener, ed.) ch.1, New York, Dekker Inc. (1974).

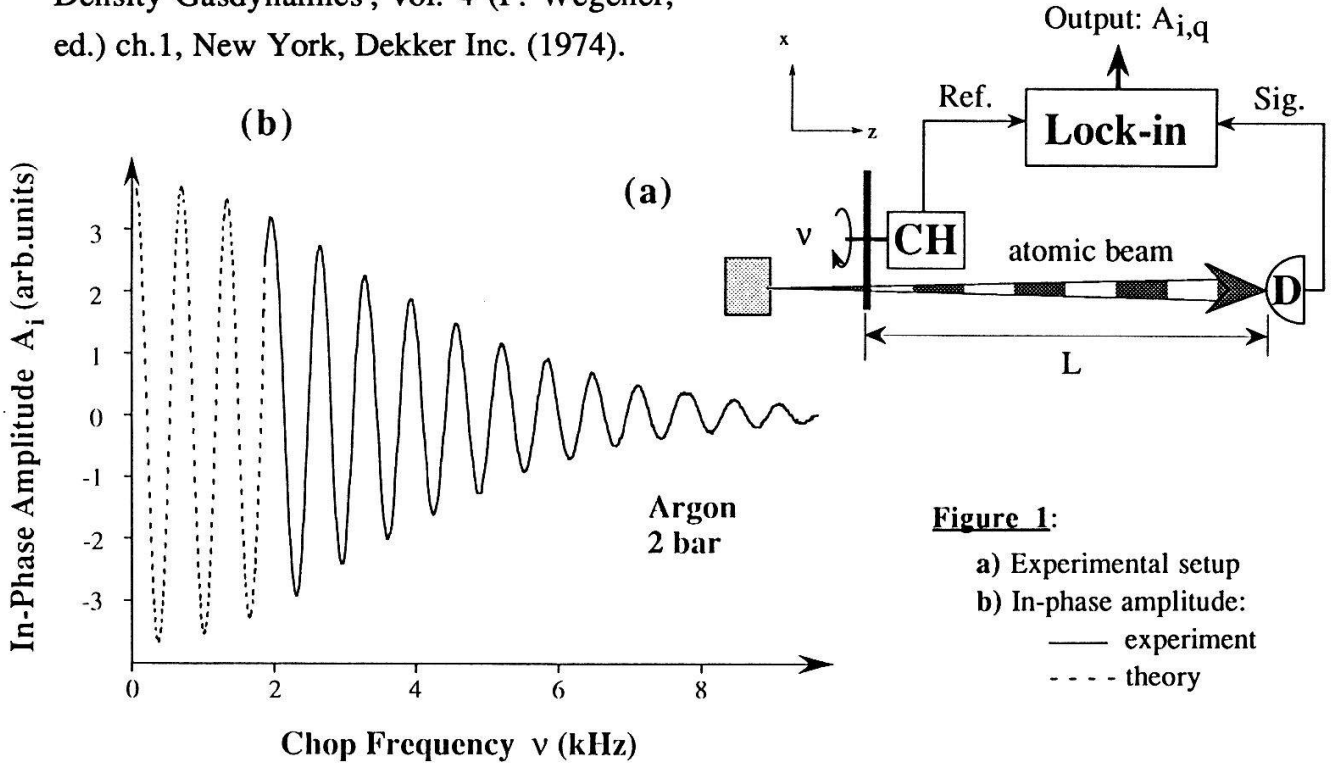

Figure 1:
a) Experimental setup
b) In-phase amplitude:
—— experiment
- - - - theory

Ein mathematisches Modell zur Lösung des Nullimpulsproblems bei Inkremental-Drehgebern

S.M.O.L. Schneider, B. Hübner F&E Abteilung, Baumer electric, Frauenfeld
L. Frey, Seminar für Angewandte Mathematik, ETH Zürich

Zusammenfassung

Die Berechnung der besten N-stelligen Kodierung eines Nullimpulses für Inkremental-Drehgeber ist ein *nichtlineares* Optimierungsproblem, dessen Lösung ca. $2^{N-3}N^2$ Operationen erfordert. Die vollständige Lösung des Problems durch Generieren und Absuchen sämtlicher möglicher Kodierungen ist deshalb ab ca. N=25 selbst mit Computern zu aufwendig.
In der vorliegenden Arbeit wird ein *einparametriges, statistisches Modell* vorgestellt, das die Berechnung von technisch brauchbaren Nullimpuls-Kodierungen auch für N>>25 erlaubt. Dazu wird eine Formel hergeleitet, welche es ermöglicht, den Modellparameter so zu wählen, dass mit "vernünftigem" Rechenaufwand eine gute Kodierung gefunden werden kann. Die numerischen Untersuchungen zeigen, dass die so bestimmte Kodierung der optimalen sehr nahe kommt.

Die physikalischen Grundlagen

Beim Einsatz von Inkremental-Drehgebern ist es nötig, dass der Sensor einmal pro Umdrehung einen Referenzimpuls erzeugt. Dieses Nullsignal wird dazu verwendet, den angeschlossenen Zähler auf Null zu setzen (z.B. beim Einschalten des Roboters) und erzeugt somit eine Referenz zur absoluten Positionierung. Es wird wie die Winkelpositionssignale durch Abtasten von Gittermustern auf der drehenden Scheibe erzeugt. Dabei wird ein Lichtstrahl von einer feststehenden Gitterblende abgetastet.

Die Vektordarstellung der Charakteristik

Die im folgenden vorgestellte Methode zur Optimierung und Auswertung des Nullimpulses beruht darauf, diesen als *binäre Zahl* darzustellen, und anschliessend mit sich selbst zu verknüpfen. Das Resultat dieser mathematischen Operation entspricht der *optischen Abtastung* des Nullimpulses und wird als dessen *Charakteristik* bezeichnet. Sie lässt sich direkt mit den Messungen am Drehgeber vergleichen, siehe Abb 1.

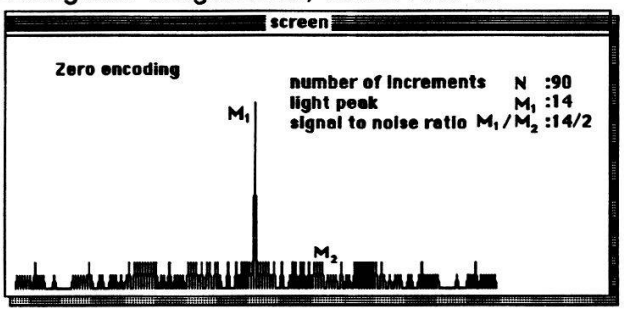

Abb. 1: *Die Charakteristik einer binären Kodierung mit N = 90*

Die binäre Kodierung auf Scheibe und Blende lässt sich mit den zwei Festlegungen $b_1=b_n=1$ und $b_i \in (0, 1)$ durch folgenden Vektor beschreiben: $\mathbf{b}:=(b_N, ..., b_1)$.
Das einzelne Element c_i zur Bestimmung der Charakteristik lässt sich so schreiben:

$$c_i = \sum_{K=1}^{M} b_K \cdot b_{N-M+K}, \qquad M \in \{1, ..., N\}.$$

Benützt man die folgenden Definitionen

$$M_1 := \sum_{i=1}^{N} b_i, \qquad M_2 := \max_{1 \le i \le N-1} c_i, \quad \text{wobei } c_N = M_1,$$

so lassen sich die Optimierungsbedingungen wie folgt formulieren:

1. für N soll das physikalisch Grösstmögliche gewählt werden,
2. M_1 soll zu einem Maximum werden,
3. M_2 soll zu einem Minimum werden, d.h. $Q := M_1 / M_2$ soll möglichst gross sein.

Für die Anwendung ist das folgende Resultat wichtig:

Satz:

$$(1) \quad M_1^2 = 2 \cdot \sum_{i=1}^{N-1} c_i + c_N$$

Offenbar sind also das maximale Signal M_1 und die Hintergrundsignale c_i nicht unabhängig voneinander!
Durch Umformung und Abschätzung der besten Verteilung erhält man das Wurzelkriterium, das zur Einschränkung des Suchintervalles benutzt werden kann.

$$(2) \quad M_1 \leq \frac{1 + \sqrt{1 + 4M_2(2N - M_2 - 1)}}{2}$$

Kernstück der Methode,welche bei einem vernüftigen Aufwand technisch interessante Kodierungen zu liefern vermag, sind Formel (2) und ein Zufallsgenerator mit gleichverteiltem Output. Dieser erzeugt mit hoher Effizienz 0-1 Sequenzen, d.h. binäre Zahlen erzeugt, deren M_1-Wert (=Anzahl Einer) im vorgegebenen Intervall $[M_1^{min}, M_1^{max}]$ liegt.
Es wird vorausgesetzt, dass ein Zufallsgenerator *random* zur Verfügung steht, dessen Resultate gleichverteilt im Intervall (0,1) liegen. Dieser soll dazu benützt werden, binäre Zahlen der Länge N zu erzeugen, welche im Mittel M_1 Einer enthalten. Diese Aufgabe wird durch das folgende "Programm" gelöst:

(3) $b_1 = b_n = 1$
shift = $(M_1 - 2)/(N - 2)$
for i = 2, 3, ..., N-1
x = random : $x \in (0,1)$
x = x + shift : $x \in$ (shift, 1+shift)
b_j = trunc : $b_j \in (0,1)$.

Eine exakte quantitative Beschreibung der so erzeugten Kodierungen ist mit der Theorie der Binominialverteilung möglich [1].
Mit dem letzten Beispiel soll das praktische Vorgehen für den Fall N=90 illustriert werden. Als erstes wird mit der Formel (2) eine Tabelle der maximalen Werte von M_1 als Funktion von M_2 berechnet. Dieser Wert ist ganzzahlig und soll mit $M_1^{max}(th)$ bezeichnet werden. Tabelle 1 stellt diesen Wert dem numerisch bestimmten maximalen Wert $M_1^{max}(num)$ gegenüber.

N	M_2	$M_1^{max}(th)$	$M_1^{max}(num)$	$[M_1^{min}, M_1^{max}]$
90	1	13	10	[10, 14]
90	2	19	14	[13, 19]
90	3	23	17	[13, 19]
90	4	26	19	[17, 23]
90	5	30	22	[20, 28]
90	6	32	24	[24, 30]

Tabelle 1.

Als nächstes muss für einen festen Wert M_2 der Erwartungswert M_1 und ein Suchintervall $[M_1^{min}, M_1^{max}]$ festgelegt werden, um das Verhältnis $Q = M_1/M_2$ zu optimieren. Tabelle 1 zeigt die Werte $M_1^{max}(num)$, welche durch Erzeugen und Auswerten von je 100'000 binären Zahlen gefunden wurden. Diese Resultate, die sich innert nützlicher Frist mit Hilfe eines Rechners finden lassen, sind technisch einsetzbar und deuten daraufhin, dass die gefundenen maximalen Verhältnisse M_1/M_2 nahe beim effektiven Maximum liegen.

[1] E. Kreyszig: Statistische Methoden und ihre Anwendungen, Vandenhoeck & Ruprecht.

A CALORIMETER BASED ON ULTRASONICS.

O.Oehler, P. Rusch und S. Dornbierer, Institute for Quantum Electronics, Swiss Federal Institute of Technology, CH-8093 Zurich, Switzerland.

Abstract: The temperature controlled tuning of an ultrasonic resonance in a gas allows calorimetric investigations. The thermal resolution of the method is 0.1 mK. Heat losses in optical wave guides of less than 5 μW are resolvable.

1. Introduction

Calorimetric investigations require accurate measurements of the temperature. In this connection usually solid state or liqud thermometers are used. The temperature dependence of the velocity of sound (dv/dT = 0.59 m/s K in air at 300 K) offers a direct temperature measurement of the gas surrounding the sample. dv/dT is detectable accurately by measuring the change in tuning of an ultrasonic resonator.

2. Apparative layout

Two identical ultrasonic transducers [1] were arranged oppositely in metal tube representing the calorimeter housing (Fig. 1). The transducers (the one used as an emitter, the other as a receiver) were operated at the wing of an acoustic resonance at a frequency of 220 kHz. The signal from the receiver was processed by a lock-in amplifier. Its low frequency output was fed to a digital storage oscilloscope used in its signal averaging mode [2].

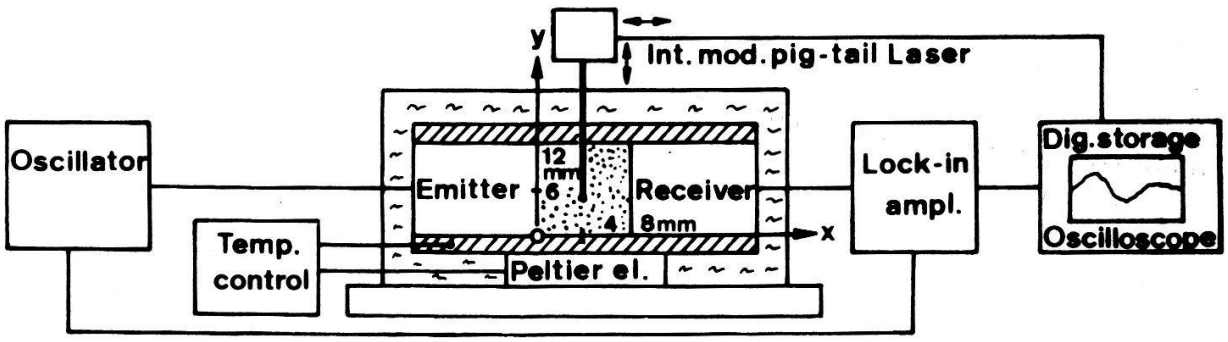

Fig. 1 Layout of the calorimeter

In order to protect the device against the influence of external heat sources the calorimeter housing was thermally shielded by an isolating jacket. Its temperature additionally was controlled by a NTC temperature sensor and a Peltier element.

3. Calorimetric investigations

The light absorbing end (black paint) of a mono-mode glass fiber was positioned in the ultrasonic resonator. By guiding the 815 nm radiation of a 200 uW pig-tail laser [3] the black spot and the surrounding air was periodical heated [4]. At the used frequency of 1.66 Hz the heat signal spreads by a few mm. The mounting of the fiber on a xy-table allows to probe the sensitivity distribtion within the acoustical resonator.

Fig. 2 shows the calorimetric sensitivity (expressed by a S/N-ratio of 1 at a signal averaging time of 10 s) on moving the probe along (2a) and perpenticular (2b) to the ultrasonic field. An extreme value of 5 μW was found in a cylindrical range of a diameter of ca. 3 mm at the center of the ultrasonic field.

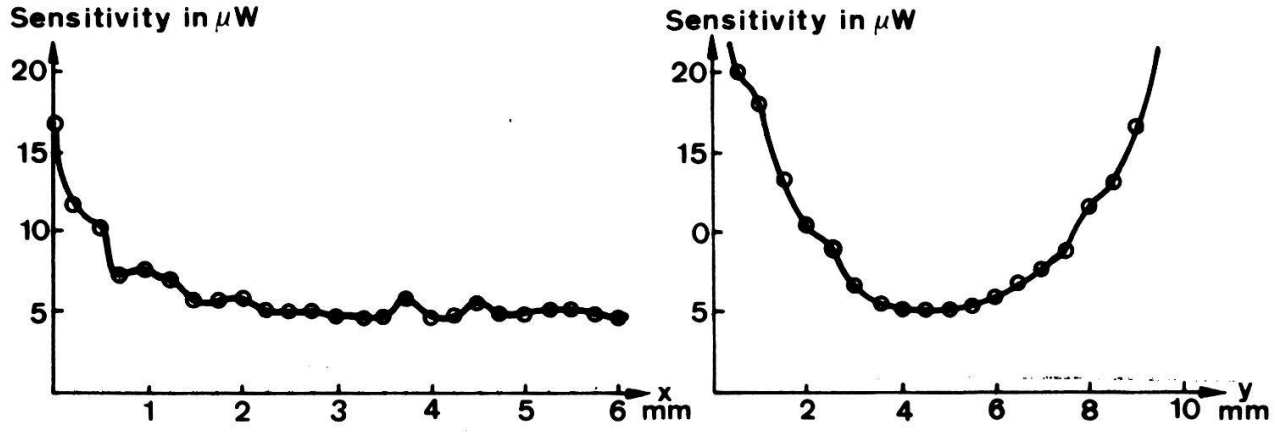

Fig. 2 Sensitivity of the calorimeter along (2a) and perpenticular (2b) to the ultrasonic field.

4. References

[1] Model E-188/220, Massa Products Corp., Hingham, Mass 02043, USA.

[2] O.Oehler, J.Wieland and S.Friedrich, Helv. Phys. Acta, **61**, 885 (1988).

[3] Model PT-450, Seastar Optics, Seattle, WA, 98104, USA.

[4] O.Oehler and A.Schäppi, Conference digest, 6th Int. Topical Meeting on Photothermal and Photoacoustic Phenomena, Baltimore, MD, 1989.

A MODEL FOR THE PATTERN FORMATION DUE TO EROSION

H.C.Schulz, T.Kautzky, E.Lüscher
Physik-Department E 13, Technische Universität München, D-8046 Garching

Abstract:We present a model calculation for erosion of soil due to surface water ending up with the same fractal structures as found in experiments and nature, as well.
To check the range of validity of our model we investigate the influence of the model parameters on pattern formation and conpare with our experimental results. An evaluation of Haussdorf dimension is carried out.

1. Introduction - the experiment to be modelled

The starting point for our model was an experiment carried out recently by C. Davidopoulos and R.Wittmann [1] ,[2]. The experimental setup consisted of a circular shaped flat box (diameter 140 cm) filled with a 9 cm layer of sand and covered by approximately 1 mm of water. The sand was watered homogeneously near the brim by a rotating sprinkler while sand and water could flow out throug a sink (diameter 39 mm) in the middle of the box. The result were dendritic river systems, bearing a strong resemblance to tideways.

2. The model

To obtain a better understanding of the processes leading to these structures we designed a computer model that works as follows: The experimental sandbox is replaced by two twodimensional arrays, representing the height of sand and water, respectively. In the beginning, all array elements have equal heights, both sand and water, representing the initial wet sand of the experiment, exept the center element, where both is zero. During every cycle the following algorithm is carried out for each array element:

Is there less sand at any neighbouring element? (the diagonals are regarded,too, thus each element has eight neighbours)

yes: Move all water of the current element to the lowest element in the neighbourhood (if "lowest" is ambigous, the decision is made by random).
Decide by random wheather a grain of sand is removed at the current position. The probability for the removal is proportional to the difference of sand height and the flow of water.

no: *Is there less water at any neighbouring element having the same sand height as the current element*?

yes: Move half of the surplus water to the "driest" neighbour.

no: No action.

After each cycle, all water at the element in the middle,representing the sink, is removed, and the water height at all rim elements is increased. Thus our model has the following parameters:

- *wetness*, the initial water height at all elements
- *inflow*, the amount of water added to the rim elements after each run
- *rain*, the amount of water added to all elements after each run
- *glue*, representing the force between single grains of sand. The probability for the erosion of a grain is inverse proportional to *glue*.

The algorithm is stopped, when the erosion reaches the brim. This model does not care about

- the maximum steepness of sand heaps. Erosion is only caused by the flow of water.
- the eroded sand grains. They just vanish. No deposition takes place.

3. Results and Comparison to the Experiment
Our model performed quite well compared to its crudeness, we could find the main features of the experiment:

- the develloping of dendritic structures
- increasing fractal dimension and growth rate of the dendrit with increasing inflow
- a cauliflower structure at the edge of the eroded regions, i.e. a softly curved utmost border and a dendritic structure develloping within. This typical feature of many dendritic structures in nature showed up both in experiment and simulation.

4. Outlook
As the computed erosion patterns show all typical features of the experiment (except the breakdown of too steep edges, which is typical for sand, but not an important feature of the erosion of most types of rock, and which could be included by a smoothing algorithm) it can be used for studying the influence of several parameters controling erosion processes. An adaption to various geometrical situations is easy and allows investigation of artificial interventions to contain erosion.

Literatur

[1] C.Davidopoulos, Diplomarbeit TU Muenchen (1989)

[2] R. Wittmann, to appear in: Naturwissenschaften

INTERMITTENCY IN THE KÁRMÁN VORTEX STREET

M. Rose, C.H. Schulz, T. Kautzky [1], E. Lüscher
Physik-Department E 13, Technische Universität München, D-8046 Garching

Abstract: Kármán-Vortex-Streets after a circular zylinder in the parameter range between periodic vortex shedding and turbulenz are investigatet. The experimental time series are examined for intermittency by next-maxima-plots and histograms.

1. Introduction:

The flow behind a circular cylinder, streamd along perpendicular to his axis, shows a different behaviour, according to flow velocity. Up to Reynolds-numbers Re≈10 one observes laminar flow. From Re≈50 to approx. Re=150 periodic vortex shedding occurs, the Karman vortex street. At Re>300 the flow is turbulent. We investigate the region of transition between periodic and turbulent flow, where chaos shold appear [1][2], i.e. where the complex system should be described by low-dimensional differential equations.

2. Intermittency in the Karman Vortex Street:

A typical transition from periodic to chaotic dynamics is the route of intermittency. In this case the dynamics of the system, if the order-parameter, here the Reynolds-number, exeeds a critical value, alternates irregulary between regular and chaotic states. The frequency of the chaotic states increases with the order-parameter.
Common descriptions of intermittent systems are next-maxima-plots, where the $n+1^{st}$ maximum is plotted over the n^{th} maximum, and a histogram of the maxima. In the figures the measured dynamics of the Kármán vortex street is compared with data from the Rayleigh-Bénard-problem, which is well examined for intermittency [3].
Fig.1 shows the time series, the R.B.-data being typical for type III intermittency. Fig.2 the amplitude-histogram with a significant accumulation at the amplitude of the periodic oscillator, which is typical for any type. Fig.3 is a next-maxima-plot. The indication for intermittancy in this plot is the fact, that it tuches the diagonal near the point of the periodic oscillator.
We could not jet assign the intermittency to one of the three types, because different representations suggest different types. Nevertheless the comparison of the two systems shows many similaryties, so that the assumption of intermittency in the transition region is well supported[4][5].

[1] part of Ph.D. thesis

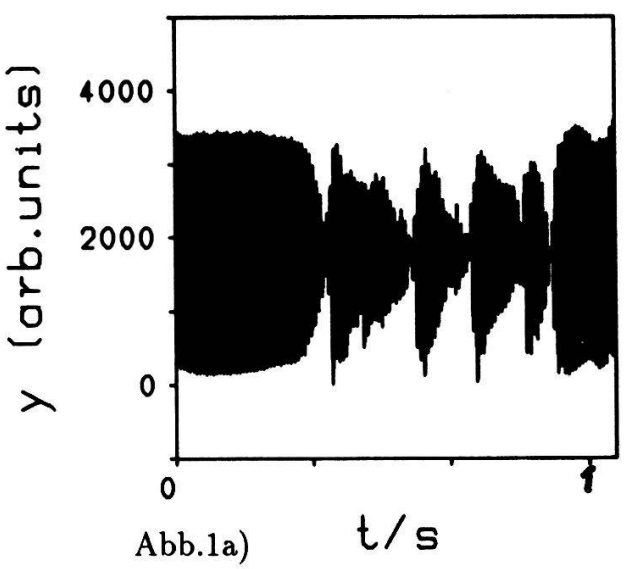

Abb.1a)

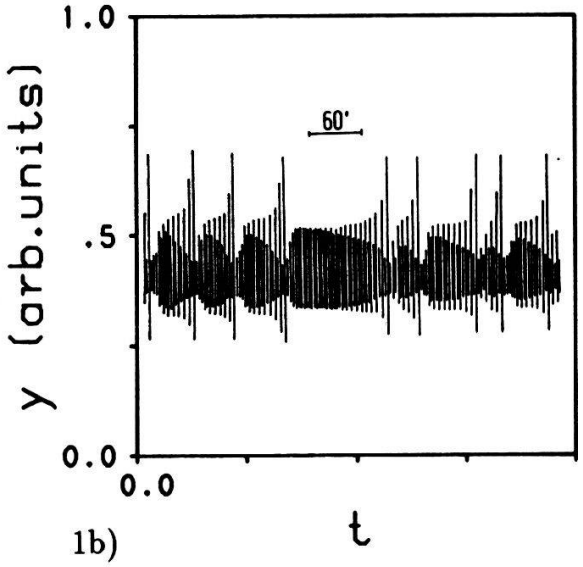

1b)

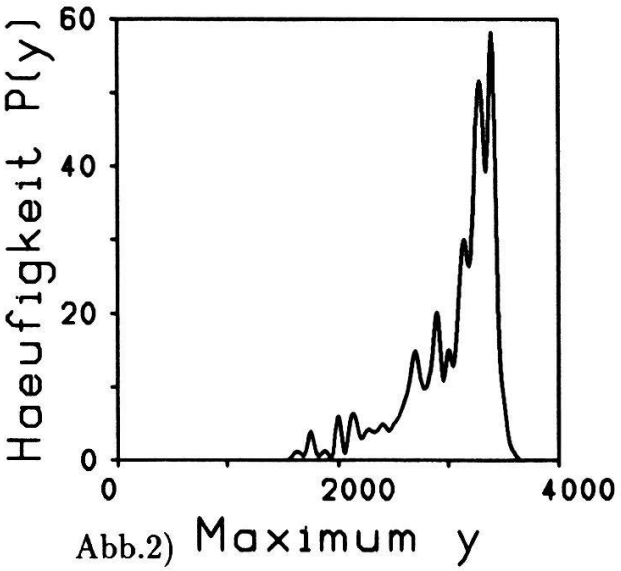

Abb.2)

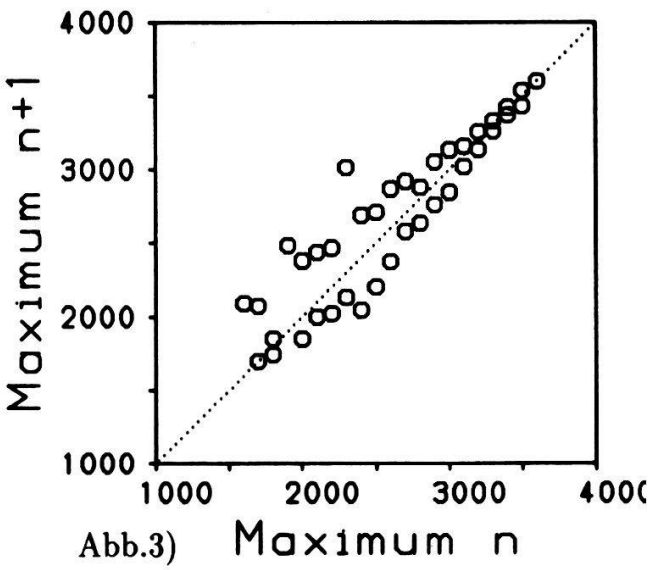

Abb.3)

Fig.1: Time-series of vortex-street (a) and of R.B.-convection (b)[6]
Fig.2: Amplitude-Histogram of intermittent vortex street
Fig.3: Next-maxima-plot of intermittent vortex street

References

[1] E. Lorenz, J. Atm. Sci 20, 130 (1963)
[2] D. Olinger, K. Sreenivasan, Phys. Rev. Let. 60, 797 (1988)
[3] P. Bergé, Y. Pomeau, C. Vidal: Order within chaos, John Wiley (1984)
[4] M. Rose, T.Kautzky, A.Hübler, E.Lüscher, Helv. Phys. Acta 62, 286 (1989)
[5] M. Rose, Diplomarbeit, 1989
[6] M. Dubois, M.A. Rubio, P. Bergé, Phys. Rev. Let. 51, 1446 (1983)

Extremal Properties of Dendritic Structures: Investigations on Systems of Blood-Vessels

M. Athelogou*, H. Kaltner•, J. Kitzbichler, G. Elender, E. Lüscher

Technische Universität München, Physik-Department E13, D-8046 Garching
• Institut für Physiologie, Physiologische Chemie und Ernährungsphysiologie der Tierärtzlichen Fakultät, Ludwig-Maximilian-Universität, Veterinär Str.13, D- 8000 München 22.

Abstract:

Biological systems often show dendritic patterns. Typical examples are plant roots, nervous systems, blood-vessels. These structures are optimal in the stationary state with regard to the surrounding conditions. A measure for the growth of this structures is the development of the fractal dimension and the change of the dissipation of the system. Measurements on blood- vessel-systems of embryos of the *JapaneseQuail* (Coturnix coturnix japonica), incubated in vitro [J. Wittmann et al. 1987], show the optimality of these structures and characterize the growth-stages of the system.

Introduction :

Open systems often exhibit dendritic patterns. In the stationary state dendritic patterns are characterized by a minimum of the "dissipation"/1/.We examine properties of blood-vessel-structures by determination of the fractal dimension D_f and a mathematical analysis of the system based on the diffusion equation and continuity equation.

Theory :

The buisiness of the blood-vessel-system is to supply the embryo with oxygen and nutrients from the yolk and to dispose of metabolic wastes. We consider the following two-dimensional model of the vessel-system (Fig.1a). The black dot in the center (embryo) is supposed to be an ideal absorber of ions, which are homogeneously distributed over the container (yolk). The system is assumed to be open, the ions having identical number of charges (Z e) and interact only electrically. The equation of continuity for this system is:

$$Ze\frac{\partial \varrho(\vec{x},t)}{\partial t} = -div\vec{j}_e(\vec{x},t) + ZeS_0 \tag{1}$$

The sourceterm S_0 represents the supply of nutrients, $\vec{j}_e(\vec{x},t)$ is the electrical currentdensity and $\varrho(\vec{x},t)$ is the density of ions in the region F, i. e. of the two dimensional space between the blood-vessels. Assume that the Ohms low is valid, the current-density is given by :

$$\vec{j}_e(\vec{x},t) = -\sigma_0\vec{\nabla}\Phi(\vec{x},t) - ZeD\vec{\nabla}\varrho(\vec{x},t) \tag{2}$$

$\Phi(\vec{x},t)$ is the eletrical potential, σ_0 the electrical conductivity of F and D is the diffusion-constant. The Poisson-equation is:

$$\triangle\,\Phi(\vec{x},t) = -\frac{4\pi Ze\varrho(\vec{x},t)}{\varepsilon} \tag{3}$$

where ε is the dielectrical-constant of F. In the stationary state $\frac{\partial \varrho(\vec{x},t)}{\partial t} = 0$ holds.

In the stationary state equation (3),equation (2) and equation (1) give:

$$\triangle\,\varrho = \frac{4\pi\sigma_0}{\varepsilon D}\varrho - \frac{S_0}{D} \tag{4}$$

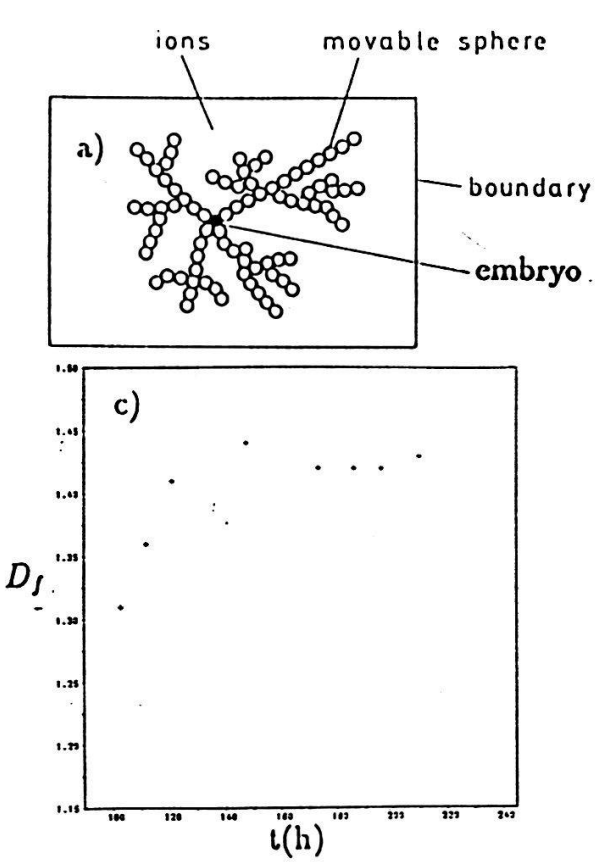

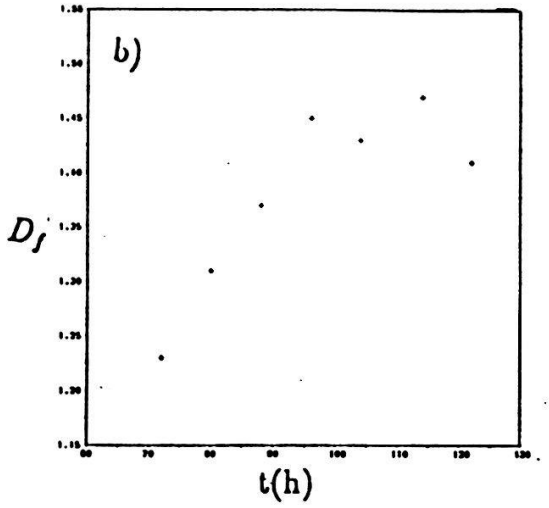

Fig.1 a) Model for a blood-vessel-system. Fractal dimension as a function of time t(h): b) : yolksak-circulation, c) : allantoic circulation.

We assume that the system is in a local-equilibrium-state and globally not far from equilibrium. Thus we can write for the dissipation P of the system:

$$P = \int_F T\sigma d\vec{f} = \int_F \frac{D\varrho}{kT}(\vec{\nabla}\mu_e)^2 d\vec{f} \qquad (5)$$

with $\mu_e = kTln\varrho(\vec{x},t) + Ze\Phi(\vec{x},t)$. We call μ_e electrochemical-potential. T is the constant temperature and σ the local entropy production in the system. Under the above assumptions and in the approximation of linear nonequilibrium-thermodynamics σ is a Lyapunov- function /4/. That means that the dissipation of the system in the stationary state must be minimal. The calculation of the dissipation of the system is possible by numerically solving the equation (5) for the dendritic structure of the blood-vessels.

Experiment and Experimental Results:

We have recorded the growth of embryos of the *JapanescQuail* (Coturnix coturnix japonica), incubated in vitro /3/, using a video camera. Locations of the blood-vessels belonging either to the **yolksak-circulation** or the **allantoic circulation** were obtained after a run with a picture-processing- system using these records. Application of a box-counting- algorithm to these data yielded the fractal dimension.

Discussion:

The blood-vessel-systems reache a stationary state. This stationary state is characterized by a constant value of the fractal dimension. According to the above theoretical model the dissipation of the system has to be minimal in the stationary state.

Literature:

/1/ B. Merté, P. Gaitzsch, M. Fritzenwanger, W. Kropf, A. Hübler, E. Lüscher, Helv. Phys. Acta 61, 76(1988).

/2/ M. Athelogou, B. Merté, P. Deisz, A. Hübler, E. Lüscher, Helv. Phys. Acta 63 (1989).

/3/ J. Wittmann,W. Kugler, H. Kaltner, J. Exp. Zool.[Suppl.]1, 325-329(1987).

Biochemistry 10, 338-345(1988).

/4/I. Prigogine, vom Sein zum Werden, R. Piper, Co. Verlag, München 1987.

*part of Ph.D. thesis

MEASUREMENT OF THE J/ψ INCLUSIVE CROSS SECTIONS IN PBAR-P AND P-P COLLISIONS AT $\sqrt{s}$ = 24.3 GEV FROM UA6 EXPERIMENT

A. Bernasconi [2], R.E. Breedon [4], L. Camilleri [1], R.L. Cool [4]†, P.T. Cox [4], L. Dick [1], E.C. Dukes [3], F. Gaille [2], P. Giacomelli [4], C. Joseph [2], W. Kubischta [1], J.F. Loude [2], E. Malamud [2], C. Morel [2], O.E. Overseth [3], J.L. Pagès [2], J.P. Perroud [2], P. Cushman [4], D. Rüegger [2], R Rusack [4], G.R. Snow [3], G. Sozzi [2], M.T. Trân [2], A. Vacchi [4] and G. Valenti [3].

[1] CERN, CH-1211 Geneva 23, Switzerland
[2] Institut de Physique Nucléaire, Université de Lausanne, CH-1015 Lausanne, Switzerland
[3] Physics Department, University of Michigan, Ann Arbor, MI 48109, USA
[4] The Rockefeller University, New York, NY 10021, USA

Abstract: Inclusive cross sections times branching ratio for $J/\psi \rightarrow e^+e^-$ are measured with the same apparatus at $\sqrt{s}$ = 24.3 GeV for both $p\bar{p}$ and pp collisions. The comparison of the two production rates provides an estimation of the contributions of $q\bar{q}$ and gg fusions to the formation of $c\bar{c}$ state.

1. Apparatus

The experiment [Fig. 1] is located in a straight section of the CERN SPS tunnel. A hydrogen cluster jet target is sent through

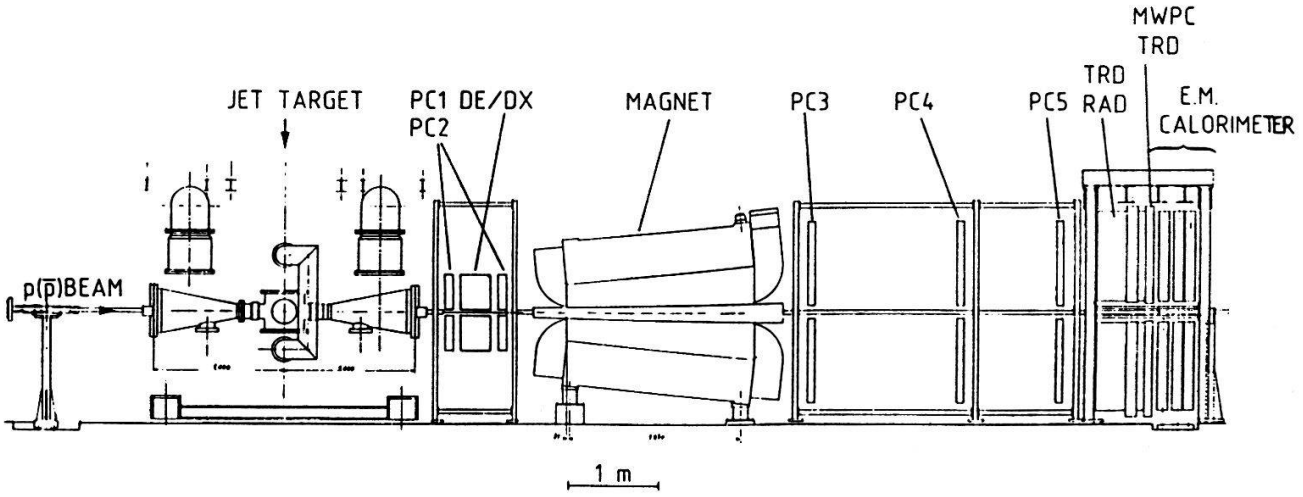

Fig. 1 Layout of the UA6 experiment in the SPS tunnel

the collider beams. The luminosity is monitored with four silicon detectors [1] by counting near $\theta = 90°$ in the lab frame the recoil protons from elastic scattering. The apparatus consists of a double arm magnetic spectrometer with a vertical field and a bending power of 2.3 Tm. Five multiwire proportional chambers (PC) allow to track the charged particles. A transition radiation detector (TRD) [2] improves the electron-hadron discrimination. Electromagnetic showers are measured with a lead-proportional tube sampling calorimeter [3]. A hodoscope of seven horizontal scintillation counters located between the first and the second module of the calorimeter provides signals for the trigger logic.

2. Cross section measurements and comparisons

The number of J/ψ is obtained by subtracting the like sign from the unlike sign effective mass spectra within the mass window $2.8 < M_{eff} < 3.3$ GeV/c^2; this gives (91 ± 10) events for $p\bar{p}$ and (153 ± 14) for pp data corresponding to integrated luminosities of 540.7 nb^{-1} and 1496.9 nb^{-1}, respectively. Cross sections times e^+e^- branching ratio for J/ψ inclusive production integrated over p_t and $0 < y < 1.0$ are (6.4 ± 0.9 ± 0.4) nb for $p\bar{p}$ collisions and (4.9 ± 0.6 ± 0.3) nb for pp interactions. The ratio $\sigma(pp)/\sigma(p\bar{p})$, evaluated from a simple QCD model of open charm production [4] which accounts for $q\bar{q}$ and gg fusion mechanisms and uses Duke-Owens (set 1) parametrization [5] of the distribution functions, is found to be 0.75. Our results give 0.76 ± 0.14 ± 0.11. This value hence agrees with a naive theoretical estimation and shows the importance of the gluon contribution to the formation of $c\bar{c}$ state.

3. References

[1] R. Breedon et al., Phys. Lett. 216B 459 (1989)
[2] A. Vacchi, Nucl. Instr. Methods A252 498 (1986)
[3] S. Baumann et al., CERN-EP/89-89
[4] M. Glück, J.F. Owens and E. Reya, Phys. Rev. D17 2324 (1978)
[5] D.W. Duke and J.F. Owens, Phys. Rev. D30 49 (1984)

MUON TRANSFER TO LOW Z ELEMENTS

R. Jacot-Guillarmod, F. Mulhauser, C. Piller, L.A. Schaller, L. Schellenberg and H. Schneuwly,
Institut de Physique de l'Université, CH-1700 Fribourg, Switzerland

Abstract : New measurements of muon transfer from protium to nitrogen and neon show, together with other measured muon transfer rates, that these rates do not have a monotonous Z dependence. In neon, a second component of unknown origin is observed.

According to our present knowledge, a negative muon, stopped in a mixture of natural hydrogen with a small amount of another gas of atomic number Z, forms either a muonic hydrogen atom or a muonic Z atom in an excited state. In the deexcitation process, muonic X-rays are emitted. Because the formation and the cascade are very fast (of the order of 10^{-12} s for Z>2), these X-rays appear promptly with regard to the incoming muon. After deexcitation of the $(\mu p)^*$ system (in about 10^{-10} s at 10 bar), which occurs essentially by collisions [1], the $(\mu p)_{1s}$ atom disappears either by muon decay with an associated rate λ_0, by formation of a $p\mu p$ mesomolecule (λ_{pp}), or by transferring the muon to deuterium (λ_d) or to the Z element (λ_{pZ}). The total disappearance rate, λ, of the μp atom is then : $\lambda = \lambda_0 + \lambda_{pp} + \lambda_d + \lambda_{pZ}$

This rate λ or equivalently the lifetime $\tau=1/\lambda$ of the μp atom in the ground state can be measured through the exponential time distribution of the muonic X-rays of the element Z, which appear delayed with respect to a muon stop signal [2]. The rates λ_0, λ_{pp} and λ_d being known, the transfer rate λ_{pZ} can be deduced. The transfer from μd atoms can be taken into account and the transfer rate from protium to element Z determined accurately [2]. For comparisons, it is normalized to the atomic density of liquid hydrogen ρ_0 : $\Lambda_{pZ} = (\rho_0/\rho_Z)\,\lambda_{pZ}$.

The muonic X-ray intensity patterns resulting from muon transfer from thermalized $(\mu p)_{1s}$ atoms [2] are essentially different from those proceeding from direct muon capture [3]. The relative intensities of the transfer X-rays can be predicted [4] and the measured ones agree well with these calculations [2],[5].

The intensity structure of the delayed muonic X-rays in nitrogen, measured in a gaseous mixture of hydrogen with 4337 ppm N_2 at 15 bar, agrees with theoretical predictions [4]. The delayed time spectra of all four observed transitions of the Lyman series are pure exponentials with the same lifetime τ of the $(\mu p)_{1s}$ atom, the average value being $\tau=1/\lambda=334$ (3) ns. The deduced normalized transfer rate to nitrogen, $\Lambda_{pN}=0.34\ (7)\cdot 10^{11}\ s^{-1}$, is surprisingly about three times smaller than the transfer rate from deuterium.

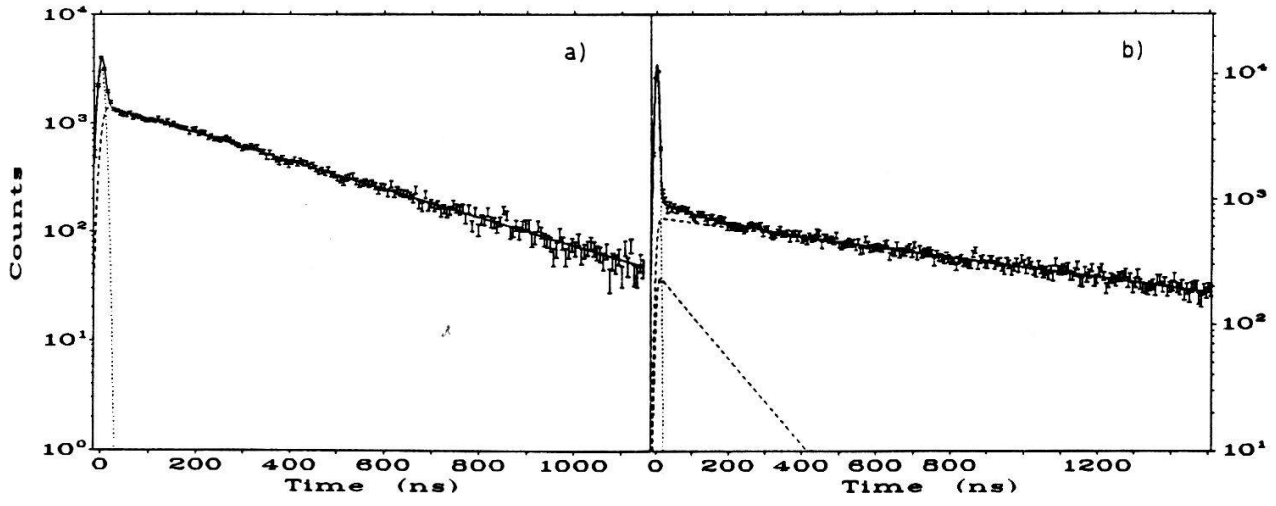

Fig. 1. Measured and fitted time spectra of the muonic K_α transitions of a) nitrogen, and b) neon.

Time and intensity spectra of muonic X-rays have been measured in a mixture of hydrogen with a concentration of 6930 ppm Ne at 15 bar. As for nitrogen, the experimental and theoretical intensities are in good agreement. For the time spectra of the muonic Ne(2-1), Ne(3-1) and Ne(4-1) to Ne(6-1) transitions, one needs two exponentials to obtain a good fit. The comparison of the time spectra of the muonic K_α transition in neon and nitrogen (Figs. 1a and 1b) shows that the shape of the neon spectrum just after the prompt peak is different. If one assumes that the flatter slope corresponds to the mean lifetime of the $(\mu p)_{1s}$ atom, the steeper one is then due to an unknown process, perhaps comparable to the one observed in H_2+SO_2 [5]. However, the normalized transfer rate deduced from the steeper slope corresponds exactly to the value obtained by Alberigi Quaranta et al. [6], namely $\Lambda_{pNe}=1.15\ (20)\cdot 10^{11}\ s^{-1}$, whereas the flatter one yields a 20 times lower rate.

By comparing the measured muon transfer rates (Fig. 2), e.g. to low Z elements like nitrogen, oxygen and neon, one observes that these transfer rates do not have a monotonous Z dependence, as predicted by theoretical calculations for high Z elements.

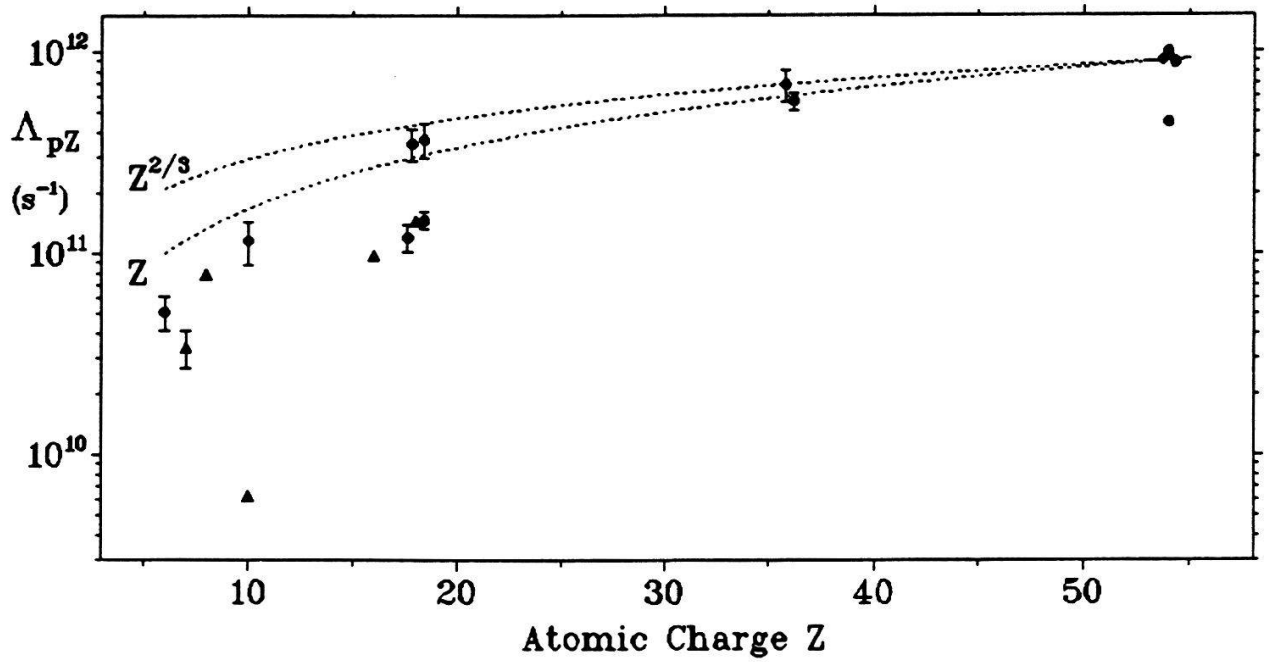

Fig. 2. Experimental transfer rates measured at room temperature. Points represent data from ref. 2 and 6-10, triangles correspond to measurements made by our group.

References

[1] V.E. Markushin, Zh. Eksp. Teor. Fiz. 80, 135 (1981); Sov. Phys.-JETP 53, 16 (1981).
[2] R. Jacot-Guillarmod, F. Bienz, M. Boschung, C. Piller, L.A. Schaller, L.Schellenberg, H. Schneuwly, W. Reichart and G. Torelli, Phys. Rev. A 38, 6151 (1988).
[3] R. Jacot-Guillarmod, F. Bienz, M. Boschung, C. Piller, L.A. Schaller, L.Schellenberg, H. Schneuwly and D. Siradovic, Phys. Rev. A 37, 3795 (1988).
[4] G. Holzwarth and H.-J. Pfeiffer, Z. Phys. A 272, 311 (1975), V.R. Akylas and P. Vogel, Comp. Phys. Commun. 15, 291 (1978).
[5] H. Schneuwly, R. Jacot-Guillarmod, F. Mulhauser, P. Oberson, C. Piller and L. Schellenberg, Phys. Lett. A 132, 335 (1988)
[6] A. Alberigi Quaranta, A. Bertin, G. Matone, F. Palmonari, A. Placci, P. Dalpiaz, G. Torelli and E. Zavattini, Nuovo Cimento B 47, 92 (1967).
[7] A. Bertin, M. Bruno, A. Vitale, A. Placci and E. Zavattini, Phys. Rev. A 7, 462 (1973); Lett. Nuovo Cimento 4, 449 (1981).
[8] S. G. Basiladze, P. F. Ermolov and K. O. Oganesyan, J. Exptl. Theoret. Phys. 49, 1042 (1965); Sov. Phys.-JETP 22, 725 (1966).
[9] A. Placci, E. Zavattini, A. Bertin and A. Vitale, Nuovo Cimento A 64, 1053 (1969).
[10] E. Iacopini, G. Carboni, G. Torelli and V. Trobbiani, Nuovo Cimento A 67, 201 (1982).

MUON TRANSFER IN H_2 + SO_2 GAS MIXTURES

F. Mulhauser, R. Jacot-Guillarmod, C. Piller, L.A. Schaller, L. Schellenberg and H. Schneuwly,
Institut de Physique de l'Université, CH-1700 Fribourg, Switzerland

Abstract : The analysis of the time spectra of the muonic oxygen x-rays, measured in four H_2 + SO_2 gas mixtures, show all an unexpected component, the origin of which has not yet been explained.

The muon transfer process in binary and ternary gas mixtures looks like a well known process [1]. From the ground state of the μp atom, where the muon has a binding energy of about 2.6 keV, which is large compared to chemical binding energies, the muon is transferred to higher Z elements onto atomic orbits with much smaller radii than the outer electron shells of the atom Z, and where the muon has a comparable binding energy. The transfer process does therefore not depend on chemical structures and bonds in which the element, to which the muon is transferred, is involved.

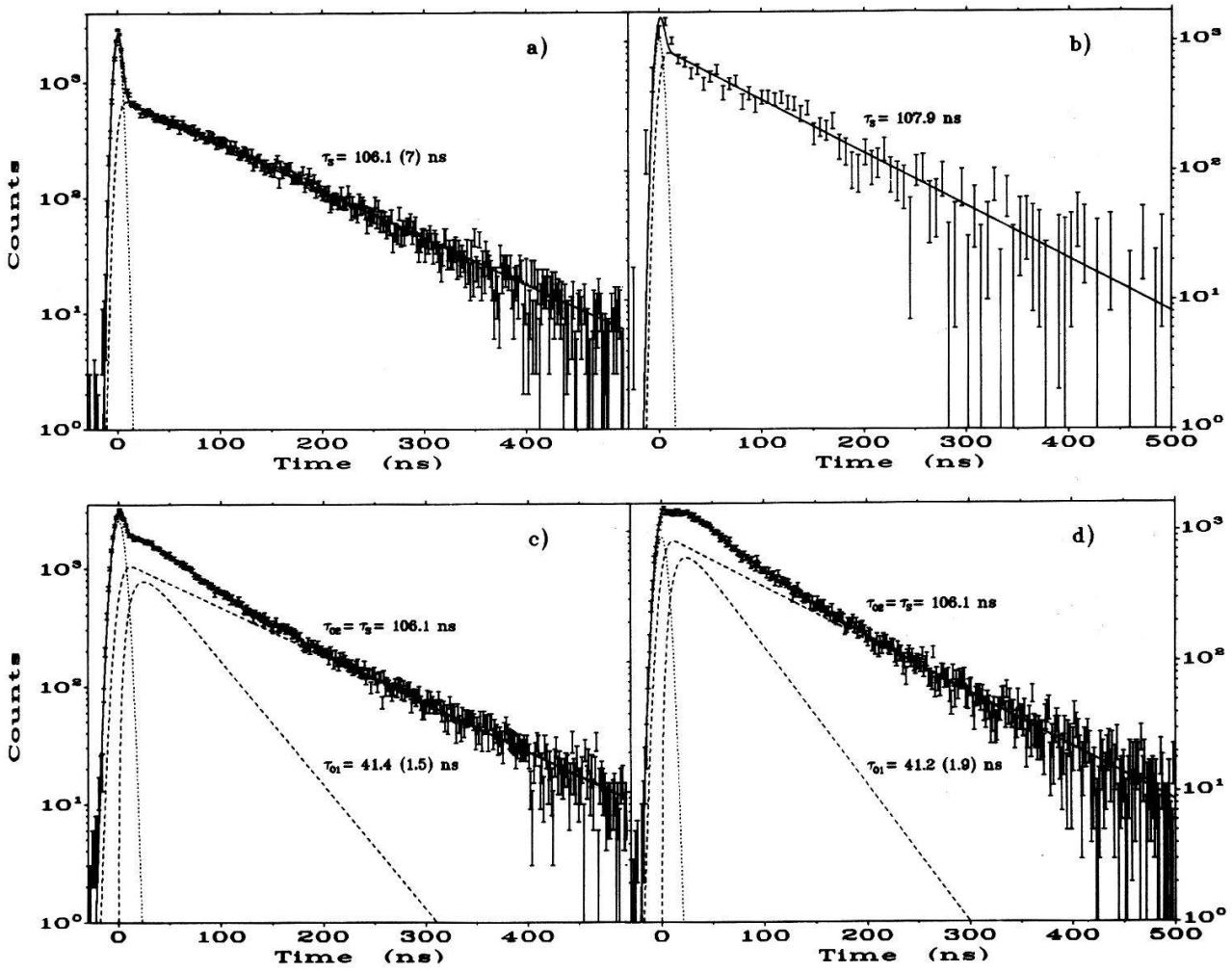

Fig. 1. Measured and fitted time spectra of the muonic a) 2p-1s and b) 5-2 transitions of sulphur, c) 2p-1s and d) 3p-1s transitions of oxygen.

According to our present knowledge, the μp atom in the ground state disappears in a H_2 + SO_2 gas mixture by muon decay with a rate λ_0, by formation of a pμp molecule (λ_{pp}) or by transferring the muon to deuterium (λ_d), to oxygen (λ_O) or to sulphur (λ_S). The total disappearance rate λ of the μp atom can then be written

$$\lambda = \lambda_0 + \lambda_{pp} + \lambda_d + \lambda_S + 2\lambda_O$$

$1/\lambda = \tau$ is then the lifetime of the μp atom in the ground state under the corresponding experimental conditions of pressure, temperature and relative concentration.

The μp lifetime can be determined by measuring the time distribution of the muonic x-rays resulting from muons transferred either to oxygen or to sulphur.

In a previous experiment [2], we observed that the time spectra of the sulphur x-rays had, as expected, one decay constant, corresponding to the lifetime of the μp atom in the ground state. The time spectra of the oxygen x-rays, however, had two time constants, suggesting the existence of two kinds of μp atoms in the ground state [3].

The experiment has been repeated at PSI under slightly different conditions of total pressure (H_2 + 0.4% SO_2 at 15 bar). The single time constant in the sulphur x-rays and the double time constants in the oxygen x-rays appeared again (Figs. 1). Because of the higher statistics of the second experiment, a third time constant, corresponding to a rise time of the order of 10ns, has been observed in all oxygen time spectra (Figs. 1c and 1d). Such a rise time is absent in the sulphur time spectra (Figs. 1a and 1b).

Under other experimental conditions of pressure and relative concentration (H_2 + 0.2% SO_2 at 10 and 15 bar) these differences between the time spectra of oxygen and sulphur x-rays have been confirmed.

The muon transfer rates to sulphur dioxide, normalized, as usual, to the atomic density of liquid hydrogen, found by analyzing the time distributions of the muonic sulphur x-rays in all four gas mixtures, agree well with each other and with theoretical estimates for the lifetime of the μp atom in the ground state under the given experimental conditions[4,5].

At present, no explanation for the second oxygen time component has been found, yet. Such a second component, but with a much larger rise time, has also been observed in fluorine of a H_2 + SF_6 gas mixture.

References

[1] R. Jacot-Guillarmod, F. Bienz, M. Boschung, C. Piller, L.A. Schaller, L.Schellenberg, H. Schneuwly, W. Reichart and G. Torelli, Phys. Rev. A 38, 6151 (1988).

[2] H. Schneuwly, R. Jacot-Guillarmod, F. Mulhauser, P. Oberson, C. Piller and L. Schellenberg, Phys. Lett. A 132, 335 (1988)

[3] H. Schneuwly, Muon Catalyzed Fusion 4, 87 (1989)

[4] S.S. Gershtein, Sov. Phys.-JETP 16, 501 (1963)

[5] G. Fiorentini and G. Torelli, Nuovo Cimento A 36, 317 (1976)

INTERFERENCE PHENOMENA IN REACTIONS OF MUON TRANSFER FROM PROTIUM TO HEAVIER NUCLEI

Yu.S. Sayasov

Institute of physics, University of Fribourg, CH-1700 Fribourg

As it is well known, see e.g. [1] §90, cross-sections of inelastic collisions between two atoms accompanied by an electronic transition are characterised by oscillatory behaviour with respect to collision energy E and other parameters. These oscillations due to interference of wave-functions of the atom relative motion in the initial and final states are described under quasiclassical conditions by the factor $\cos^2 S$ where S is a phase shift. For the atomic collisions S is usually very big and the factor $\cos^2 S$ is replaced, after an appropriate averaging, by the numerical factor 0,5. Similar assumption is used, too, for calculation of the cross-section σ_{tr} of the muon transfer to a nucleus Z in the reaction $1\mu + Z = 1 + Z\mu$, see e.g. [2]. However, for such processes the assumption $S \gg 1$ is, in fact, often not justified. Effective distances corresponding to mesic processes e.g. the distance r_c corresponding to crossing of the term U_i (for the system 1μ, Z) and U_f (for the system 1, $Z\mu$) are very small, typically of the order of $r_c \approx 10\, a_\mu \approx 10^{-10}$ cm (a_μ is the mesic radius) and they can be comparable to the de Broglie wave length $\lambda\!\!\!^{-}_i = 1/\sqrt{2M(E-U_i)}$ pertaining to relative motion of 1μ and Z. Here 1μ is system consisting of proton or deutron or triton and muon and M is the mass of 1μ.). For this reason the quasiclassical or WKB approximation equivalent to the assumption $S \gg 1$, may be not applicable in this case. In the present note we give an estimate for σ_{tr} using device described in [1], §90, i.e. representing the terms U_i, U_f in the vicinity of the crossing-point $r = r_c$ by the linear approximations $U_i = U_o - F_i(r-r_c)$, $U_f = U_o - F_f(r-r_c)$, $F_{i,f} = -(\partial U_{i,f}/\partial r)_{r=r_c}$, $|F_i| \ll |F_f|$. In this way the wave-functions χ_i, χ_f corresponding

resp. to initial (term U_i) and final (term U_f) states can be expressed through the Airy functions. This approximations remains valid also in cases when the WKB approximation for the function χ_i fails.

Within two-state distorted wave-approximation σ_{tr} can be represented by the formula (we are using mesic units)

$$\sigma_{tr} = 6\pi \left(\frac{2}{M}\right)^{1/2} \frac{Z}{v} w\, F(\xi),\quad F(\xi) = \xi^{1/2}\left[\cos\phi\Phi(\xi) - \sin\phi\Psi(\xi)\right]^2$$

$$\phi = \frac{\pi}{4} - \frac{10}{3}\xi^{3/2},\quad \Phi = \pi^{-1/2}\int_0^\infty \cos\left(\xi t + \frac{1}{3}t^3\right)dt,$$

$$\Psi = \pi^{-1/2}\int_0^\infty \sin\left(\xi t + \frac{1}{3}t^3\right)dt \qquad (1)$$

where w is the Landau-Zener transition probability, v is the thermal velocitiy of 1μ, and $\Phi(\xi)$, $\Psi(\xi)$ are the Airy functions. Transition to WKB-approximations corresponds to $\xi = \left[1/2\left(\frac{\partial\chi_i}{\partial r}\right)_{r=r_c}\right]^{2/3} = (3\sqrt{2M}\, Z/8r_c)^{2/3} \gg 1$ and the function $F(\xi)$ reduces thereby to $\sin^2 S$, $S = 4\xi^{3/2}$. Corresponding expression for the transition rate $\lambda = \sigma_{tr} v n_{H_2} = 5{,}2\cdot10^{10} Z M_p^{-1/2} F(\xi)w$ normalized to liquid Hydrogen density ($n_{H_2} = 4{,}2\cdot10^{22}$ cm^{-3}) shows that (1) represents satisfactorily non-monotonous behaviour of λ as a function of Z revealed in [3]. (Here M_p is the mass of 1μ referred to the mass of pμ). In particular, (1) explains anomalously low value of $\lambda_{pNe} = 0{,}056\cdot10^{11}$ sec^{-1} found in [3]. In this case $\xi = 0.78$, $F(0{,}78) = 0{,}015$ and we have from (1), under an assumption $w = 0{,}5$, $\lambda_{pNe} = 0{,}04\cdot10^{11}$ sec^{-1} in reasonable agreement with experiment. For similar process dμ + Ne = d + Neμ we have $\xi = 0{,}98$, $F(0{,}98) = 0.71$ and $\lambda_{dNe} = 1{,}8\cdot10^{11}$ sec^{-1} (for $w = 0{,}5$), again in reasonable agreement with experiment [3]: $\lambda_{dNe} = 1{,}4\cdot10^{11}$ sec^{-1}.

REFERENCES

[1] L. Landau, E. Lifshits, Quantum Mechanics, Pergamon, 1958.

[2] S. Gershtein, Soviet Physics-JETP, 16, 501 (1963).

[3] R. Jacot-Guillarmod et al., Muon Transfer to Low Z Elements, in EM Cascade and Chemistry of Exotic Atoms, Eds. L.M. Simons, D. Horvath, O. Torelli, to be published by Plenum Press.

DETERMINATION OF THE ABSOLUTE MAXIMUM OF POLYNOMIALS BY ALGEBRAIC BISECTION

V.Thurner, W.Eberl, A.Hübler, N.Packard, E.Lüscher*
CCSR, Beckman Institute, Urbana, IL 61801
*Physik-Department E13, TU München, D-8046 Garching

Abstract

Many theoretical approaches to physical phaenomena lead to optimization problems, typically to the problem of finding the absoulte maximum of a polynomial [e.g. modeling of complex systems, spin glasses]. Well-known methods like gradient dynamics or simulated annealing have the disadvantage of not being definitely reliable in finding the absolute extremum. We present a new method where we devide the polynomial's interval into several parts, prove that some of these parts cannot contain the absolute maximum and eliminate those parts from further calculations.

1. Algorithm

We consider a polynomial in n variables:

$$P(x_1, x_2, \ldots, x_n) := \sum_{i_1=0}^{m_1} \sum_{i_2=0}^{m_2} \cdots \sum_{i_n=0}^{m_n} a_{i_1,i_2,\ldots,i_n} {x_1}^{i_1} \cdot {x_2}^{i_2} \cdot \ldots \cdot {x_n}^{i_n} \tag{1}$$

or shorter:

$$P(\vec{x}) := \sum_{\vec{i}=\vec{0}}^{\vec{m}} a_{\vec{i}} \prod_{j=1}^{n} {x_j}^{i_j} \tag{2}$$

1. For one variable x_i, devide the corresponding interval into b parts and estimate the polynomial's lower bounds $L(P(\vec{x}))$ and upper bounds $U(P(\vec{x}))$ in each part. A good choice would be $b = 4$.
2. If the upper bound of a part is smaller than the lower bound of any other part, this part cannot contain the maximum. Consequently, it does not have to be considered any more.
3. Estimate lower and upper bounds of the derivatives $\frac{\partial P(\vec{x})}{\partial x_i}$ for each remaining part.
4. If for any part $U(\frac{\partial P(\vec{x})}{\partial x_i}) < 0$, it cannot contain a maximum, unless it is the leftmost part of the corresponding original interval.
5. If for any part $L(\frac{\partial P(x)}{\partial x}) > 0$, it cannot contain a maximum, unless it is the rightmost part of the corresponding original interval.
6. For each part that has not been excluded using (2., 4., 5.), start again with (1.) and a different x_i, until the desired precision is reached for each variable.

Usually, all parts can be excluded exept the one that contains the maximum. If there exist several maxima of equal value in different parts, all these parts will remain. Maxima at the boundaries will be detected as well.

2. Estimation of a Polynomial's Upper and Lower Bounds in a Certain Interval

Any polynomial $P^0(\vec{x}) := \sum_{\vec{i}=\vec{0}}^{\vec{m}} a_{\vec{i}} \prod_{j=1}^{n} x_j{}^{i_j}$ can be transformed in such a way that, without restricting universality, we can assume $P(\vec{x} = \vec{0}) = 0$ and the interval to be the unit interval $\left[\vec{0}, \vec{1}\right]$. To calculate the upper and lower bound for any part of the polynomial, we transform this part so that it meets these conditions. Having calculated both bounds, we retransform them and thus receive the bounds for the corresponding part of the original polynomial.

To estimate the polynomial's upper and lower bounds, devide the sum into a rising, strictly positive, and a falling, strictly negative part:

$$P(\vec{x}) := \underbrace{\sum_{\vec{i}=\vec{0},a_{\vec{i}}>0}^{\vec{m}} a_{\vec{i}} \prod_{j=1}^{n} x_j{}^{i_j}}_{u(P(\vec{x}))} + \underbrace{\sum_{\vec{i}=\vec{0},a_{\vec{i}}<0}^{\vec{m}} a_{\vec{i}} \prod_{j=1}^{n} x_j{}^{i_j}}_{\ell(P(\vec{x}))} \tag{3}$$

Since $u(P(\vec{x}))$ has its maximum and $\ell(P(\vec{x}))$ its minimum at $\vec{x} = \vec{1}$, $\ell(P(\vec{1})) \leq P(\vec{x}) \leq u(P(\vec{1}))$ for all $\vec{x}$ in the unit interval. Thus we receive as estimates of the polynomial's bounds $U(P(\vec{x})) = u(P(\vec{1}))$ and $L(P(\vec{x})) = \ell(P(\vec{1}))$.

For obtaining a better estimate of $U(P(\vec{x}))$, consider that $x_j{}^{i_j} < x_j{}^{i_j-1}$ for any x_j in the unit interval, thus $a_{\vec{i}} \prod_{j=1}^{n} x_j{}^{i_j} \leq a_{\vec{i}} \prod_{j=1}^{n} x_j{}^{k_j} \leq a_{\vec{i}}$ and

$$U(a_{\vec{i}} \prod_{j=1}^{n} x_j{}^{i_j} + a_{\vec{k}} \prod_{j=1}^{n} x_j{}^{k_j}) \leq U((a_{\vec{i}} + a_{\vec{k}}) \prod_{j=1}^{n} x_j{}^{k_j}) = a_{\vec{i}} + a_{\vec{k}} \tag{4}$$

if $k_j \leq i_j$ for all $j = 1, \ldots, n$.

After substituting those $a_j \prod_{j=1}^{n} x_j{}^{i_j}$ with $i = 1, \ldots, m$ and positive a_j by $a_j \prod_{j=1}^{n} x_j{}^{k_j}$ with $k_j \leq i_j$ for all $j = 1, \ldots, n$, we receive a new polynomial $P^*(\vec{x}) > P(\vec{x})$ for any x_j in the unit interval. If we choose for substitution those k_j with negative coefficients a_k, the polynomial $P^*(\vec{x})$ can be simplified by adding up $a_{\vec{i}} \prod_{j=1}^{n} x_j{}^{k_j}$ and $a_{\vec{k}} \prod_{j=1}^{k_j}$ as shown in (4). Using (3) on this simplified polynomial $P^*(\vec{x})$, we obtain a rather good estimation of $U(P(\vec{x}))$. To calculate $L(P(\vec{x}))$, the same algorithm may be used, considering that $L(P(\vec{x})) = -U(-P(\vec{x}))$.

As an example, let us look at the onedimensional polynomial $P(x) = -x + 3x^2 + 2x^3 - 6x^5 + 4x^7$. After carrying out all substitutions, we receive $P^*(x) = -x + 3x + 2x - 6x^5 + 4x^5 = 4x - 2x^5$ as simpler polynomial. Using (3) on $P^*(x)$, we obtain $U(P(x)) = 4$ as estimate for the upper bound of the polynomial $P(x)$.

We acknowledge A.Hayd, P.Meinke, H.B.Fischer and O.Wohofsky for continuous support.

References:

This work is part of the PhD thesis of W.Eberl.

V.Thurner, W.Eberl, A.Huebler, N.Packard (1989): *Technical Report CCSR-89-20, Algebraic Bisection Method for Detection of the Absolute Maximum of Polynomials*, CCSR, Beckman-Institute, Urbana-Champaign, IL 61801, U.S.A.

Applications:

W.Eberl, A.Huebler, N.Packard, E.Luescher (1990): *Unique Models for Stochastic Dynamics*, H.P.A. 63.

The Influence of Asynchronous Control on the Geometry of Cellular Automaton Patterns

Ch. Scholz, W. Eberl*, K. Birken, S. Zaunseder, E. Lüscher
Physik-Department E13, TU München, D-8046 Garching

Abstract
Cellular automata are often defined on a quadratic or hexagonal lattice. Normally, the geometry of the solutions depends strongly on the underlying geometry of the automata. A large variety of automata-solvable problems (e.g. reaction-diffusion-systems), however, should show a more or less round and wiggly boundary. Besides the possibility of introducing a random lattice, one can use asynchronous control of the automata. A method to simulate asynchronous control will be presented.

1. Synchronous and Asynchronous Cellular Automata

It is well known that for several physical problems cellular automata represent good models [1]. Normally, cellular automata are controlled synchronously, but some asynchronous cellular automata have been investigated as well [2]. Here we have examined two types of cellular automata, a PDE-solver and an epidemic model as an example for a reaction-diffusion system.
If the cells are updated synchronously, there exists a superior unit which provides an updating for the whole system at discrete moments. In case of asynchronous control, each automaton's time-development is unique, rather than controlled by a superior unit. For a hardware construction of an automata system, the system with asynchronous control in some cases leads to a simpler solution than designing a superior unit. To simulate a cellular automata system, run through a *computing cycle* and an *updating cycle* according to one of the queues in figure (1). Asynchronicity is gained by using a mixed queue with a certain insertion region. Here, a processed cell is not attached to the end of the queue, but is **inserted into** the queue within a certain region. A measure for the asynchronicity is then defined by $\alpha := \frac{\text{length of inserting-region}}{\text{total number of cells}}$.

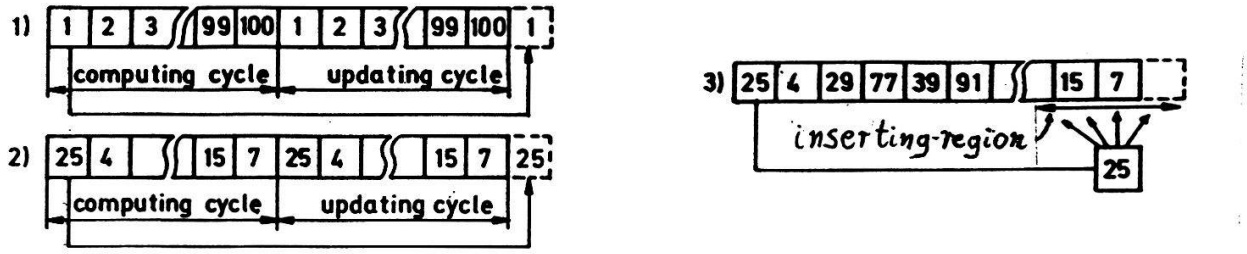

Figure 1: Three different queues for managing the updating. 1. This queue simulates the usual synchronous cycle. 2. Using a mixed queue, the results do not change when computing and updating is strictly separated. 3. Definig an insertion area the queue is continuously mixed. A larger insertion area will lead to greater deviations from the synchronous results.

2. Asynchronous Version of the Gauss-Seidel-Algorithm as an Example of a PDE-Solver

The above method of simulating asynchronous control can be applied to PDE-solvers like the Gauss-Seidel method that can also be interpreted as an cellular automaton with a von Neumann neighborhood. We tried to solve the Laplace equation $\Delta\phi = 4$ with random initial values [4]. A comparison of the rates of convergence of the Jacobi, the synchronous and the asynchronous Gauss-Seidel method shows that the asynchronous Gauss-Seidel method always achieves better or equal results than the well-established Jacobi method, even if $\alpha = 1$.

3. A Model of an Epidemic

In our a model of an epidemic, a sick cell infects its four next neighbours in the first time step. In the next time step, the state of the sick cell changes to 'resistant', and stays like that for the next nine time steps. After that, the cell is infectable again. Mathematically, this model can be described by

$$z_{ij,t+1} = \begin{cases} z_{ij,t+1} - 1 & \text{if } z_{ij,t} \geq 1 \\ 10 & \text{if } z_{ij,t} = 0 \quad \wedge \quad (z_{i\pm1j,t} = 10 \quad \vee z_{ij\pm1,t} = 10) \end{cases}$$

with $z_{ij} = 0, 1, ..., 10$. Part one of figure 2 shows the starting condition. A small stripe of cells is infected, the cells in the immediately neighbouring vertical rows are resistant.
Part two of figure 2 shows the synchronous solution. The unrealistic regularity of the pattern is obvious. In part three of figure 2, you see a rounder, more realistic pattern, which was calculated with asynchronous control. Due to asynchronicity, the time structure is weakened. Thus follows a weakening geometry of solutions.

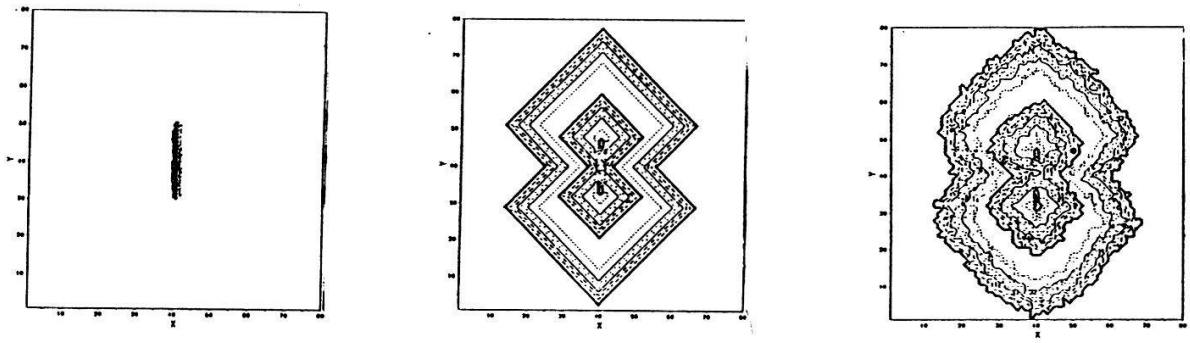

Figure 2: Time development of an epidemic with synchronous or asynchronous control. Left: Initial condition, middle: result after 100 cycles with synchronous control, right: asynchronous control ($\alpha = 10\%$)

4. Summary and Outlook

We have found a method for simulating asynchronous control, where the time order can be disturbed more or less ($\sim \alpha$), but the cells in average are updated the same number of times. Asynchronous control can be used to get more realistic results for cellular automata models, although the correlation between asynchronicity and 'roundness' is not yet understood theoretically. It should be possible to use α as an additional model parameter for other physical effects like crystal growth with defects.

We want to acknowledge O.Wohofsky, H.-B. Fischer, A.Hayd, P.Meinke and N.Packard for fruitful discussion and continuous support.

References

[1] S. Wolfram, Theory and Applications of Cellular Automata,1986
[2] T.E. Ingerson, R.L. Buvel, Physica 10D, 59 (1984)
[3] T.Toffoli, N. Margolus, Cellular automata machine, MIT Press, 1987
[4] Ch. Scholz, Diplomarbeit am Institut E13, TU München

* This work is part of the PhD thesis of W. Eberl.

ANGULAR MOMENTUM, SPIN AND ENERGY-MOMENTUM LOCALIZATION IN SCHERRER'S FORMALISM OF GENERAL RELATIVITY

J. Chevalier, rue des Vignes, CH-2822 Courroux, Switzerland

Abstract: In Scherrer's formalism of general relativity, the angular momentum conservation can be derived directly from the field equations, provided that spin is taken into account. Applied to the Lense/Thirring solution, this result then shows that the total angular momentum depends on the tetrads. This circumstance suggests that the tetrads have to be determined uniquely, which localizes gravitational energy-momentum.

1. Angular momentum conservation. Spin

Recently, we have discussed the possibility of localizing gravitational energy-momentum (GEM) in two tetradic formalisms of general relativity (Møller and Scherrer) [1]. The argumentation was founded on the tetrad dependence of the angular momentum (AM) (see Def. (1.4) of [1]). It is unfortunately very difficult, and perhaps impossible, to obtain the conservation law for this AM. But we can overcome this difficulty as follows (in the present paper, we use Scherrer's formalism [2]; for the notations, see Ref. [1] and [2]). First consider the field equations (FE):

$$\frac{\partial t^{\lambda,\mu\alpha}}{\partial x^{\alpha}} = -\kappa T^{\lambda,\mu} \quad \left(t^{\lambda,\mu\alpha} \equiv \frac{\partial \mathfrak{H}}{\partial(\partial g_{\lambda,\mu}/\partial x^{\alpha})} = -t^{\lambda,\alpha\mu}\right) \tag{1.1}$$

and then the integral:

$$J^{\lambda\mu} \equiv \int [(x^{\lambda} T^{\mu,0} - x^{\mu} T^{\lambda,0}) + \frac{1}{\kappa}(t^{\lambda,0\mu} - t^{\mu,0\lambda})]\, d^3x \quad \text{''} \tag{1.2}$$

With the help of the FE and Gauss' theorem, we get easily:

$$J^{\lambda\mu} = -\frac{1}{\kappa} \lim_{S \to \infty} \int_S (x^{\lambda} t^{\mu,0k} - x^{\mu} t^{\lambda,0k})\, dS_k \tag{1.3}$$

and moreover, if we write $\mathfrak{J}^{\lambda\mu/\alpha}$ for the integrand of (1.2), with 0 replaced by α, it appears that $\partial \mathfrak{J}^{\lambda\mu/\alpha}/\partial x^{\alpha} \equiv 0$. Consequently, the $J^{\lambda\mu}$ are conserved and can be computed as limits of surface integrals (1.3). The total AM $J^{\lambda\mu}$ is thus the sum of an orbital momentum $B^{\lambda\mu}$ and of a spin momentum $S^{\lambda\mu}$:

$$B^{\lambda\mu} \equiv \int (x^{\lambda} T^{\mu,0} - x^{\mu} T^{\lambda,0})\, d^3x \qquad S^{\lambda\mu} \equiv \frac{1}{\kappa} \int (t^{\lambda,0\mu} - t^{\mu,0\lambda})\, d^3x \tag{1.4}$$

'' On account of Møller's conditions at infinity [3], it is not necessary to specify the nature of the indices λ and μ of the global quantities $J^{\lambda\mu}$, $B^{\lambda\mu}$, $S^{\lambda\mu}$.

2. Application to the Lense/Thirring solution

In order to calculate the total AM, we need the $g^{\lambda,\mu}(x)$ very far from the field sources, i. e. in the post-Newtonian approximation (PNA). Let's compute for instance the component J^{12} for an homogeneous uniformly rotating sphere (around the z-axis). From the definition (1.1), we find for the $t^{\lambda,\mu\nu}$(Scherrer):

$$t^{\lambda,\mu\nu} = \sqrt{-g}\, g_{\alpha,}{}^{\nu} g_{\beta,}{}^{\mu} [f^{\lambda\alpha\beta} - f^{\alpha\beta\lambda} - f^{\beta\lambda\alpha}] \qquad (2.1)$$
$$- 2\sqrt{-g}\, f^{\alpha} [g^{\lambda,\mu} g_{\alpha,}{}^{\nu} - g^{\lambda,\nu} g_{\alpha,}{}^{\mu}]$$

The calculations are tedious, but straightforward. For the $t^{1,0k}$ and $t^{2,0k}$ in the PNA, the result is:

$$t^{1,01} \cong -\frac{1}{2}\zeta_{1,1} + v_{,2} + w_{,3} \qquad t^{1,02} \cong -\frac{1}{2}\zeta_{1,2} - v_{,1} \qquad (2.2)$$
$$t^{1,03} \cong -\frac{1}{2}\zeta_{1,3} - w_{,1} \qquad (+ \text{cycl. perm. for the } t^{2,0k})$$

where we wrote: $\zeta_i \equiv -g_{0i} \qquad g^{0i}{}_{,i} \equiv -\frac{1}{2}\zeta_{,i} + v$ etc. (2.3)

According to the expressions (2.2), we can expect that J^{12} actually depends on the choice of the functions u, v, w(x). Consider for instance the case u = v = w = 0 (Møller solution). We get easily:

$$J^{12}(v = v = w = 0) = \frac{4MR^2\omega}{15} \qquad (2.4)$$

(M ≡ mass of the sphere, R ≡ radius, ω ≡ angular velocity), i. e. the 2/3 of the correct value. But putting $u = 1/2\ \zeta_1$, $v = 1/2\ \zeta_2$, $w = 1/2\ \zeta_3$ (spin density = 0 in the PNA), we find the "good" AM: $(2/5)MR^2\omega$, which thus proves that the total AM indeed depends on the tetrads. Consequently, it is reasonable to search for a theory which could allow to determine them uniquely (see [1]). Nevertheless, note that the justification given in [1] might be disputed for the reasons mentioned in the beginning of the present paper, which is not the case here.

In a later article, we shall study more in detail the rôle of the spin and shall show how considerations about this concept lead to the same theory as in [1].

3. References

[1] J. Chevalier, Helv. Phys. Acta 62, 335 (1989).
[2] W. Scherrer, Z. f. Physik 138, 16 (1954) and later papers.
[3] C. Møller, Mat. Fys. Skr. Dan. Vid. Selsk. 1, no. 10 (1961).

UNIQUE MODELS FOR STOCHASTIC DYNAMICS

W. Eberl, A. Hübler, N.Packard, E. Lüscher*
CCSR, Beckman Institute, Urbana, IL 61801, USA
* Physik-Department E13, TU München, D-8046 Garching

Abstract:

Starting from a noisy set of experimental data, we reconstruct maps in order to describe and control the dynamics of the corresponding system. When including long-time correlations and coloured noise the problem of modeling leads to the problem of finding the absolute maximum of a likelihood-function.

1. Introduction:

The dynamics of a large variety of nonlinear oscillators and a lot of other complex systems can be well described by special maps like Poincaré maps. These maps can be used for an effective prediction and control of the system [1]. When Gaussian noise is assumed, this maps can be calculated using a Least-Square-Fit or correlated methods [2]. However, colored noise cannot be modeled with this method. Furthermore it is necessary to include long-time correlations in order to get a better model [3], especially when the data are not homogeneously distributed in a certain range of state space. In this paper we calculate a likelihood-function [4]. The maximum of this function can be calculated by means of computer algebra [5] and leads to the coefficents of the model.

2. Reconstruction of maps from experimental time series

We start from a given set of N experimental data $\vec{x}_i^e$, $i = 1, 2, \ldots, N$, where $\vec{x}_i^e$ are n-dimensional vectors. We assume that the complex dynamics can be modeled by a low dimensional deterministic model with additional noise

$$\vec{y}_{i+1}(y_i) = \vec{F}(\vec{y}_i, \vec{p}) + \vec{F}_N(\vec{q})$$

where $\vec{p}$ and $\vec{q}$ are the parameters of the model, $\vec{F}_N$ is colored noise. For simplicity, in the following only the one-dimensional case will be considered, but a generalization for higher dimensional systems is straightforward.

In order to estimate the parameters $\vec{p}$ and $\vec{q}$ we use a maximum likelihood method. The transition propability functions are:

$$T_1(y_i, y_{i+1}; \vec{p}, \vec{q}) = D\left(y_{i+1} - F(y_i, \vec{p}), \vec{q}\right)$$

$$T_2(y_i, y_{i+2}; \vec{p}, \vec{q}) = \int T_1(y_i, y_{i+1}; \vec{p}, \vec{q}) \cdot T_1(y_{i+1}, y_{i+2}; \vec{p}, \vec{q}) dy_{i+1}$$

where T_j is the probability of transition from y_i to y_{i+j}, $\vec{p}$ are the parameters of the deterministic part of the model and $D(x,\vec{q})$ is a propability density function with $\vec{q}$ as the parameters of the color of the noise. The integrals of T should be calculated analytically, thus we propose to use polynomials as density functions. $T_3, T_4, \ldots$ are defined analogously, so that the propability of a piece of the trajectory starting at y_n leading over l points is given by $P(y_n, y_{n+1}, \ldots, y_{n+l}) = T_1 \cdot T_2 \cdots T_l$.

We use the Maximum-Likelihood-Estimation for the comparison of the probabilities of the eperimental trajectories and the trajectories predicted by the model. Thus, the optimal parameters of the model can be found by calculating the absolute maximum of

$$L = \prod_{i=1}^{N-1} \prod_{j=1}^{l} T_j(y^e_{i+j}, y^e_i; \vec{p}, \vec{q})$$

3. Example We considered a special dynamics generated by a logistic map and an approximately Gaussian noise:

$$T(y_i, y_{i+1}; a, d_f) = E_{app}\left((y_{i+1} - a y_i(1-y_i))^2 / {d_f}^2\right)$$

with $E_{app}(x) := 0.987539 - 8.87895x^2 + 32.7768x^4 - 59.5967x^6 + 52.3996x^8 - 17.576x^{10}$

For various values of d_f the parameter a could be reconstructed from a short time series (10 or 50 data) with a precision of approx. 10%. Using 500 data it was also possible to get an estimate for d_f.

We like to thank H.-B.Fischer, A.Hayd, P.Meinke and O.Wohofsky for fruitful discussions and continuous support. This work was supported in part by MAN.

This paper is part of the PhD thesis of W. Eberl.

[1] A. Hübler, R. Georgii, W. Eberl, E. Lüscher, Helv. Phys. Acta **62**, 290 (1989)
[2] A. Hübler, Helv. Phys. Acta **62**, 343 (1989)
[3] A.M.Albano, A.Passamante, M.E.Farrell, submitted to Phys. Rev. A
[4] I.N.Bronstein, K.A.Semendjajew, Taschenbuch der Mathematik (Deutsch, Thun 1981), chapt. 5
[5] V.Thurner, W.Eberl, A.Hübler, N.Packard, E.Lüscher, H.P.A. **63** (1990)